PLANET FORMATION AT HIGH RESOLUTION: FROM GROUND-BASED EX-AO TO JWST

by

Alexandra Zvia Greenbaum

A dissertation submitted to The Johns Hopkins University in conformity with the requirements for the degree of Doctor of Philosophy.

Baltimore, Maryland

August, 2016

Abstract

The field of exoplanets has grown rapidly over the last 10 years, especially with technological advances in radial velocity and transit photometry methods of discovery. While direct imaging is behind in discovery tallies it is still competitive in characterization of discovered exoplanets. Direct imaging from the ground is sensitive to a younger population of planets that are still glowing from the heat of formation. Probing planet formation with high angular resolution methods complements coronagraphic surveys from both the ground and space. Combining direct imaging designs with state of the art wavefront control and downstream instrumentation for, e.g., spectroscopy and polarimetry is essential for understanding planet formation and evolution processes. Ground-based instrumentation sets the stage for flying mature high contrast technologies on future space telescopes to obtain the most scientific yield.

I present my contributions to the current direct imaging revolution, both for ground based instrumentation as well as preparing for the upcoming JWST mission. I will begin by describing an image-based algorithm for reducing interferometric

ABSTRACT

data, and outline the factors that limit contrast for binary detection. I will present the results from commissioning and characterizing the Gemini Planet Imager's non-redundant mask, outlining the search space for high resolution observations with GPI. I will also discuss how new post-processing methods can remove biases from planet signals close-in that are buried under speckle noise. Lastly, I will show how interferometric methods contribute to wavefront sensing, which can serve as a backup mirror phasing method for JWST and which will be an essential component of future large space telescopes aimed at imaging exo-earths.

Primary Reader: Anand Sivaramakrishnan

Secondary Reader: Tobias Marriage

Acknowledgments

I feel incredibly privileged and fortunate for the path I took during my PhD and the support I've had throughout. My parents, Steve and Osnat Greenbaum have been endlessly supportive of me, well before I started graduate school and throughout. They truly made me believe that I could do anything. My partner David Arenivar has been an incredible friend and supporter throughout my PhD, amidst his own soul searching. I also want to thank the whole Arenivar family for their warmth and support.

Anand Sivramakrishnan has gone above and beyond the role of thesis advisor. In addition to coaching me through many difficult problems, he has afforded me countless opportunities to be in the right place at the right time. I truly admire his knack for mentoring and willingness to take on students of all backgrounds, and I aspire to be a mentor of his caliber (and to have his level of expertise using Vim).

Several people have also been mentors to me throughout my graduate work. Laurent Pueyo in many ways has been a secondary advisor to my thesis, getting me started on my first major project and working with me through various difficult ques-

tions. He has incredible technical expertise as well as a great vision for science. Marshall Perrin, who has a seemingly endless supply of knowledge and experience, is incredibly supportive of students and has always been very accessible. Remi Soummer has overseen the progress and experience of the many students and postdocs working within the lab and is also a great source of professional advice. Bruce Macintosh has been an excellent mentor and role model in his leadership of the GPI collaboration and thoughtfulness towards providing opportunities for students and postdocs. I also want to thank Peter Tuthill for hosting me in his research group at University of Sydney and advising on everything from image deconvolution to observing strategies. It's been a pleasure to work with so many experts in my field.

I also want to thank a number of my peers that I've had the pleasure to work with. Anthony Cheetham has given me a great deal of advice and helped me develop my analysis tools over the past few years, and especially in the last weeks leading up to my dissertation! Ben Pope is excellent to work with and always brings great ideas to the discussion. I also want to thank my graduate peers in the JHU Physics Astronomy program who really made the experience enjoyable and fun. Specifically, in my research group I want to thank Schuyler Wolff, my good friend and part of my cohort at JHU; there's a lot we've been through together in an outside of research, and I am excited to see all the great science she will continue to accomplish. I also want to thank Jonathan Aguilar, who made it easy to ask my most basic and embarrassing questions and who shared many of my curiosities, especially in this last

year. The Physics Astronomy graduate students together make a truly welcoming and fun atmosphere that is also conscious of inclusiveness and public outreach. I couldn't have asked for a better community in my 5 years at Johns Hopkins.

Dedication

To the people who have had a major impact in my life, but are no longer with us. My grandparents, Dora and Herman Greenbaum, Sarah and David Laske, survivors and immigrants who made a new life for their children, my parents. If not for their perseverance I would not be here today.

To John Arenivar, who was always so warm and supportive. We continue forward in your memory, and strive to honor it.

Contents

List of Tables

List of Figures

Chapter 1

Introduction

1.1 Planet formation – state of the art

The discovery of vast numbers of extra-solar planets (exoplanets) by the prevailing transit and radial velocity surveys, which both favor older, less active host stars, have revealed just some of the rich variety in the population of exoplanets. The slowly growing view of exoplanet demographics brings up new questions of how planets form from the proto-stellar disk, and how planetary architectures come to look the way we observe them in these (mostly) older systems. Direct imaging, while challenging provides the opportunity to image planets and circumstellar disks separate from their host stars. With current technology combining coronagraphs with extreme adaptive optics (ExAO – an adaptive optics system using of the order of a thousand or more actuators in the deformable mirror) direct imaging probes complementary science

compared with indirect methods of detection. Directly imaged low-mass detections (including both confirmed planets and low mass brown dwarfs), shown in the red circles in Figure 1.1 demonstrate the bias toward wider orbits and brighter companions. The less obvious bias is the sensitivity to younger ages, where planets are intrinsically bright. At very young ages (a few to 10s of Myr) planetary companions are still glowing from the heat of formation. Direct imaging surveys target these self-emitting object in infrared light, where their blackbody emission typically peaks. The challenges of ground based infrared observations have motivated space-based missions, notably *Spitzer*, *Herschel*, and the upcoming *James Webb Space Telescope* (*JWST*). *JWST*'s large aperture will provide not only high precision photometry at infrared wavelengths, but also higher resolution than previous infrared space missions.

While the number of directly imaged planets is small, various ground and space-based facilities have imaged a large number of circumstellar disks in both thermal and scattered light. The detection of disks around a variety of host stars provides another view of the environment of extra-solar system evolution. Space-based infrared and optical light instruments have imaged a gallery of disks, while ground-based instruments equipped with polarimeters have captured the scattered light in polarization. For ground-based mm and sub-mm observations the Atacama Large Millimeter/submillimeter Array (ALMA) achieves resolutions competitive and sometimes exceeding optical and infrared planet imagers, providing a complementary view of young disks sensitive to gas and mm-size dust emission.[1] Recent observations with

ALMA show ordered structure in a nearby protoplanetary disk TW Hya, a possible sign of planet formation around $\sim$ 1AU.[2] Together these various imaging methods provide a multiwavelength view of the planet formation environment, probing scattered light and thermal emission from dust grains of different sizes and measuring the presence and location of gas at various stages of evolution.

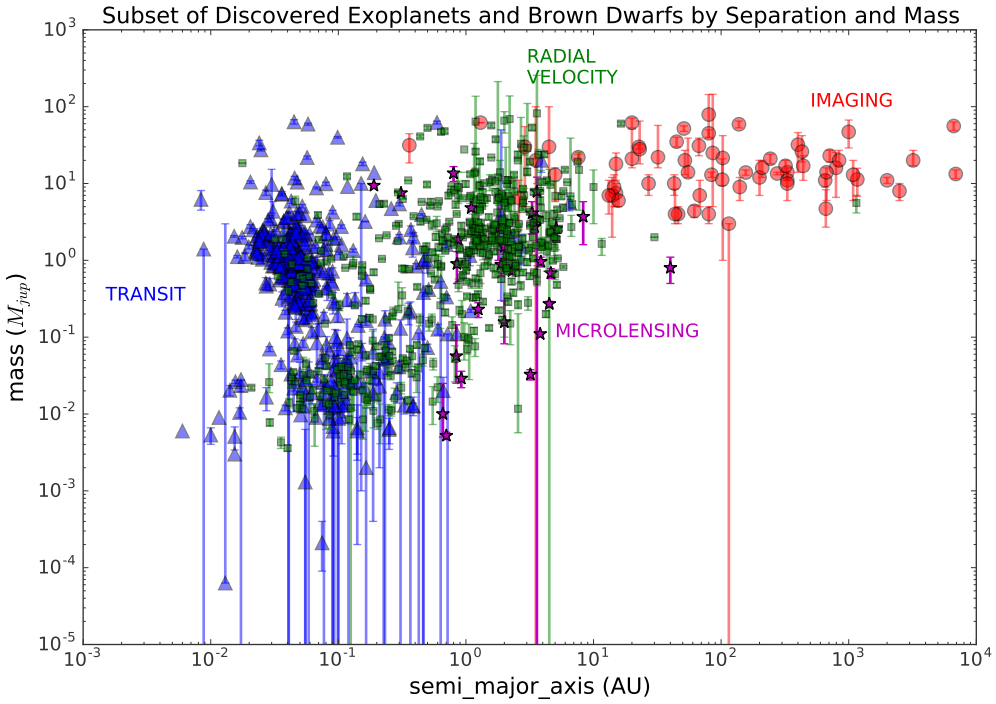

Figure 1.1: A selection of exoplanets and brown dwarfs discovered through Transit (blue triangles), RV (green squares), Direct Imaging (red circles), and Microlensing (magenta stars) techniques. The data are from the exoplanets.eu archive. Many of the direct imaging targets shown here have masses exceeding $13M_{jup}$, so are more likely brown dwarfs.

1.1.1 Relevant scales of planet formation

Current state of the art imagers using Ex-AO are digging down to 0.15 arcsec inner working angles with their coronagraphs and down to the diffraction limit through non-occulted imaging. Direct imaging surveys target youngs stars, often identified by their moving groups. Meanwhile the lessons learned on current ground and space-based instruments will help prepare for next generation space telescopes (e.g., High Definition Space Telescope[3] concepts) that will attempt to reach exo-earths with superb quality imaging from space with large apertures.

In order to overcome the stellar light to image planets down to a contrast of $\sim 10^{-6}$, state of the art imagers employ coronagraphs coupled with an extreme-AO subsystem. These latest imagers (e.g. GPI,[4] SPHERE,[5] etc.) push towards 0.1 arcsec inner working angle around the host star, using the host star itself to correct the wavefront. For a star 100pc away (as e.g., Sco-Cen star-forming region members) 0.1 arcsec is 10 AU from the star. In our own solar system 10 AU is beyond the orbits of Jupiter and Saturn, our gas giant planets.

Extrapolations from radial velocity surveys led to the prediction of a significant fraction of gas giant planets inside 20 AU.[6] The dearth of such objects in the latest exoplanet surveys so far brings to question assumptions made in yield predictions for direct imaging surveys. Evolutionary models that predict luminosity of low-mass objects are put to the test in this region and require some knowledge of the age of the system as well. High resolution methods probing 1-10 AU around the host star

expand the search space of direct imaging instruments and can either provide upper limits on the presence of low-mass companions, or reveal structure unavailable to ground- and space-based coronagraphs.

Non-redundant masking achieves interferometric resolution of $\lambda/2D$, complementing coronagraphic instruments. For example the Gemini Planet Imager's NRM is sensitive to $\sim$ 30 mas scales in H-band ($\sim 1.5 - 1.8\mu$m), or 3AU for stars 100pc away. Many coronagraphic survey instruments have one or more aperture mask.[7–10] Many of the newer facilities combine NRM with spectroscopy and/or polarimetry, increasing detection sensitivity.

1.1.2 Current questions of planet formation

Direct imaging provides planet photometry and, if followed up over multiple epochs, can provide an estimate of the orbit on sky. Multi-wavelength observing can help estimate effective temperatures and measure atmospheric compositions of giant planets. The luminosities of these giant planets can provide insight on mechanism of formation, depending on their age and mass. Direct imaging combined with radial velocity or astrometry measurements can also provide a direct measurement of mass.

For example, giant planets that form very rapidly due to gravitational instability in the disk are expected to be very bright at young ages (hot start). Giant planets that form through core accretion – first accumulating small bodies until they are large

enough to accrete gas rapidly – are expected to be cooler and smaller at young ages.[11] Inferring the formation mechanism from luminosity does depend on well-constrained age and mass.

Both models of formation face major challenges and distinguishing between the two mechanisms can only be resolved by many more observations. Directly imaged exoplanets to date are mostly too bright to be consistent with the cold start model. Another major challenge to this model is that the time scale needed to assemble enough material to undergo rapid accretion is longer than the dissipation timescale of gas in the disk.[12–14] Bodies formed through gravitational instability (that would lead to hot start conditions) are expected to be generally more massive than planets and at large separations.[15] A lack of substellar objects at $\gtrsim 20AU$[16] separations calls gravitational instability into question. Observing a large number of young giant planets at a range of early ages can help distinguish their formation mechanism. Direct imaging at multiple infrared bands can help narrow down the formation mechanism of a given planet or sub-stellar object.

Planets form in the circumstellar disk environment making disks with large gaps popular targets for planet searches. The timescales and conditions of planet formation are directly linked to the disks they inhabit. There a number of possibilities for how clearings form in protoplanetary disks, including interactions with planetary mass or larger companions. Whether planet/low-mass binary formation and dynamical evolution can explain the transitional disk period remains an outstanding question.

Spectroscopic observations can help estimate effective temperatures and accretion properties of disk gap companions, while polarimetry can probe the disk structures close in. Stable space instruments can push contrast limits at close inner working angles to either discover new companions or rule out their presence above a certain mass, as well as better characterize known cool companions' infrared colors. To date, many of the few low mass companions found inside disk gaps do not appear massive enough to open up the very large disk gaps and holes they inhabit. One explanation for massive disk gaps is that multiple unseen planets dynamically shape the circumstellar environment.[17] Deeper contrast imaging of the inner regions of disks will either uncover these additional companions or place limits on their presence.

Coronagraphic instruments push extreme contrasts and can characterize planet-mass companions spectroscopically from the ground but struggle to reach small inner working angles. At close separations direct imaging can overlap radial velocity sensitivity, especially for more massive companions. Complementary studies of young, low mass binaries can help break age-mass degeneracies and test luminosity predictions. Aperture masking on ground-based 8-10m class telescopes push the smallest inner working angles, which can for example be used to measure dynamical masses of young stellar binaries.[18] Aperture masking on NIRISS will have the be able to observe fainter targets and high precision astrometry of companions to low mass primaries (e.g., M dwarfs) at less extreme contrasts.[19] High resolution observations, especially on NIRISS, will help collect more direct mass measurements to test evolutionary mod-

els. Non-redundant masking is an excellent tool for studying close-in binaries and the inner regions of disks, probing moderate contrasts on high resolution ground-based near-IR imagers, and will reach deeper contrasts with high photometric precision on JWST's NIRISS.

1.2 Non-redundant masking for high resolution, high dynamic range imaging

While aperture masking Fizeau interferometry was demonstrated on sky as early as 1986,[20] the first major scientific result came at the turn of the millennium on the Keck Telescope.[21] Before adaptive optics, aperture masking was a way to beat atmospheric noise by splitting the pupil into a set of unique vector hole pairs (or in some cases a partially redundant pupil). These observations required very fast exposures to remove or reduce blurring of fringes and "freeze" the atmosphere, and therefore required very bright targets. AO stablizes the wavefront over the holes and enables exposure times longer than the characteristic timescale of atmospheric turbulence. Coupled to adaptive optics systems aperture masking has detected accreting protoplanetary material,[22,23] disks around young stars,[24–26] and has studied the distribution of brown dwarf companions to stars,[27–32] among other exciting studies.

1.2.1 Basic Fourier Principles

Every imaging system is an interferometer, where every pair of points in the pupil interfere. In a filled pupil, there is a large degree of redundancy so that individual spatial frequencies cannot be tracked back to one pair of points in the pupil. A non-redundant mask breaks the pupil redundancy by having only a set of unique hole-to-hole vector spacings, at the cost of reduced throughput. Each spatial frequency present in the image can be mapped back to a specific set of holes in the pupil.

1.2.2 Fringe Observables

NRM images are generally analyzed by Fourier methods, with a numerical Fourier transform. In Chapter 2 We present an alternative approach, using an analytic Fourier transform sampled onto detector-scale pixels. For a mask of N holes there are $N(N-1)/2$ complex observables – a phase and amplitude for each hole pair. Fringe amplitude variations probe symmetric structure, while fringe phase probes asymmetric structure.

On the ground, even behind an adaptive optics system, fringe phases are corrupted by large or small variations in the atmosphere and imperfections in the instrument. Changing atmospheric aberrations can obscure the phase signal from a faint companion, for example. In practice, the primary observable in ground-based binary searches with NRM is the closure phase, sets of 3 fringe phases that form a closed triangle. For

closure triangles, hole-based phase errors (e.g. from atmosphere/instrumental effects) calibrate out. Systematic non-zero closure phases can be calibrated by observing a single-star (point source) calibration target and subtracting their measured closure phases.

Squared visibilities also provide information about the extent of a resolved object but can be challenging to measure with high fidelity from the ground. Differential polarimetry provides a calibrated squared visibility observable by using orthogonal polarizations and half wave plate angle rotations to calibrate out variations due to instrument noise. Differential polarimetry is discussed in detail in § 3.2.2, implemented on the Gemini Planet Imager.

Chapter 2

Raw contrast on JWST-NIRISS's non-redundant mask

This chapter presents work published in the Astrophysical Journal in Jan 2015.[33]

2.1 Context

Recent direct detections of exoplanets open a spectroscopic window into the atmosphere and physics of young and adolescent exoplanets. They are an important component for piecing together a complete picture of exoplanetary formation and evolution, and are complementary to indirect detections methods. Young and nearby stars have already been surveyed from a few Astronomical Units of physical separation outwards with direct imaging and coronagraphs on eight meter class telescopes[34–37]

and are being surveyed at even higher contrast with current[38–41] instrument surveys utilizing extreme adaptive optics (ExAO). However, the close environs of young systems in stellar formation regions are only accessible to ExAO systems using interferometric techniques such as non-redundant mask (NRM) interferometry.[22,24,42,43] NRM imaging is fundamentally limited by photon noise, so it yields moderate contrast. By comparison, coronagraphs (which suppress light from the bright central object) are capable of delivering higher contrast than NRM, but their search area does not reach as close in as that of NRM. The two techniques are complementary.

NRM was first used to improve the angular resolution of filled-aperture telescopes.[20,21,44] Its improved dynamic range helped to probe the physics of binaries at moderate contrast ratios.[27,45–48] More recently, NRM observations of star forming regions have discovered structures associated with the birth of exoplanets.[22,24,43] Routine ground contrast ratio limits for NRM are $10^2 - 10^3$ with the deepest contrast being $\Delta L'$=7.99.[49] Today instruments combine NRM with ExAO systems.[50–52] These facilities, together with wide bandpass polarization or integral field unit spectroscopy (IFS) in the YJHK bands on the 8 m Gemini South telescope[4] as well as 2.5–5 μm NRM on the 40 K James Webb Space Telescope's Near Infrared Imager and Slitless Spectrograph (JWST NIRISS),[50,53–55] promise to extend planet formation science by enabling deeper dust penetration at longer wavelengths. These new systems will enable detection of very young (e.g. Taurus-Auriga star forming region), possibly accreting, gas giant planets at small separations.[56]

CHAPTER 2. RAW CONTRAST ON JWST-NIRISS'S NON-REDUNDANT MASK

In spite of the wealth of recent observational results from NRM, the literature does not include extensive discussion of the fundamental and practical limits associated with the technique. Lacour et al. (2011)[42] discussed empirical sensitivity limits of VLT NACO Sparse Aperture Masking (SAM), based on experiments with the image plane fitting routine that we study here. Martinache (2010)[57] showed how NRM can be generalized to full aperture imaging in the high Strehl ratio regime. Ireland (2013)[58] discussed some of the limiting factors of high contrast NRM observations, and Hinkley et al. (2011)[49] conducted deep NRM observations of the known multiple planetary system HR 8799.

The focus of this chapter is two-fold. First, we continue the development of the image plane approach to analyzing NRM data. We address field of view, pixel sampling, plate scale and pupil magnification stability, and some detector properties. We show that this method typically confirms the photon noise and flat field accuracy limits presented by Ireland (2013).[58] In addition, we study other factors that limit NRM contrast — requirements on the spectral type match between a target and its calibrator star, and the effect a finite spectral bandpass has on closure phase errors. Second, we highlight factors that limit JWST NIRISS NRM, which fields a 7-hole NRM.[54] NIRISS has the best pupil image quality of all the JWST instruments,[59] which makes it JWST's best-suited instrument for aperture masking interferometry. In addition, NIRISS's homogenous aluminum bench and optics should help achieve uniform contraction of mechanical and optical surfaces as the instrument cools to its

operating temperature of about 40 K. NIRISS's all-reflective design philosophy also mitigates against chromatic effects, which can be exacerbated by cryogenic conditions. Finally, some relevant properties of NIRISS NRM are described in the Appendix.

2.2 Background

A non-redundant mask (e.g., Figure 2.2) is a pupil plane mask typically located at a re-imaged pupil plane. It possesses several usually identical holes arranged so that no two hole-to-hole vectors are repeated (thus providing a non-redundant set of *baselines* in the pupil). If its holes are circular, with diameter d when projected back to the primary mirror, at a wavelength λ its point-spread function (PSF) or *interferogram* is contained in an Airy pattern envelope with a first dark ring of diameter 2.44 λ/d (Figure 2.1). This envelope is modulated by fringes with half period $\theta = \lambda/2B$ for each baseline. Here B is the hole separation. Figure 2.2 shows the JWST NIRISS mask with seven hexagonal holes, and its PSF.

The Fourier transform of the detected in-focus two-dimensional image intensity array is the array of *complex visibility*, $\mathcal{V}$. Because of the baselines' non-redundancy, the fringe amplitude and phase for each baseline or "two hole interferometer" component in the NRM can be measured unambiguously. The array of complex visibilities for a point source through unaberrated optics is the autocorrelation of the pupil mask. The resulting array of complex visibilities form localized *splodges*[27] of signal in the

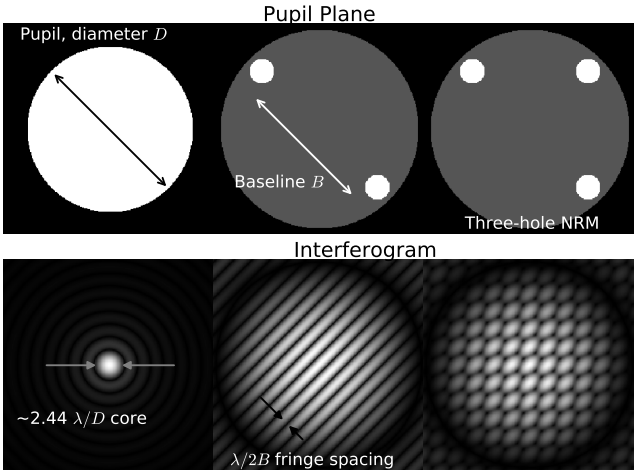

Figure 2.1: Pupil masks and their interferograms. Small holes produce a large PSF envelope, fringed by interference through multiple holes. The longest baselines provides finer resolution than a full aperture. The three hole pupil at right can provide a *closure phase* measurement of a celestial object.

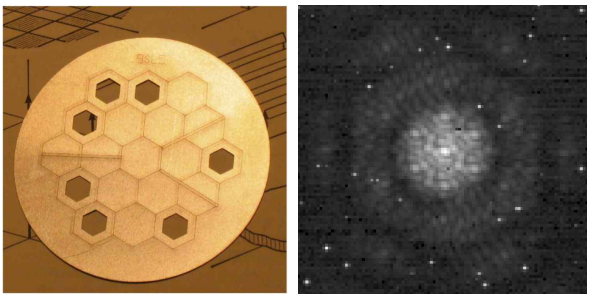

Figure 2.2: Non-redundant mask for JWST's NIRISS pupil wheel[60] and its PSF (or interferogram) with NIRISS F430M from cryogenic vacuum tests in November 2013.[61] The interferogram's fine structure is due to the 21 baselines generated by the 7 holes. The PSF envelope reflects the hexagonal hole shape. Each hexagonal hole maps onto one of the JWST primary mirror segments.

transform domain (e.g., Figure 3.2–bottom) — conceptually one independent splodge (or a splodge and its dependent, Hermitian "mirror splodge") per baseline. Numerical Fourier data analysis approaches measure fringe phases and fringe amplitudes, often at the peak of each splodge amplitude.[21,27] When using a finite bandwidth filter, selecting a single amplitude and phase to characterize a polychromatic fringe implicitly averages over the bandpass. Furthermore, since windowing in the image plane leads to convolution in the Fourier domain, this induces a second form of averaging within a splodge. Our image plane approach avoids this second form of averaging, but it does perform a conceptually similar averaging over the bandpass. In the absence of wavefront aberration, fringe phases for an on-axis point source are zero. Information on source structure is contained in the fringes that are extracted from the image.

The non-redundancy of baselines in the pupil leads to constraints on the complex fringe visibilities. A *closure phase* (the cyclic sum of fringe phases around the baselines formed by three holes (top right, 2.1)) is insensitive to constant wavefront delays (pistons) over the holes. The fringe formed by interference of holes i and j has a fringe phase $\phi_{i,j}$ which is proportional to the wavefront delay between holes $\phi_{i,j} \equiv \phi_j - \phi_i$. For a point source (in the absence of higher order aberrations):[62]

$$\begin{aligned} \Delta\phi_{1,2} + \Delta\phi_{2,3} + \Delta\phi_{3,1} &= \\ (\phi_1 - \phi_2) + (\phi_2 - \phi_3) + (\phi_3 - \phi_1) &= 0 \end{aligned} \tag{2.1}$$

Full-aperture images do not yield closure phases, but sufficiently high Strehl ratio images possess certain constrained linear combinations of phases of the Fourier transform of the image.[57,63] These combinations, or *kernel phases*, are useful for model fitting data when wavefront aberrations are below ~ 1 radian.[57,58,64]

An N-hole mask has $N(N-1)/2$ baselines, $N(N-1)(N-2)/6$ closure phases, and $(N-1)(N-2)/2$ independent closure phases. Empirically, achievable dynamic range is approximately the inverse of the standard deviation of closure phase error, $1/\sigma_{CP}$.[42]

Closure phases of centro-symmetric sky brightness distributions are zero. Binary or multiple point source models are fit to closure phase data to provide information on structure as fine as $\lambda/2B$. Instrumental contributions to closure phases are measured (in principle) by observing a point source. These contributions are then subtracted from a target's closure phases. Instrument stability between target and calibrator leads to improved NRM performance. In addition to fringe phases, a space telescope is likely to provide stable fringe amplitudes. Closure amplitudes (a ratio of amplitudes of fringes formed by four holes[65]) are useful in simple model fitting using space-based NRM data, thereby extending NRM model fitting to include centro-symmetric structure such as circular disks. However, Ford et al. (2014)[66] use simulated noisy NIRISS NRM data to extract the fringe amplitudes and phases which they then use to recreate the input target scene with interferometric resolution. They found that enforcing closure quantities on image plane data leads to an increase in spurious image

artifacts.

Currently numerical Fourier methods are the most common approach to NRM data analysis.[21,22,45,67] This is suited to fields of view that encompass the first few Airy rings of the NRM PSF's "primary beam" (the diffraction pattern of a single hole), and pixel scales that are significantly finer than $\lambda/2D$. Palomar Hale's PHARO, Keck-NIRC2, and VLT's NACO all possess 3-5 pixels per resolution element.[21,68,69,69,70] With such super-Nyquist fine pixellation, Fourier methods easily identify and interpolate over isolated bad pixels.[58]

Diffraction-limited exoplanet imagers deploying state-of-the-art ExAO systems now feed IFSs.[4,5,38] These imaging spectrographs typically have limited fields of view since several detector pixels are required for each image plane pixel spectrum, and the angular extent of each image plane lenslet is at or below the diffraction limit of the telescope, so the instruments are often limited by the number of available detector pixels. NRM on these hyperspectral imagers — Palomar's P1640[51,52] and Gemini Planet Imager[8,50] — must deal with this limitation. An image plane based approach[42,55,71] is insensitive to these restrictions on the field of view.

Future space-based NRM on JWST NIRISS[54,55,60,72,73] is implemented on coarse pixel scales. Under these conditions a numerical Fourier data reduction approach may require more data in order to reduce contamination by bad pixels. This is more relevant to coarse — barely or sub-Nyquist — pixel scales. Dithering to fill the image plane pixels with valid data decreases observing efficiency and complicates estimates

of noise. An image plane based approach sidesteps the requirement of knowing every pixel value in the image. The image plane approach is also robust to detector non-linearities that may occur at the centers of NRM images, since suspect pixel data can be discarded. JWST NIRISS's coarse pixel scales also increase its sensitivity to non-uniform sensitivity within a pixel (intra-pixel sensitivity, or IPS), and pixel-to-pixel variations in IPS.[74] Image plane data reduction can take IPS into account, with a map of measured variations or a model of the pixel sensitivities.[55]

2.3 Image Plane Modeling

We assume the image plane complex amplitude induced by a point source at infinity is described by the Fourier transform of the aperture transmission function (*i.e.,* the Fraunhofer approximation). If functions F and f are a Fourier transform pair, we write $F \overset{F.T.}{\rightleftharpoons} f$. We develop a polychromatic image plane model tailored to JWST NIRISS's seven hole NRM (2.2). Each hole is a hexagon, which, when projected to the JWST primary mirror, has a flat-to-flat distance of approximately 0.8 m. Our model can be adapted to arbitrary hole locations and polygonal hole shapes.[8] Here we treat circular holes with diameter d or hexagonal holes with flat-to-flat distance D (2.3), utilizing a closed form for the Fourier transform of a hexagon,[75] while noting that other more specialized derivations for this exist in the literature.[76] We extend the work of Sabatke et al. (2005)[75] to include limiting values for the

analytical expression's three singular lines and singular central point.

We calculate the monochromatic NRM PSF at a wavelength λ analytically, and construct polychromatic PSFs by summing appropriately weighted monochromatic PSFs on a finely sampled numerical grid. We then bin this finely sampled image to the detector pixel scale to simulate a pixelated noiseless NRM PSF.

We denote the pupil transmission function by $A(\mathbf{x})$. A hole with a transmission function $A_h(\mathbf{x})$ produces an image plane complex amplitude $a_h(\mathbf{k})$ (where $a_h \overset{F.T.}{\rightleftharpoons} A_h$) and a PSF $P = a_h\, a_h^*$ (where * indicates complex conjugation). If the pupil plane vector $\mathbf{x} = (x, y)$ is in units of the wavelength of the monochromatic light, the image plane (or spatial frequency) vector $\mathbf{k} = (k_x, k_y)$ is in cycles across the pupil. $P(\mathbf{k})$ is the *primary beam*, by analogy with radio interferometry, and is the envelope of the NRM PSF. Vector baselines create the finer scale fringing in the NRM PSF.

2.3.1 Circular mask holes

A circular aperture's transmission function is

$$ {}^2\prod(\mathbf{x}) \;=\; \begin{cases} 1 \quad , & r < \frac{1}{2} \\ 0 \quad , & r \geq \frac{1}{2} \end{cases} \tag{2.2} $$

where $r = \sqrt{x^2 + y^2}$. The transmission function of a mask with N identical circular holes centered at $\{\mathbf{x}_i,\ i = 1, ..., N\}$ is

$$A(\mathbf{x}) \quad = \quad \sum_{i=1}^{N} {}^{2}\prod(\frac{\mathbf{x} - \mathbf{x}_i}{d_\lambda}) \tag{2.3}$$

(where $d_\lambda \equiv d/\lambda$). The image plane complex amplitude of an on-axis monochromatic point source observed through this mask is

$$a(\mathbf{k}) \quad \overset{F.T.}{\rightleftharpoons} \quad A(\mathbf{x}). \tag{2.4}$$

Following the nomenclature of phase retrieval work on the Hubble Space Telescope, we call $a(\mathbf{k})$ the *amplitude spread function* (ASF).

Invoking Fourier shift and scaling theorems,

$${}^{2}\prod(\frac{\mathbf{x} - \mathbf{x}_0}{d_\lambda}) \overset{F.T.}{\rightleftharpoons} (d_\lambda)^2 \mathrm{Jinc}(k d_\lambda) e^{-i\mathbf{k}\cdot\mathbf{x}_0} \tag{2.5}$$

where $\mathrm{Jinc}(k) \equiv J_1(\pi k)/2k$ is the transform of the circular transmission function. Here J_1 is the Bessel function of the first kind, of order 1. The phase gradient term $e^{-i\mathbf{k}\cdot\mathbf{x}_0}$ reflects the shift of the hole's origin to $\mathbf{x}_0$.

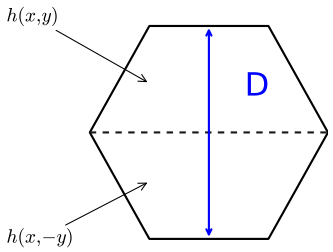

Figure 2.3: We use the convention from Sabatke et al. (2005),[75] where D is the flat-to-flat distance. The hexagon is split into two symmetric parts, $a_{\rm hex}(x, y)$ and $a_{\rm hex}(x, -y)$, whose transforms, $g(k_x, k_y)$ and $g(k_x, -k_y)$ are computed analytically (2.6).

2.3.2 Hexagonal mask holes

We denote the hexagonal hole Fourier transform by $a_{\rm hex}(\mathbf{k})$. Following,[75] $g(k_x, k_y)$ is the Fourier transform of one half of a hexagon that is bisected from one corner to it diametrically opposite corner (2.3):

$$\begin{aligned} g(k_x, k_y) &= \frac{\exp[-i\pi D(\frac{2k_x}{\sqrt{3}} + k_y)]}{4\pi^2(k_x^3 - 3k_x k_y^3)}(\sqrt{3}k_x - 3k_y) \\ &\times \ (\{\exp(i\pi D\sqrt{3}k_x) - \exp[i\pi D(\frac{4}{\sqrt{3}}k_x + k_y)]\} \\ &+ \ (\sqrt{3}k_x + 3k_y)[\exp(i\pi D k_x/\sqrt{3}) - \exp(i\pi D k_y)]) \\ a_{\rm hex}(k_y, k_x) &= g(k_x, k_y) + g(k_x, -k_y). \end{aligned} \tag{2.6}$$

The function g has numerical singularities along three lines, $k_x = 0$ and $k_x = \pm\sqrt{3}k_y$. The limiting behavior along $k_x = 0$ and at the origin is:

$$g \quad (0, k_y) = \frac{e^{-iD\pi k_y}}{2\sqrt{3}\pi^2 k_y^2} \times$$
$$(-1 + iD\pi k_y + e^{iD\pi k_y} - 2iD\pi k_y e^{iD\pi k_y}) \tag{2.7}$$
$$g \quad (0, 0) = \frac{\sqrt{3}D^2}{4}. \tag{2.8}$$

Values along the other two lines can be found by invoking symmetry arguments, and replacement with the appropriate limiting value taken from the $k_x = 0$ line.

2.3.3 Interference between holes

In the absence of wavefront error the ASF of a mask with N identical holes centered at $\{\mathbf{x}_i, i = 1, ..., N\}$ is

$$\sum_{i=1}^{N} A(\mathbf{x} - \mathbf{x}_i) \overset{F.T.}{\rightleftharpoons} a(\mathbf{k}) = a_h(\mathbf{k}) \sum_{i=1}^{N} e^{-i\mathbf{k}\cdot\mathbf{x}_i} \tag{2.9}$$

($a_h(\mathbf{k})$ is a single hole ASF). The mask's point spread function is

$$p(\mathbf{k}) = a(\mathbf{k})a^*(\mathbf{k}) = P(\mathbf{k}) \sum_{i=1}^{N} \sum_{j=1}^{N} e^{-i\mathbf{k}\cdot(\mathbf{x}_i - \mathbf{x}_j)} \tag{2.10}$$

or

$$p(\mathbf{k}) = P(\mathbf{k})\{N + e^{-i\mathbf{k}\cdot(\mathbf{x}_1-\mathbf{x}_2)} + e^{i\mathbf{k}\cdot(\mathbf{x}_1-\mathbf{x}_2)}.$$
$$+e^{-i\mathbf{k}\cdot(\mathbf{x}_1-\mathbf{x}_3)} + e^{i\mathbf{k}\cdot(\mathbf{x}_1-\mathbf{x}_3)} + ...\}$$

(which is real and nonnegative for any $\mathbf{k}$). The flux in this image is the two-dimensional integral $\int NP(\mathbf{k})d\mathbf{k}$, taken over the entire $\mathbf{k}$ plane. We rewrite the PSF as

$$p(\mathbf{k}) = P(\mathbf{k})\{N + \sum_{i<j} 2\cos\left(\mathbf{k}\cdot(\mathbf{x}_i - \mathbf{x}_j)\right)\} \tag{2.11}$$

which shows the separate roles the vector baselines and the primary beam play in the morphology of a point source's interferogram.

Wavefront errors $\{\phi_i,\ i = 1, ..., N\}$ that are constant within each of the apertures decenter each fringe by $(\phi_i - \phi_j)$. Such errors are termed *pistons*. Pistons do not move the image centroid, since the intensity centroid is the mean of the phase gradient over the (uniformly illuminated) pupil forming an in-focus image,[77] and piston errors do not change the mean wavefront slope. A piston difference between two holes shifts the fringe away from the image centroid (or *pointing center*) by an angle, the *fringe phase*. A shift from one fringe maximum to the next is interpreted as an angle of 2π. Given JWST NIRISS' anticipated image quality during normal operations, we expect fringe phases of point source NRM images to lie well inside the half-open interval $(-\pi, \pi]$. This removes any technical difficultes associated with a fringe phase

wrapping around 2π. We stress that fringe phases are not the argument of a 'phasor' associated with the complex amplitude of an electromagnetic wave. The expression for the interferometric PSF in the presence of only piston errors is

$$\begin{aligned} p(\mathbf{k}) &= P(\mathbf{k}) \sum_{i=1}^{N}\sum_{j=1}^{N} e^{-i\mathbf{k}\cdot(\mathbf{x}_i-\mathbf{x}_j)+i(\phi_i-\phi_j)} \\ &= P(\mathbf{k})\Big\{N + \sum_{i<j} 2\cos\left(\mathbf{k}\cdot(\mathbf{x}_i-\mathbf{x}_j)+(\phi_i-\phi_j)\right)\Big\} \\ &= P(\mathbf{k})\Big\{N + \sum_{i<j} 2\Big(\cos\left(\mathbf{k}\cdot(\mathbf{x}_i-\mathbf{x}_j)\right)\cos\left(\phi_i-\phi_j\right) \\ &\quad - \sin\left(\mathbf{k}\cdot(\mathbf{x}_i-\mathbf{x}_j)\right)\sin\left(\phi_i-\phi_j\right)\Big)\Big\}. \end{aligned} \tag{2.12}$$

2.3.4 The JWST NRM PSF

For JWST NIRISS's 7-hole hexagonal mask, (2.12) gives

$$\begin{aligned} p(\mathbf{k}) = P(\mathbf{k}) \ \big\{7 &+ 2\cos\left(\mathbf{k}\cdot(\mathbf{x}_1-\mathbf{x}_2)\right)\cos\left(\Delta\phi_{1,2}\right) \\ &- 2\sin\left(\mathbf{k}\cdot(\mathbf{x}_1-\mathbf{x}_2)\right)\sin\left(\Delta\phi_{1,2}\right) \\ &+ 2\cos\left(\mathbf{k}\cdot(\mathbf{x}_1-\mathbf{x}_3)\right)\cos\left(\Delta\phi_{1,3}\right) \\ &- 2\sin\left(\mathbf{k}\cdot(\mathbf{x}_1-\mathbf{x}_3)\right)\sin\left(\Delta\phi_{1,3}\right) \\ &+ \ldots\big\}. \end{aligned} \tag{2.13}$$

With this closed form rapid calculation of monochromatic and polychromatic PSFs

on a fine scale is straightforward.

2.3.5 Linear fit

Piston differences enter into 2.13 as coefficients of the sines and cosines describing the baselines' fringes. NIRISS's 7-hole mask has 42 such fringe coefficients—$\cos\Delta\phi_{i,j}$'s and $\sin\Delta\phi_{i,j}$'s, which we rename a_{ij}'s and b_{ij}'s, respectively. Two additional parameters are required to match the model to data: the average flux per hole, F, and a DC offset C:

$$\begin{aligned} & F\ P(\mathbf{k})\ \{N + \\ \textstyle\sum_{i<j} \quad & 2[\cos\left(\mathbf{k}\cdot(\mathbf{x}_i-\mathbf{x}_j)\right)\cos(\Delta\phi_{i,j}) \\ & -\sin\left(\mathbf{k}\cdot(\mathbf{x}_i-\mathbf{x}_j)\right)\sin(\Delta\phi_{i,j})]\} + C. \end{aligned} \tag{2.14}$$

These 44 parameters can be estimated from image plane pixel data by using an unweighted *linear* least squares minimization of the quantity

$$||\text{data} - \text{model}(a_{ij}, b_{ij}, F, C)||,$$

and performing a matrix inversion to recover the parameters. We did not detect significant improvent of a noise-weighted fit over an equally weighted fit, so we use

the latter. The piston differences, or fringe phases, are found with

$$\Delta\phi_{ij} = \arctan(b_{ij}/a_{ij}). \tag{2.15}$$

For uniformly transmissive optics throughput, no scattered light, no significant high spatial frequency wavefront errors, and perfect detectors we expect the trigonometric identity

$$b_{ij}^2 + a_{ij}^2 = 1$$

to hold when imaging a point source. Model parameters derived from fitting real data rarely obey this identity. Instead, we obtain the square of the ij^{th} fringe visibility:

$$b_{ij}^2 + a_{ij}^2 = \mathcal{V}_{ij}\mathcal{V}_{ij}^*. \tag{2.16}$$

Target structure further reduces fringe visibility. We calculate fringe visibilities in our simulated data sets by measuring coefficients $\{a_{ij}, b_{ij}\}$. We calculate all 35 possible closure phases in NIRISS's 7-hole NRM. Only 15 of these are independent measurements.

We evaluate our model PSF on a 3×3 sub-pixel grid (unless otherwise noted) so we can study sub-pixel effects, and then bin the array to the detector pixel scale. A full pupil distortion model was not used in this study, although real data will require detailed knowledge of the NRM-to-primary mapping.

A polychromatic model is generated with an appropriately weighted sum of each monochromatic fringe model, given the bandpass profile.

$$model = \sum_{\lambda} F_{\lambda}\ P(\mathbf{k}_{\lambda})\ \{N+ \sum_{i<j} 2[\cos(\mathbf{k}_{\lambda} \cdot (\mathbf{x}_i - \mathbf{x}_j)) \cos(\Delta\phi_{i,j}) - \sin(\mathbf{k}_{\lambda} \cdot (\mathbf{x}_i - \mathbf{x}_j)) \sin(\Delta\phi_{i,j})]\}. \tag{2.17}$$

In the presence of non-zero piston error the model in 2.14 does not fit polychromatic data perfectly, because piston error scales inversely with wavelength. This means that the fringes' coefficients, $\cos(\Delta\phi_{i,j})$ and $\sin(\Delta\phi_{i,j})$, themselves vary with wavelength, but our fit keeps these coefficients constant over the bandpass. The narrower the fractional bandwidth of the filter, the smaller the variation of these coefficients. This problem is common to both the image plane as well as the numerical Fourier approach to NRM data analysis. The least squares solution (2.15 and 2.16) produces an estimate of fringe phase and amplitude that describes some average over the bandpass. We use this estimate in our polychromatic studies.

2.3.6 Applicability of the model

NRM is suited to wavefronts that are smooth over each hole in the mask. Our model assumes flat wavefronts over each hole, which averages over fine wavefront structure in some manner. A Fourier approach windows image data, which also aver-

Filter Name	λ_c	$\delta\lambda/\lambda$	$\lambda/2D$
F480M	4.8	0.08	76
F430M	4.3	0.05	68
F380M	3.8	0.05	60
F277W	2.7	0.25	44

Table 2.1: λ_C is the filter central wavelength, and $\delta\lambda$ is the half-power width of the filter. The Nyquist pixel scale $\lambda/2D$ uses the nominal equivalent area JWST mirror diameter $D = 6.5$. NIRISS's pixel scale is 65 mas.

ages phase and visibility information (since image plane windowing is a convolution in the Fourier domain). However, the two approaches propagate image plane noise differently. We discuss the effects of high spatial frequency wavefront error in § 2.6.

Table 2.1 describes NIRISS NRM filters relevant to exoplanet studies. We study filter bandpass, source temperature, and spectral type effects using our polychromatic PSF model. When using F277W and F380M, NIRISS' 65 mas square detector pixels are coarser than Nyquist-sampled.

2.4 Photon noise, flat field error, and intra-pixel sensitivity

We inserted piston wavefront errors over the holes (Figures 2.2 and 2.4) to examine their effects on simulated monochromatic images. Our pistons are all smaller than $\lambda/4$, which avoids phase wrapping.

We generate monochromatic 4.3 μm images either 3 or 5 times finer than the

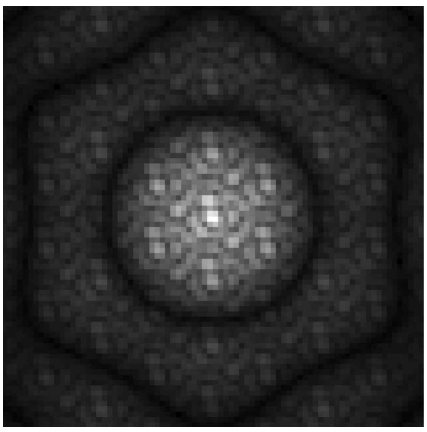

Figure 2.4: Asserting the static pistons from 2.2 in this simulated PSF produce asymmetric features.

Piston in waves at 4.3 μm
+0.02884
−0.06150
+0.12400
−0.02040
+0.01660
−0.03960
−0.04780

Table 2.2: Our simulations use a set of uniformly distributed, random static pistons with a mean of zero and standard deviation 0.06 waves. Anticipated JWST NIRISS rms wavefront error at 4.3 μm is approximately $\lambda/30$.

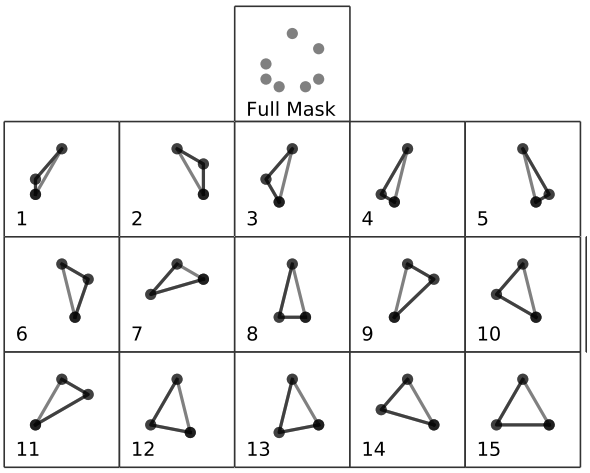

Figure 2.5: Closure triangles: The set of 15 independent closure triangles corresponding to the x-axes in closure triangle behavior inset plots in figures in § 2.4, 2.5, and 2.6, ordered by increasing perimeter length.

NIRISS pixel scale prior to binning to its detector scale and performing a least squares determination of the 44 model parameters. We measure closure phase standard deviation for different noise parameters for a set of 15 independent closure triangles (2.5). In the absence of added noise our measured closure phases were numerically indistinguishable from zero.

We find that the quality of the fit does not change significantly with field of view (i.e. the number of pixels used). We used data within the first dark Airy ring of the primary beam in all simulations.

We distinguish between two types of closure triangle response to different sources of noise or error:

- *Baseline-independent* behavior limits contrast at all spatial frequencies similarly.
- *Baseline-dependent* behavior varies with baseline length and therefore closure

triangle. This behavior preferentially limits contrast at higher frequencies, or smaller angular resolution.

2.4.1 Photon noise limit

We investigate a range of exposures, from 10^4 to 10^{11} photoelectron counts (assuming coadding of multiple exposures regardless of pixel well depth). We calculate the standard deviation of each of the 35 closure phases over 25 independent realizations, and plot the mean of these standard deviations, σ_{CP}, as the solid line in 2.6. Our results are consistent with the[58] result

$$\sigma_{CP} = \sqrt{1.5}\frac{Nholes}{\sqrt{Nphot}}$$

indicated by the dotted line. The inset plot in 2.6 displays the behavior of the closure phases plotted in order of increasing closure triangle perimeter. Photon noise contributes *baseline-independent* error.

2.4.2 Flat field error

We simulated multiplicative flat field error with an arrays of uncorrelated pixel-to-pixel noise drawn from a Gaussian distribution. The standard deviation of the Gaussian distributions range from 0.03% to 3%. 2.7 shows our simulation alongside

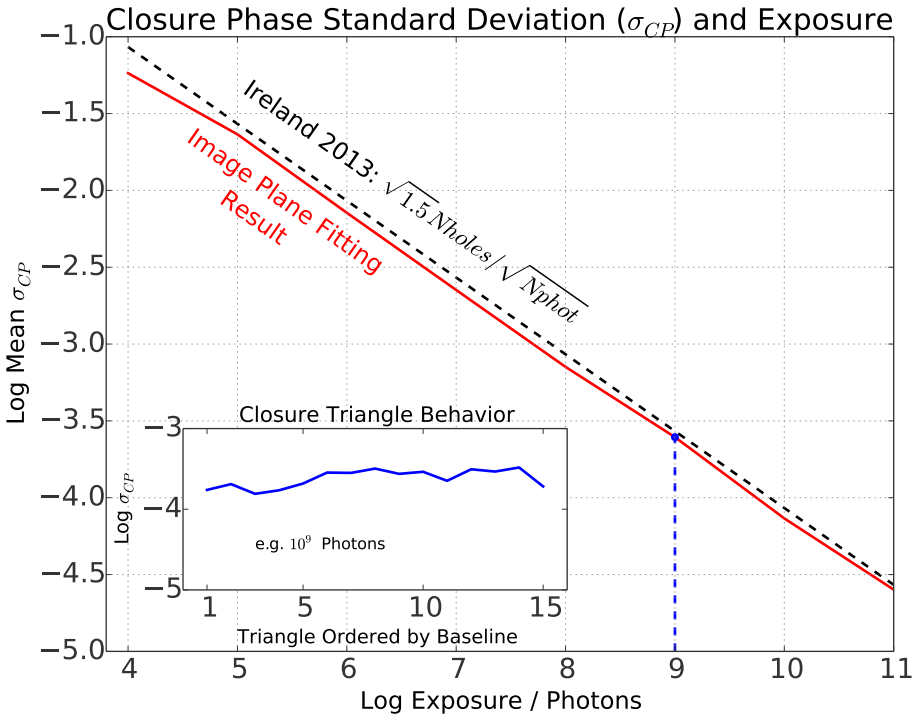

Figure 2.6: Exposure time (monochromatic): The mean closure phase standard deviation for a range of exposure. The solid red line shows our simulation results; the dotted black line displays the noise limit of Ireland (2013).[58] The inset shows one example of σ_{CP} for each of the 15 triangles in 2.5 for an exposure with 10^9 photons. Photon noise induces *baseline-independent* errors.

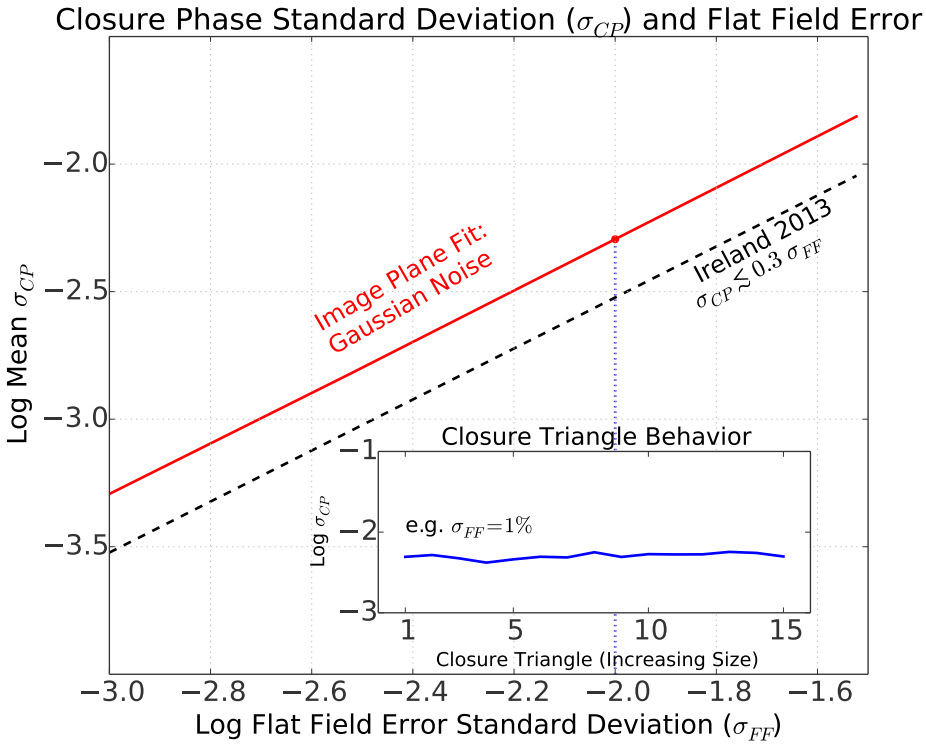

Figure 2.7: Flat field error (monochromatic): σ_{CP}, averaged over closure triangles, is compared to varying uncertainty in flat field, σ_{FF}. The solid red line shows our simulation results. The dotted black line displays a similar numerical result from Ireland (2013).[58] Uncorrelated flat fielding error induces *baseline-independent* errors.

the Ireland (2013)[58] result:

$$\sigma_{CP} \lesssim 0.3\sigma_F.$$

The small offset between the two results may be a difference in number of pixels used or in the way error is modeled. Both results show the same trend. Flat field error is a *baseline-independent* effect.

2.4.3 Pixel-to-pixel variations in intra-pixel sensitivity

We use a data-based model of the NIRISS detector's intra-pixel sensitivity.[74] The pixel has maximum sensitivity at its center, but the sensitivity drops smoothly to 80% ± 5% of its peak at the pixel corners (2.8B–left). We implement a parabolic drop-off of sensitivity within a pixel.

[78] describes a single image (integrated over each pixel) on a detector as

$$I(x,y) = O(x,y) * P(x,y)(\mathrm{III}(x,y) * \mathfrak{R}(x,y)) \tag{2.18}$$

where the image is a convolution of the object, $O(x,y)$ and the PSF $P(x,y)$ multiplied by a sampling function convolved with the intra-pixel response, $\mathfrak{R}(x,y)$. If $\mathfrak{R}(x,y)$ is symmetric it will not contribute phase to the transform of the image. However, the intra-pixel sensitivity is not the same for all pixels, and/or is not symmetric, so is likely to contribute fringe phase error.

Uncharacterized IPS variations are prone to have a larger effect on coarsely sampled images than finely sampled ones. 2.8 compares the effects of sampling frequency when IPS varies from pixel to pixel. We compare the sampling in NIRISS F277W and F430M bands, and GPI H and K bands as illustrative examples.

Here we assume that flat fields are known perfectly, so we use uniform and symmetric pixel-to-pixel weighting in our model (2.8B–left) and fit data with many re-

alizations of IPS drawn from the model we describe above (*e.g.,* 2.8B–right). We renormalize the total pixel efficiency to maintain a constant net sensitivity of each pixel to avoid confounding flat-fielding error with IPS effects. 2.9 shows increasing closure phase error for increased coarseness in pixel scale. Although NIRISS' F277W suffers most from IPS variation, we can still achieve below 10^{-3} radians in closure phase error with the 5% uncertainty in IPS. Fine scale dithering[79] and careful individual pixel IPS calibration could mitigate our sensitivity to worse-than-Nyquist pixel scales. We note in passing that the NIRISS F277W filter presents an interesting science opportunity for faint companion imaging. F277W covers an H_2O absorption feature that could help constrain planet chemistry and dust grain models.[80–82]

IPS modeling can also help determine fractional-pixel positioning of objects on the detector, by cross-correlating image data with analytically generated reference PSFs at different sub-pixel centerings.[55]

2.5 PSF magnification and spectral throughput

Uncertainty in the coordinate scaling of the PSF affects our linear fit. Scaling errors could arise from hole size or central wavelength uncertainty. Coordinate scaling magnifies the PSF envelope and contributes errors, particularly to longer baselines. The PSF magnification in the data can be determined by cross-correlating the power

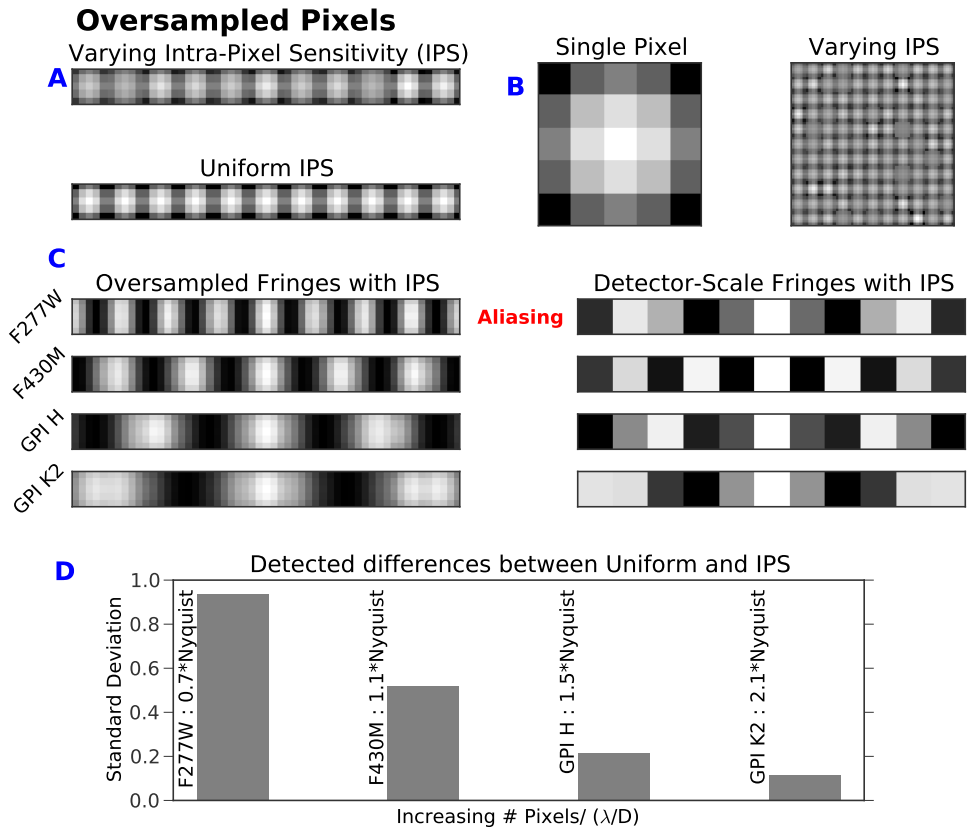

Figure 2.8: Intra-pixel sensitivity: A comparison between uniform IPS and pixel-to-pixel IPS variations[74] on detectors with sub- and super-Nyquist pixellation. **A.** Top left panel shows the sub-pixel sensitivity variation of two rows of 11 pixels, one with uniform IPS and the other with IPS realizations drawn from the statistical model. **B.** A single pixel whose sensitivity drops quadratically to 80% at its corners, and an oversampled map of 11 × 11 pixels drawns from the statistical IPS model. **C.** On the left, a finely sampled fringes (5× finer than the detector sampling) with varying IPS. On the right, the same response binned to the detector scale. At 2.77 μm the sampling is too coarse to detect the fringe peaks, which are aliased — only one peak is visible, though there are actually three. **D.** The difference between image pixel counts for simulated detectors with uniform pixels and varying IPS. F430M (just Nyquist sampled) and F277W (about half Nyquist) show the largest errors. The two well-sampled GPI H and K2 bandpasses show much smaller errors. 2.9 quantifies closure phase errors in these situations.

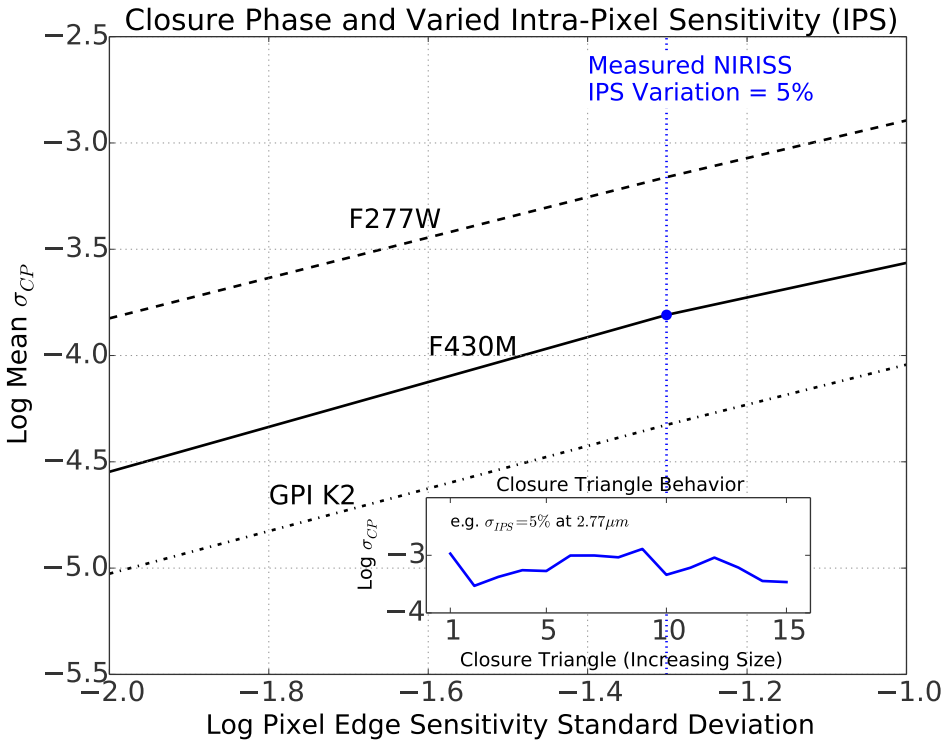

Figure 2.9: Varied intra-pixel sensitivity (monochromatic): Closure phase errors resulting from a range of distributions of IPS. The relative edge sensitivity is varied, while maintaining a uniform net pixel quantum efficiency (see text). NIRISS detector sampling at 2.77 μm and 4.3 μm, and GPI sampling at K2 (2.3 μm) are shown.

spectrum of the data with power spectra of model PSFs created using a range of pupil scales. An NRM can be used to determine plate scale of IFS data cubes, thus providing an independent check of either plate scale or wavelength calibration in the hyperspectral data cubes.[8]

Mask geometry or mask scale uncertainties will contribute errors in the closure phase when there are static pistons. Without static phase errors (*i.e.,* with a symmetric PSF) there should be no error in closure phase. An asymmetric PSF (resulting from static piston error), however, will produce *baseline-dependent* closure phase errors, even when the model perfectly matches the data. We demonstrate that random static phases produce baseline-dependent closure phase error when fitting a polychromatic image, regardless of whether the model is monochromatic or polychromatic. Below about $\lambda/10$ waves (at the central wavelength) rms piston error the closure phase error scales with piston error. The effect is negligible when piston is below small fractions of a wave, when the PSF is sufficiently symmetric. In this section we use pistons that are uniformly distributed with an rms piston of 0.06 waves and zero mean (2.2).

2.5.1 Hole size tolerance

The mask geometry must be known well to fit the diffractive image model to data. We simulate masks with 7 identical holes. We used a Gaussian distribution of mask hole sizes with varied uncertainties and mean hole diameter d, the NRM hole size

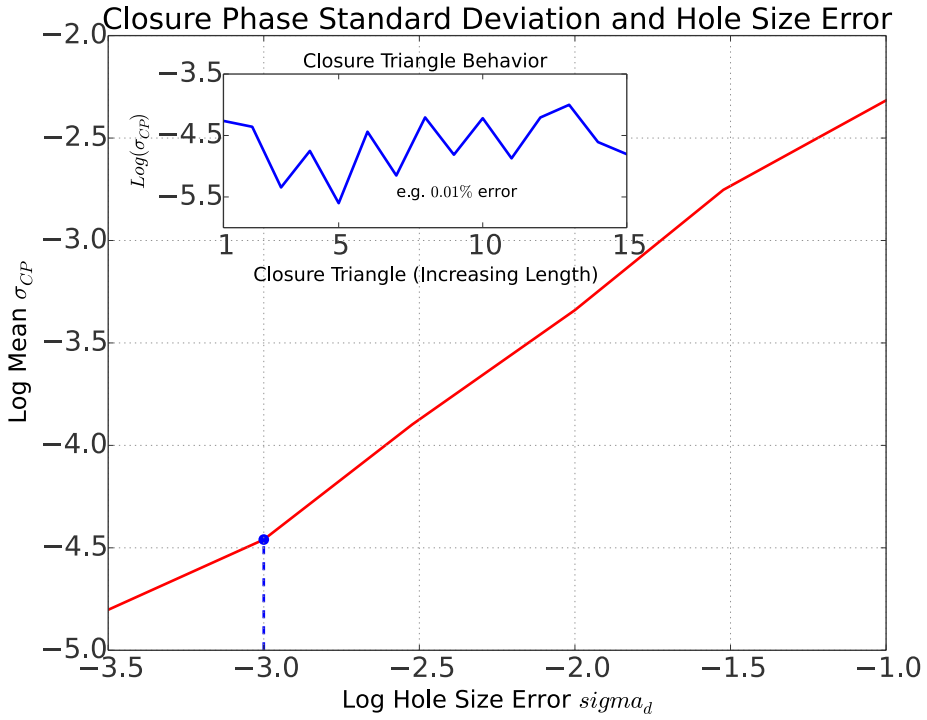

Figure 2.10: Hole size errors (monochromatic): We calculate σ_{CP} with a range of errors in hole diameter. Hole size only affects PSF envelope scaling, which is easily measured in the Fourier plane. Wavelength scales the entire PSF.

for NIRISS. 2.10 compares hole size error σ_d to σ_{CP}. Contrast drops steeply with uncertainty in hole size in the presence of piston errors.

2.5.2 Fitting medium- and wide-band data

NIRISS has three medium-band ($5-8\%$ fractional bandwidth) filters intended for exoplanet science with NRM. Additionally, the wide-band F277W filter (25% fractional bandwidth) may also be scientifically interesting, despite its coarse sampling. 2.11 demonstrates that a polychromatic model matches the data better than

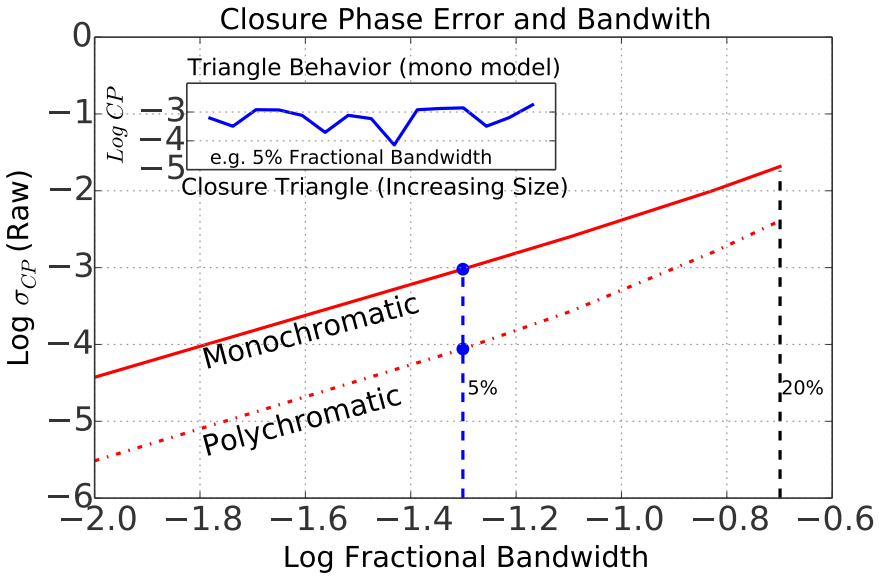

Figure 2.11: Fitting finite bandwidth data: Using a monochromatic model to fit finite bandwidth data achieves our required contrast only when the fractional bandwidth is $\lesssim 1\%$. Using a polychromatic model improves contrast by an order of magnitude. These closure phase errors are *baseline-dependent*, and are highly sensitive to the particular configuration of holes and pistons.

a monochromatic model, by about an order of magnitude. Closure phase errors for finite-bandwidth images with pistons are highly *baseline-dependent*. The errors vary by orders of magnitude between different closure triangles. Closure phase errors also depend on the shape of the bandpass for a given realization of piston errors, when fitting with a polychromatic model. 2.11 suggests that mismatch in central wavelength can introduce large errors in closure phase.

Unless otherwise noted, we use the pistons described in 2.2 in these simulations. When there are no pistons in the pupil, error in the source spectrum should not contribute closure phase errors because the PSF remains symmetric. To explore how much piston affects closure phase error for polychromatic data fit with the model

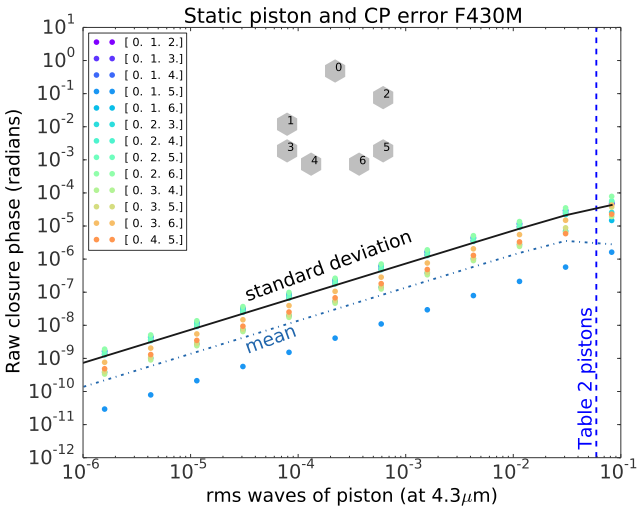

Figure 2.12: Spectrum errors and static piston in the pupil: We measure closure phase for polychromatic data with different levels of piston simulated with NIRISS's F430M filter and fit with a polychromatic model. The dependence is roughly linear when the pistons are below $\lambda/10$ at the central wavelength $\lambda_c = 4.3\mu m$.

described in 2.17, we simulated data with piston at small fractions of a wave and measured the resulting closure phase. The set of pistons in 2.2 were scaled uniformly to preserve the character of the errors while changing the size of the error. Closure phase error scales with the level of static piston up until an rms piston of about $\lambda/10$ (2.12).

Fitting polychromatic data with a polychromatic model will only introduce closure phase errors when there are non-zero pistons in the pupil and the PSF has asymmetries. The gross characteristics of the net throughput (filter $\times$ source spectrum) sets a floor on raw contrast (2.13). This is likely because of the piston averaging mentioned in § 2.3.5. Polychromatic fitting is robust to smaller differences in throughput (e.g. slope) between the model and data.

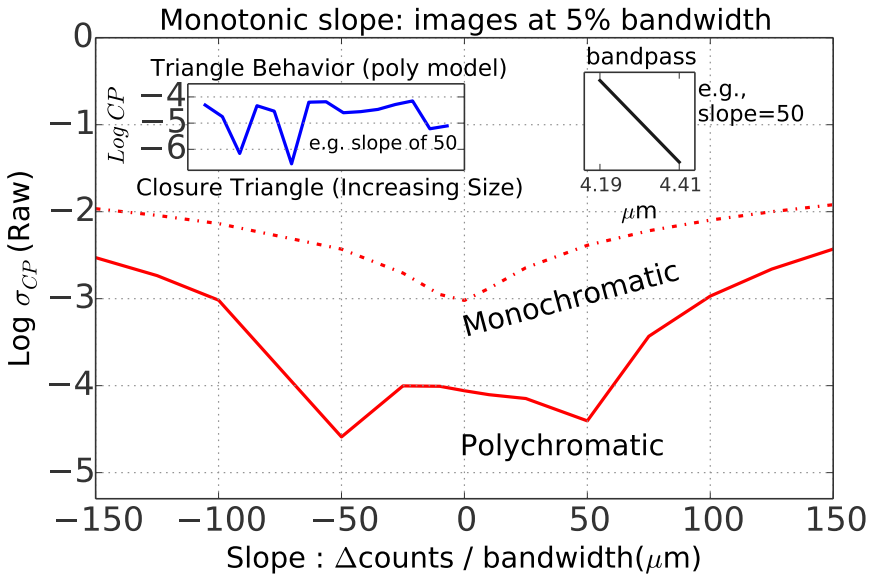

Figure 2.13: Bandpass shape: We fit noiseless polychromatic data generated with bandpasses of positive or negative slopes (difference in counts between the edges of the bandpass) with both a monochromatic model ($4.3\mu m$), and a polychromatic model ($\lambda_c = 4.3\mu m$) matching the bandpass. Surprisingly, the data are not fit best at zero slope with a polychromatic model. The shape of the bandpass can add small but significant errors because of averaging discussed in 2.3.5. Bandpass shape introduces *baseline-dependent* errors.

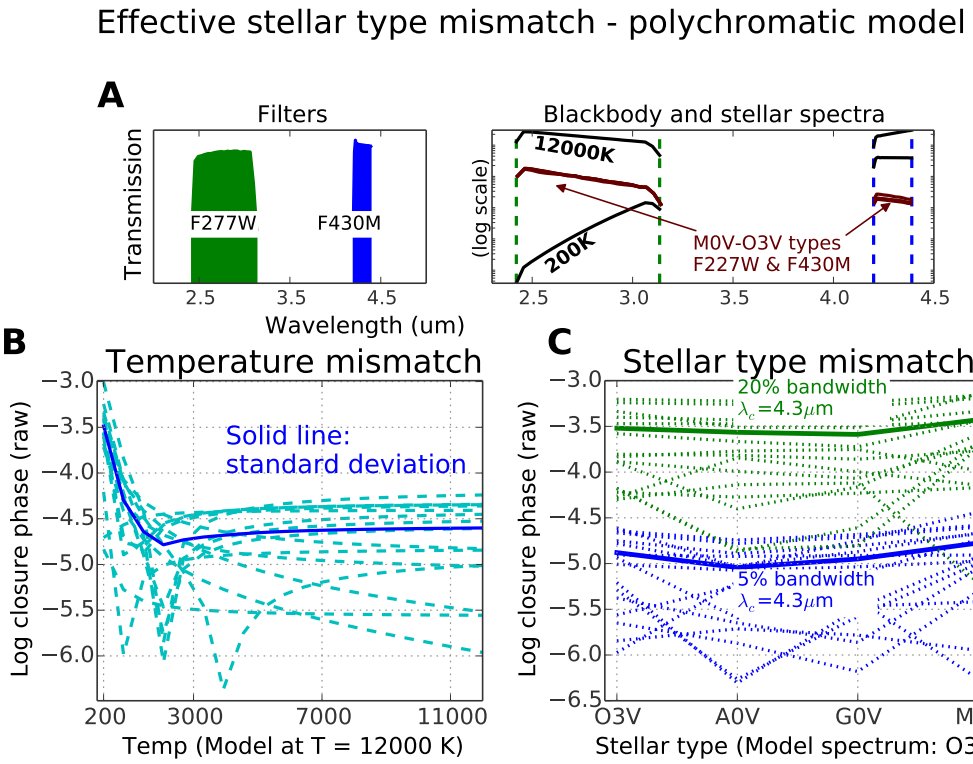

Figure 2.14: Spectrum error (polychromatic): A. Left: Transmission profiles for F430M and F277W NIRISS filters. Right: Spectral profiles seen through the two NIRISS filters: blackbody spectra from T_{eff}=12000K to T_{eff}=200K (subplot B) and stellar-type spectra[83] from M0V to O3V (subplot C). Large changes in spectral type do not strongly affect the slope of the spectrum. **B.** The closure phase error (standard deviation over triangles in solid) plotted against blackbody temperature of simulated polychromatic data. The model temperature is T_{eff}=12000K. Dashed lines represent individual closure triangles. **C.** Closure phase is plotted against mismatch in stellar-type between the model created with an O3V stellar spectrum at a central wavelength λ_c=4.3μm for 5% (blue) and 20% (green) bandpasses. Closure phases for all of 15 triangles are in dotted lines and their standard deviation in solid.

JWST is anticipated to have 80% Strehl Ratio at 2 μm. If its all wavefront error is in piston, piston standard deviation should be about 0.035 waves at 4.3 μm. These values fall below $\lambda/10$ for the F430M filter. We assume that the filter is well known but the source spectrum is not. We investigate mismatch in blackbody spectrum (*i.e.,* temperature) as well as an incorrect choice of stellar spectral type. We generate point source images for NIRISS F430M and F277W at a range of temperatures and stellar spectra, and fit each to either a $T = 12000K$ blackbody or an O3V star model.

2.14A displays the F430M and F277W filter transmissions and range of blackbody curves, from our modeled spectrum at T=12000K down to T=200K. 2.14B displays raw closure phases for all of the 15 independent baselines and their standard deviation from fitting an incorrect blackbody model (T=12000K) to data simulated at our range of temperatures. Similar to the bandpass shape simulation in 2.13, there is an overall throughput shape that yields best sensitivity, though this behavior varies depending on baseline. The polychromatic image plane model is robust to a large error in blackbody temperature, up until the blackbody slope turns over for extremely cool objects (*e.g.,* cooler than 670K at 4.3 μm).

We repeat the same procedure with a range of stellar photosphere models from[83] to examine the effect of stellar type mismatch on closure phase sensitivity. 2.14A shows that the range of stellar spectra from O3V to M0V stars in the two JWST filters do no differ much by slope. We model a flat bandpass centered at λ_c=4.3μm at 5% and 20% to introduce the same rms piston. 2.14C shows the raw closure phase

error when the two models (using stellar type O3V) are fit to this range of spectra. The polychromatic image plane model shows similar robustness to poor knowledge of the stellar spectral type.

Polychromatic model fitting will not be a limiting factor on raw contrast for the narrowest filters with less than 0.06 waves rms piston, but becomes more of a concern for wide-band images, especially at shorter wavelengths. For small piston WFE, raw contrast for NRM with the F277W filter is not limited by the size of the bandpass compared to the effect of intrapixel sensitivity or flat field errors.

2.6 Higher Spatial Frequency Wavefront Error

Wavefront errors can introduce both amplitude and phase aberration in an image. NRM is most effective in the low spatial frequency wavefront error regime; closure phases are insensitive, to first and second order, to piston wavefront error.[58] Wavefront errors on mirror segments often span a range of spatial frequencies. We used WebbPSF[84] to simulate NIRISS NRM PSFs with low to mid spatial frequency wavefront errors, including segment tip and tilt, and figure errors on the segments and instrument optics.

We first explore the contribution of tip/tilt error by introducing randomly oriented tilts on simulated JWST mirrors. In 2.15 each trial has a fixed tilt magnitude, which

we place on 6 mirrors. We require a mean tilt of zero by constraining the last mirror so that we do not actually shift the centering of the PSF. Closure phase errors of 10^{-4} result from segment tilts of the order of half a resolution element.

We also calculated closure phases for 10 different PSF realizations of $\sim$ 140 nm rms optical path delay (OPD) on the JWST primary[85] using WebbPSF (2.15). These sample OPDs do not contain significant segment tilt or global focus. Fitting simulated data with this WFE yields $\sigma_{CP} = 10^{-3.5}$.

2.7 Detecting the companion around LkCa15 with JWST NIRISS

We consider the case of LkCa 15, which has a detected companion inside its disk gap, to compare simulated NIRISS NRM to current ground-based NRM. In 2.16 we plot the theoretical binary closure phase signal for the mask on NIRISS at 4.3 μm and 2.77μm for two flux ratios: 10^{-2} and 10^{-3}. The red stars mark the Keck Telescope K' and L' detections of companion structure around LkCa15, a transitional disk with potential planet-forming bodies.[22] The LkCa15 detections fall between $0.5\lambda/D$ and λ/D for 2.77 μm (D referring to longest baseline), and are detectable with contrast better than 10^{-3}.

The F277W filter, at shorter wavelength, will access smaller inner working angles, relevant to following up close companions detected with large apertures on the ground.

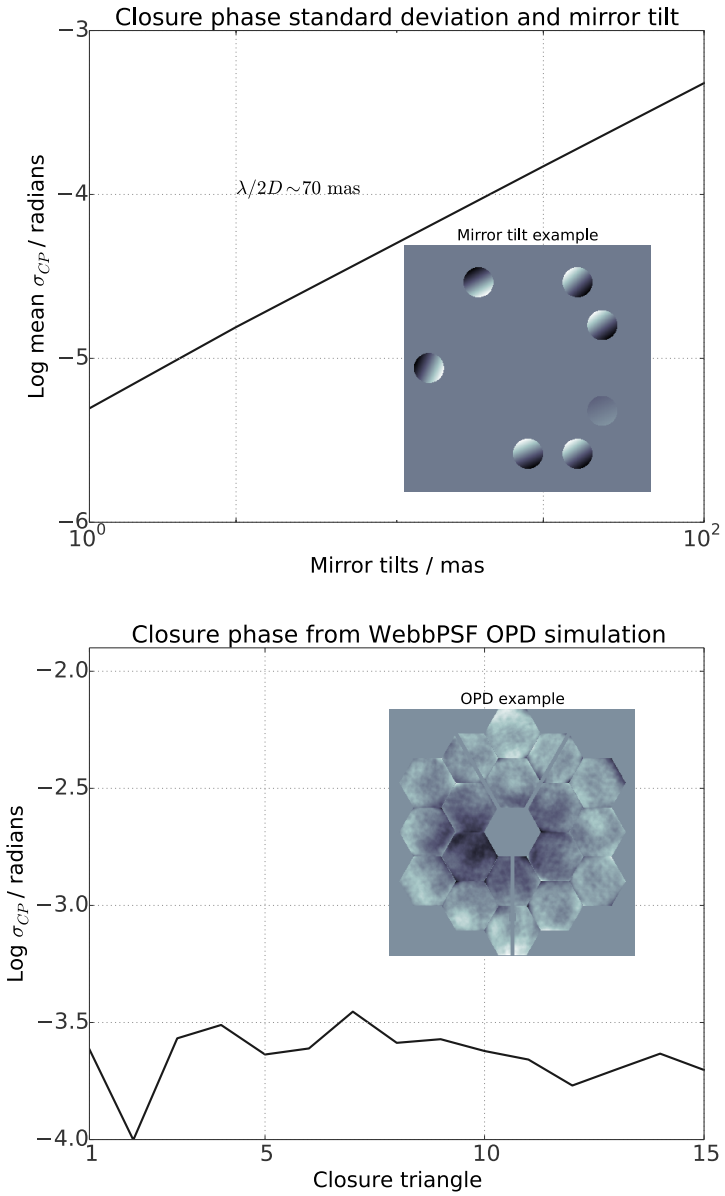

Figure 2.15: Tilts and higher order wavefront error: *Top:* We measure σ_{CP} from 100 different tilt error simulations of various sizes of tilt. An instance of tilt over each hole is inset in the top panel. *Bottom:* σ_{CP} from fitting 10 different ~ 140 nm rms JWST NIRISS wavefront realizations containing higher order wavefront error.[85] PSFs were generated with WebbPSF software.[84]

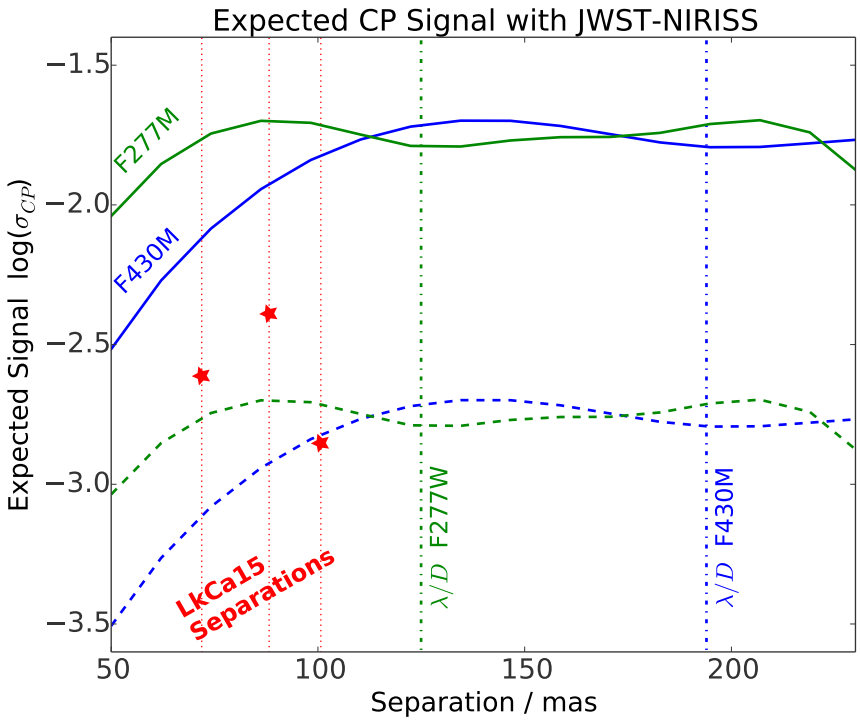

Figure 2.16: LkCa15 with JWST NIRISS: The theoretical closure phases for a single binary companion predict a required contrast $\approx 1/\sigma_{CP}$ empirically. The plot shows σ_{CP} over all possible triangles through NIRISS F277W and F430M filters. If F277W observations can reliably measure closure phase below 10^{-3}, they could detect the K' signal of the companion structure around LkCa15, according to.[22] Two of their three companion sources lie between $\lambda/2D$ and λ/D at 2.77 μm.

Following our analysis in 2.4–2.6, we conclude that F277W would be able to achieve raw contrast of 10^{-3} with good flat field measurements and IPS characterization. With this performance NIRISS would be able to detect the LkCa15 companion signal in a routine observation.

At $2.77\mu m$, $\lambda/2B \sim 88$ mas for NIRISS NRM. Detections this close to the diffraction limit maybe challenging from a modeling perspective. The anticipated stability of NIRISS NRM's visibility amplitudes may help in breaking contrast-separation degeneracies more securely than in similar ground-based data. Multi-band observations may also help resolve degeneracies between separation and contrast. While the angular separation LkCa15's companions may still pose a challenge, NIRISS will likely achieve better contrast than ground-based NRM.

2.8 Discussion and Recommendations

Our analysis of the limits on raw contrast helps develop instrument tests, calibration needs, and observing strategies for JWST NIRISS. We applied our analytic model to NIRISS' cryogenic test data.[61] The necessary conditions for 10^{-4} closure phase error with NIRISS NRM depend strongly on detector behavior and other instrument and telescope details. Instrument characterization and accurate pointing and dithering, coupled with point source calibration of science target data could help achieve this contrast goal for routine NIRISS observations. Because of thermal drift and the

planned occasional wavefront control activity in flight,[86–88] near-contemporaneous acquisition of target and point source calibrator data is desirable. Since NIRISS point source calibration involves system-wide complexities we defer study of it here. NRM paired with the sub-Nyquist sampled F277W filter should provide about 7.5 magnitude raw contrast, which could be useful for probing water absorption features.

Identifying outlying image pixels is straightforward with our analytical model fit. Our algorithm also makes for more efficient observing strategies since missing pixel data do not need to be filled in with dithered observations. Pixel-to-pixel variation in sub-pixel scale differences is easily incorporated in a statistical or detailed manner in our model fit approach, and saturated pixels can be ignored in the fit. This is relevant to NIRISS, with its barely-Nyquist pixel scale and JWST's limited lifetime.

Flat field errors of 0.1% limit raw monochromatic contrast to a few $\times 10^{-4}$. Precise positioning of the target and calibrator on the same pixel will reduce the effect of flat field errors.[72] Knowledge of intra-pixel sensitivity can be used to improve astrometry and reduce fringe phase measurement errors.[55] Intra-pixel sensitivity (IPS) variations over the detector limit contrast, especially for the shorter wavelength NIRISS F277W and F380M filters. However, knowledge of the IPS can ameliorate this. We demonstrated that a statistical understanding of IPS variations can help markedly. As with flat field errors, repeated placement of targets to sub-pixel accuracy will benefit NIRISS NRM's contrast.

Small scaling errors may introduce closure phase errors when there are static piston

in the pupil. Matching magnification between data and model is straightforward in the Fourier domain. For instruments that have IFSs, this technique can be used either for wavelength or for plate scale calibration of individual hyperspectral cube slices.[8]

NIRISS NRM data analysis in the image plane will benefit from polychromatic modeling. The necessary piston averaging at the band's central wavelength will contribute closure phase errors when there are non-zero pistons in the pupil. However, the modeled bandpass is fairly robust to errors in source spectrum, as long as the spectrum slope sign is correct. Raw contrast from F277W observations will be reduced because of its wider bandpass, and because F277W will see higher instrument WFE at its shorter wavelength. However, with the anticipated WFE for JWST, its bandpass should not be the limiting factor for contrast.

The primary contrast limiting factors are pixel-to-pixel (flat field) variations and IPS variation for the coarsest sampled F277W filter. In comparison contrast will be largely unaffectected by uncertainty in source spectrum if the modeled bandpass roughly matches the data. While these various systematics limit raw contrast, additional sensitivity will be possible through point-source calibrations and leveraging stable closure amplitudes.

Flat field errors can also effect closure phase measurements from IFS images. but higher order wavefront error from atmospheric effects may be the biggest limiting factor on the ground. These higher order errors certainly exist on ground-based instruments like GPI, and may contribute amplitude as well as phase errors. JWST

NIRISS' wavefront error is expected to be dominated by low order terms, and stay below about 160 nm rms. Fitting uncorrelated pistons with our analytic model is robust to low-order wavefront errors including tip and tilt. A thorough study of the effects of higher-frequency wavefront error in the NRM PSF is warranted.

Space-based NRM presents opportunities for extended object imaging at high angular resolution. Centro-symmetric structures require amplitude measurements, which will be stable in the absence of atmospheric effects. Space-based NRM's fringe phase and amplitude measurements provide true imaging, which can benefit AGN and quasar science 2014ApJ...783...73F, so our image plane model could improve observing efficiency and data reduction methods for space-based high resolution imaging. An analytic point source model is a step towards more sophisticated forward-modeling of NRM data.

Chapter 3

Commissioning GPI's Non-Redundant Mask

3.1 Gemini Planet Imager AO and Optical Path

Outlining the AO system and optical path of GPI are essential to understand the subtleties of its NRM performance. Figure 3.1 is a diagram of the light path through GPI and its wavefront correction stages. Light enters GPI's AO system, which consists of two deformable mirrors (DMs) – the woofer that corrects low order corrugations and the tweeter that corrects the high spatial frequency aberrations. The light is split part into the sensing leg of the AO system and part into the rest of

the instrument. GPI's wavefront sensing is done with a Shack-Hartmann wavefront sensor, an array of lenslets in front of a visible light CCD camera, looking for offsets from center in focus of each lenslet. The lenslets map to the actuators on the tweeter DM. The light that continues through the instrument first passes through the Pupil Plane Mask (PPM) wheel, which contains the coronagraphic apodizers to truncate the wavefront, as well as a 10-hole non-redundant mask. The light continues on to the Focal Plane Mask (FPM) wheel preceding the Calibration (CAL) system. In coronagraphic mode the FPM is a mirror with a central hole as the occulter. The light passing through the occulter is sent to a tip/tilt sensor and additional higher order calibration unit. For NRM mode, no light is sent to the CAL system, so the NRM mode does not benefit from low-order tip/tilt correction. Following the CAL system, light enters the Integral Field Unit (IFU) spectrograph or polarimeter, where an array of lenslets at the focus send the light through either a dispersing prism for spectroscopy at each image pixel or Wollaston prism to measure polarization at each image pixel, respectively.

This instrument is designed to work best in coronagraphic modes. The NRM and direct exposure modes of operation do not benefit from CAL tip/tilt sensor correction or any high order CAL corrections. The commissioning of the NRM was plagued by a low order jitter in the image centroid that could not be sensed by the CAL. This, along with detector overheads of 20s per exposure made the problem difficult to diagnose.

The large number of optics in between the AO system and the science detector

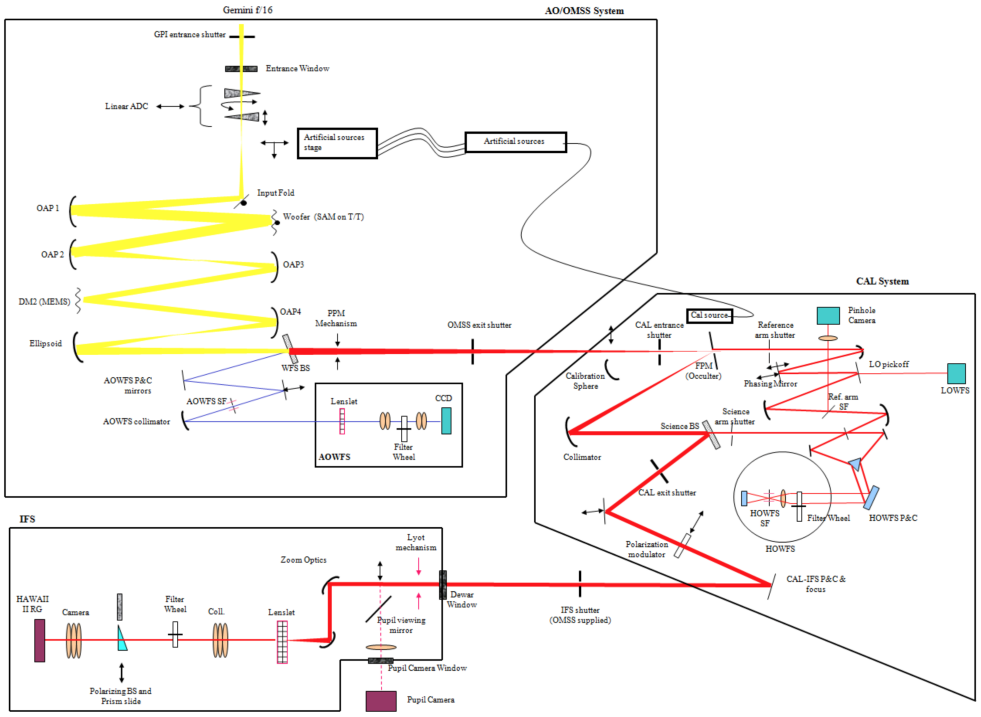

Figure 3.1: GPI's Optical Path

introduce non-common path aberrations (NCPA) that cannot be corrected in closed-loop AO. In Chapter 6 we demonstrate how the NRM and direct modes can be used to measure NCPA, in order to improve the NRM performance.

3.2 NRM + IFU

The Mask[89] operates in both spectral and polarization IFU modes. Given the default pipeline reduction that yields 37 cube slices for a wavelength dispersed extraction, each slice is $< 1\%$ $\delta\lambda/\lambda$ so a monochromatic approximation is appropriate and Fourier transform splodges are round. For polarization extractions the bandpasses

range from roughly 12% to 19% and the transform splodges (complex visibilities) are radially smeared.

3.2.1 Integral Field Spectroscopy + NRM

GPI has an integral field spectrograph in YHJK bands that splits each image into wavelength channels across the band with spectral resolution R$\sim 35 - 80$.[90] GPI's spectral mode with its NRM is best suited for detection and characterization of binary companions (whether stellar, sub-stellar or planetary mass). The multiple wavelength channels provide an extra axis to constrain NRM detections of binary companions. The J and K bands are windows to spectral features linked to accretion. Accretion properties with the overall spectral shape over these NIR bands can help constrain the effective temperatures of these cool bodies.

Spectral Mode

Observational calibration follows the traditional approach of using a point source calibrator to subtract out instrument effects and leverages the spectral slices to gain better detection sensitivity. Differential phase has not yet been tested for the May commissioning data, this analysis is still in progress.

Fitting the data is relatively straight forward, using the analytic solution for a binary systems of unequal brightness. We use Markov Chain Monte Carlo (MCMC) to find the best parameters.

3.2.2 Integral Field Polarimetry + NRM

GPI can also operate with a Wollaston prism, splitting the light at each image pixel into two orthogonal polarization channels. These polarimetry mode images are broadband (*i.e.,* YJHK). GPI polarimetry with its NRM is best suited for studying disks on small angular scales inaccessible to coronagraphs. NRM with polarimetry produces a unique observable, the differential visibility.[9] In GPI, two orthogonal polarizations split by the Wollaston prism and 4 half wave plate (HWP) angle rotations. In this case there are 2 layers of differential calibration. First between orthogonal polarization channels and then between orthogonal half waveplate angles (HWPA). In a typical observation a single sequence will consist of 0, 22.5, 45, 67.5 HWPAs. The differential observables are as follows:

$$\begin{aligned} CP_{ortho-diff} &= CP_{channel1} - CP_{channel2} \\ V_{ortho-diff} &= \frac{V_{channel1}}{V_{channel2}} \end{aligned} \tag{3.1}$$

Then one proceeds with HWP rotation differential measurements, for example between HWPAs of 0 and 45 degrees:

$$\begin{aligned} CP_{0-45} &= CP_{diff-0} - CP_{diff-45} \\ V_{0-45} &= \frac{V_{diff-0}}{V_{diff-45}} \end{aligned} \tag{3.2}$$

The same is repeated for 22.5 and 67.5 HWP angles. These differential measurements can be compared with models to reconstruct the resolved structure. An unresolved source should be observe as a reference source.

The modeling for extended sources is less straightforward than for binaries. radiative transfer modeling codes (e.g. MCFOST,[91] Hyperion[92,93]) may be used to simulate the physical structures resolved by the NRM in an MCMC approach to fitting.

3.3 GPI's non-redundant mask

The Gemini Planet Imager has one 10-hole non-redundant mask that sits in the PPM wheel.[89] There are $\frac{N(N-1)}{2}$ baselines formed by the g10s40 configuration.

Table 3.1: Mask hole dimensions measured in mm from center.

X	Y
-1.061	-3.882
-0.389	-5.192
2.814	-0.243
3.616	0.995
-4.419	2.676
-1.342	5.077
-4.672	-2.421
4.157	-2.864
5.091	0.920
1.599	4.929

Hole diameter: 0.920 mm
Gemini S outer diameter (OD): 7.770 m (after baffling)
Apodizer OD in this re-imaged pupil plane: 11.68 mm

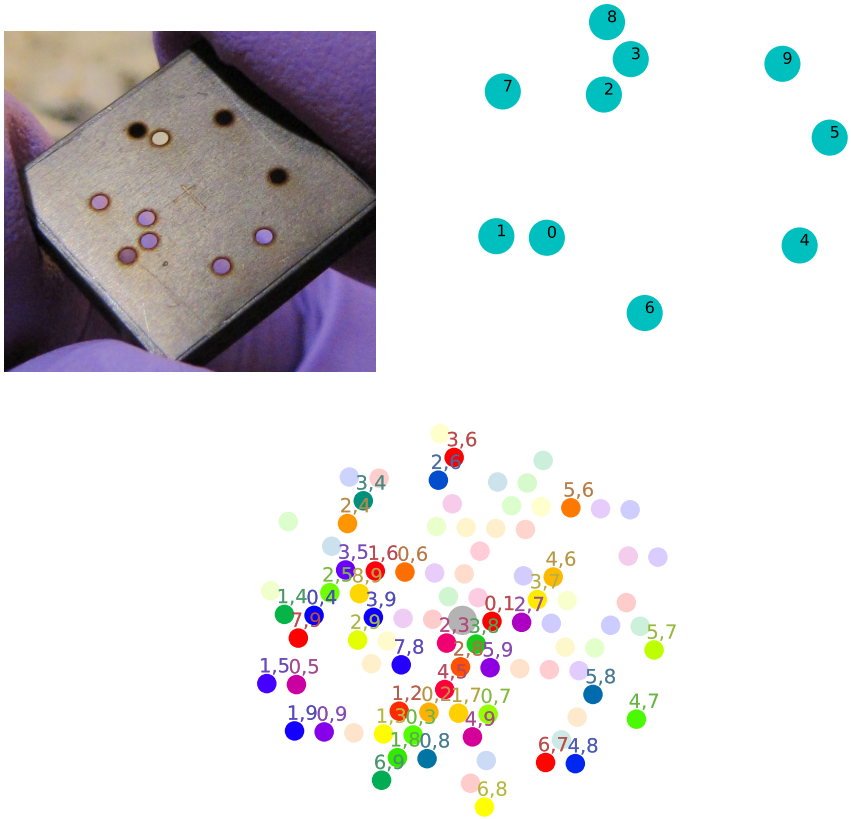

Figure 3.2: Labeled Holes and Splodges: **Top Left:** GPI's 10-hole NRM.[50,94] **Top Right:** We establish a numbering convention, which helps to keep track of hole and baseline dependent systematics and aids diagnosis of problems, shown in the center. **Bottom:** We plot the *splodges*, or associated hole-pair baselines (with their complex conjugate "reverse baselines" in lighter color).

3.3.1 GPI filters and sampling

The NRM sits in the Pupil Plane Mask (PPM) wheel, which houses the coronagraphic apodizers, and operates with all Y-K2 filters in either spectral or polarimetry mode. The longest NRM baseline projected onto the primary is 6.68 m. Assuming a pixel scale of 14.14 mas the mask is Nyquist sampled at 0.92 μm, supporting well-sampled images throughout nearly the entire spectral range of GPI.

3.3.2 Exposure time calculator

A major goal of commissioning was to pass light through every filter with the NRM. To estimate the exposure time for future observations, we recorded the peak value in every raw image. This value should not exceed 16000 counts to remain in the linear regime for the detector. We adopt 14000 counts as a conservative limit. There is a known focus error in direct exposures (non-coronagraphic). We note that focus error can affect the peak counts in the PSF.

We found a lot of variation in peak count value and exposure time. This could be due to vibrations encountered throughout the night. From the majority of May 2015 observations we formulate the following empirical ETC:

$$\frac{Peakcounts}{\gamma \frac{BAND}{MODE}(10^{mag/2.5})} \tag{3.3}$$

Here γ is an empirically estimated constant, $BAND$ is the relative throughput of each band, $MODE$ is the relative number of pixels on which the light is dispersed

for the spectral or polarization modes, and mag is the apparent magnitude in the observing band. Figure 3.3 shows the measured vs. expected counts for a selection of observations using this ETC. For this we assigned the following:

$$\begin{aligned} \text{gamma} &= 50000 \\ \text{throughput bands Y, J, H, K1} &= 1.0 \\ \text{and K2} &= 0.75 \\ \text{MODE}_{\text{PRISM}} &= 5/17 \\ \text{MODE}_{\text{WOLLASTON}} &= 1.0 \end{aligned}$$

We place a brightness limit of $mag \sim 2.7$ in all bands for the polarization mode and $mag \sim 1.6$ for all bands in spectral mode. This may be modified with data in better conditions and without the presence of vibrations.

3.4 Pupil positioning

It is important to check that the NRM is not vignetted by GPI's pupil stop, and that the holes are evenly illuminated. We determined the mask position in the pupil with a few custom poke patterns on the MEMS tweeter the deformable mirror, while illuminating the pupil with the internal source and imaging with the pupil viewing camera. One asymmetric set of pokes helped determine the rotation between the the MEMS DM (Figure 3.4) and the pupil to help map the NRM holes to actuator locations. The rotation between the poke pattern and the as-designed NRM orientation (with respect to the MEMS DM) is roughly 243.6 degrees counter-clockwise. Another set confirmed a new aligned position of the mask.

Figure 3.5 shows the NRM in its nominal position from the pupil viewer (a) and

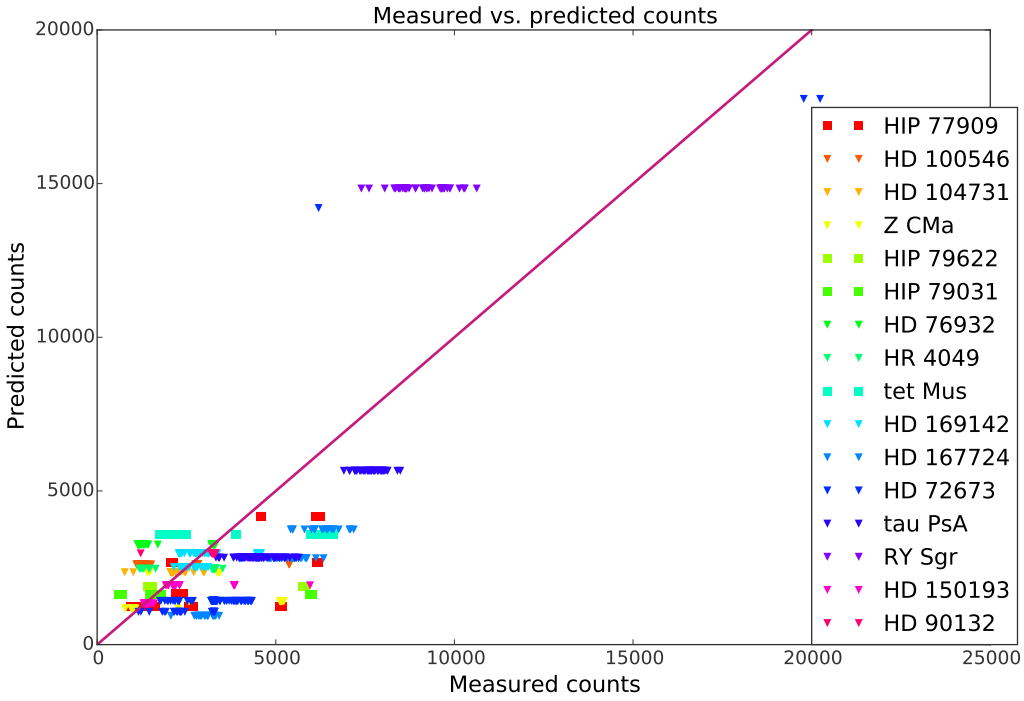

Figure 3.3: Peak counts in May 2015 observations. We compared measured peak counts to our empirically determined ETC. Triangles represent polarization mode, squares represent spectral mode. The variation in measurements could be due to a range of vibration conditions. The solid line plots 1:1 correspondence between our ETC and the measured peak flux. Outlying exposures are likely due to increased vibrations or resolved structure.

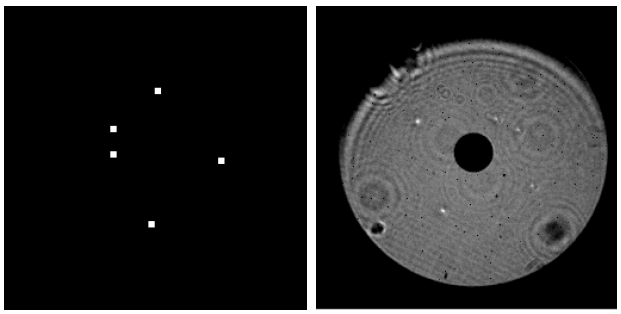

Figure 3.4: Left: asymmetric 5-poke pattern on the 48×48 GPI MEMS actuator array. **Right:** The resulting pupil image. The pupil image is vignetted at the top, a result of miaslignment of the pupil-sensing camera, not the science path. The pupil viewing camera also shows other features like dust on the camera and bad actuators.

overlaid on a clear pupil image (b). A few holes appear to be clipped, but since the pupil viewer optics vignette the on-axis beam it is difficult to determine the edge location. The secondary obstruction provided a good handle on the pupil center and which holes were cut off at the edge. We shifted the mask from the nominal position to lie entirely in the pupil. Figure 3.6 shows a poke pattern of NRM hole centers mapped to the deformable mirror actuators, and as seen through the mask in the pupil. A set of NRM-specific pokes (Figure 3.6) confirmed the new hole position mapping to the MEMS plane and confirmed our alignment. The actuators covered by each hole are obvious and can be used to track back peculiarities in the AO control. We confirm that the holes miss spiders and known dead actuator locations, as designed. The dead actuators are indicated in masked regions at the top of Figure 3.6.

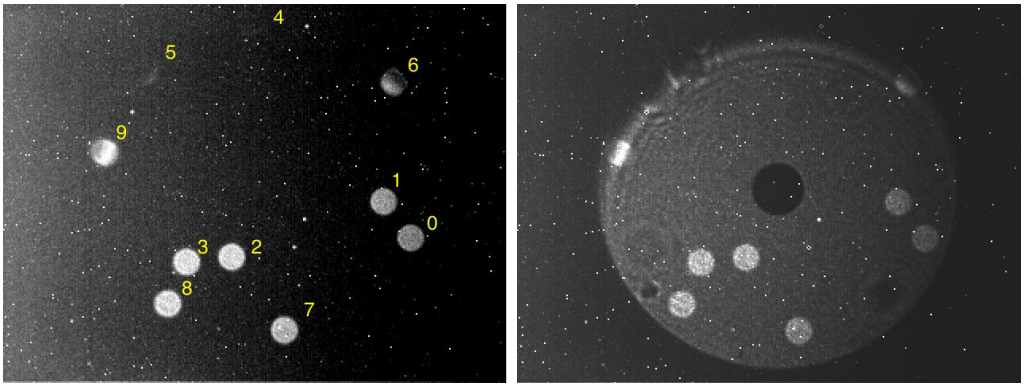

Figure 3.5: Left: The nominal alignment of the NRM seen with the pupil viewing camera. Holes 4 and 5 look completely cut off, hole 6 partially. **Right:** Pupil viewer images of the NRM and overlaid with the clear pupil show vignetting by the pupil viewing system.

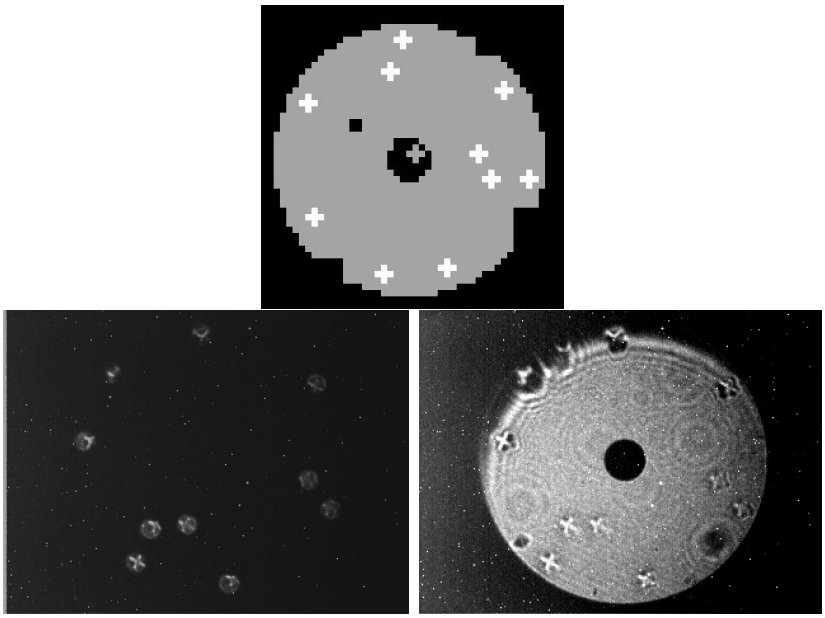

Figure 3.6: Top: The expected NRM hole centers (white crosses) overlaid on the bad actuator map of active subapertures (gray). **Bottom left:** The poke pattern seen through the mask moved to its new position. **Bottom right:** The poke pattern seen through the clear pupil. The NRM hole centers miss known bad actuator locations.

3.5 Early NRM Data

As a demonstration, in December we observed known binary HR 2690 in H band. We recovered the companion at separation of 88.4 ± 0.5 mas and contrast ratio of 5.94 ± 0.09. We recovered the companion in 24 minutes of data. Section **??** discusses a current estimate of detection limits for short exposures.

Despite a few outstanding instabilities, GPI's NRM is capable of high dynamic range measurements, competitive with masking modes on older instruments. In long exposures where pointing jitter smears the data, variations can be calibrated if enough data are taken. In the most stable conditions on the telescope from the internal source

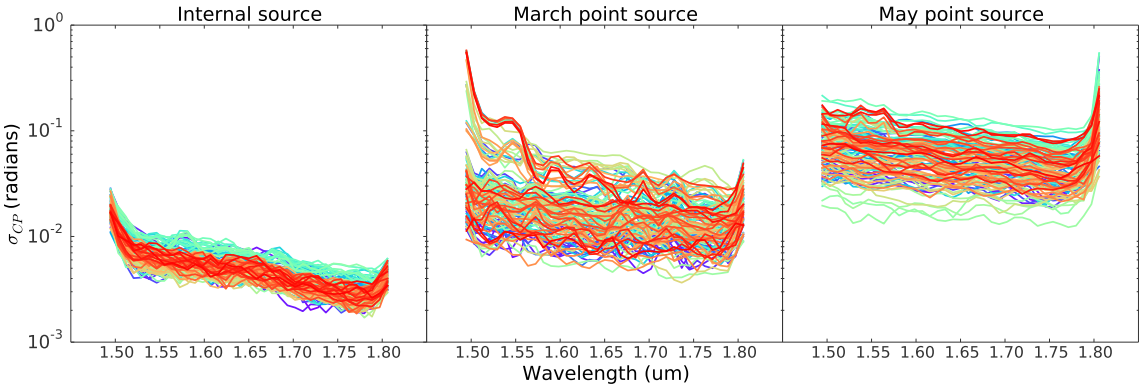

Figure 3.7: Perfomance: Closure phase standard deviation from internal source exposures on the telescope. Phases are very stable and predict raw contrast as low as several $\times$ 10^3 for similar conditions. On sky in March closure phase error was roughly an order of magnitude higher, and in May even worse. March and December had clear conditions while May had thin and thick cirrus. We reject 3 frames showing visible smearing in the May dataset for this calculation.

(without atmospheric turbulence) closure phase is stable, a median standard deviation of 0.0046 radians in H band (uncalibrated). In Figure 3.7 we plot the closure phase error with wavelength for the internal source compared with measurements on sky in March and May 2014.

In March 2014, short exposures saw relatively stable closure phases that had a median standard deviation 0.016 radians, uncalibrated. These closure phases roughly follow the wavelength trend seen in July 2013 lab data[95] and in exposures with the internal source. Observing conditions were worse in May and observations saw increased pointing jitter (Figure 3.8). The median standard deviation in closure phase was 0.055 radians. This could be an explanation for larger error in the closure phases, decreased contrast sensitivity. In Figure 3.7 the three most visibly smeared frames from are not included in analysis.

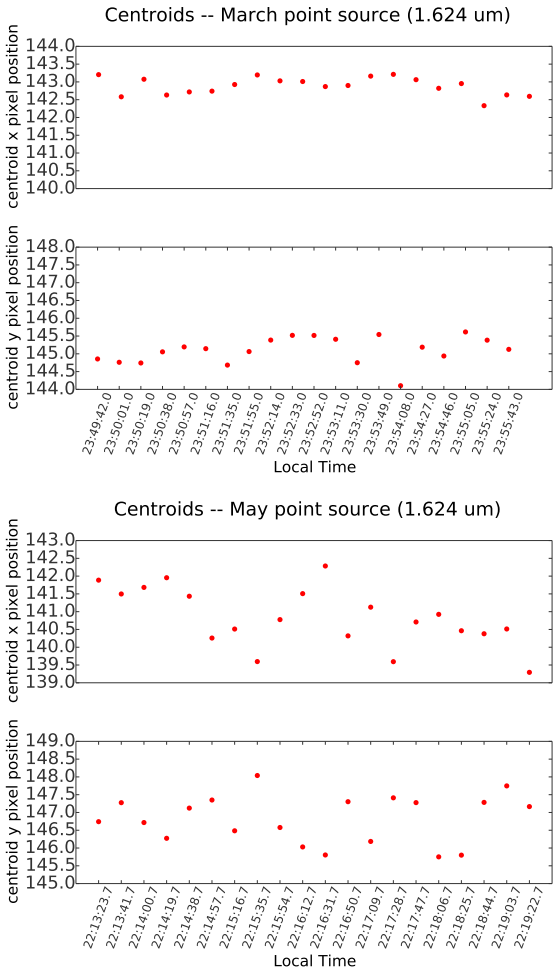

Figure 3.8: Image centroid position with time: Both March and May 2014 runs looked at the same point source for 1.5 s exposures, approximately 20s apart due to the integration time of the camera. Both show some jitter in the pointing. The pointing stability appears worse for the May run, consistent with higher wind speeds and poorer observing conditions.

Analyzing the data through the Sydney pipeline, March 2014 short exposure closure phases had a median standard deviation of 1.57 degrees for each group of 10 frames after calibration, allowing detections of point sources at up to 6.5 magnitudes. In the 17 exposures in May 2014, calibrating the first 9 frames with the remaining frames the root-mean-square (rms) of the calibrated closure phases was 1.62 degrees. This would provide robust detections at up to 6 magnitudes. These results suggest the current performance of GPI NRM is similar to that obtained routinely with older instruments such as NIRC2 at Keck and NACO at VLT. However, the extra wavelength dimension provides more independent data per frame than is obtained with these instruments, resulting in higher contrast detection limits with the same number of frames and similar closure phase scatter.

3.6 Vibrations and polarimetry

NRM polarimetry can help resolve close in polarized structure in disks that is beyond the reach of GPI's coronagraph. This includes the edges of inner disks in protoplanetary systems, often inferred by SEDs but not necessarily directly. This kind of information can shed light on the architecture of planet forming regions and is especially important in the context of any known or theorized companions. NRM polarimetry can also be used to study the polarized structures of massive stars that are shedding their envelopes.[96]

The differential visibility is a primary observable that calibrates instrumental and atmospheric effects. It requires stable images that preserve fine detail produced by the NRM interferogram. Smearing due to vibration or pointing jitter degrades the quality of this observable and the sensitivity for measuring polarized structures close in, as close as ∼50 mas in H band and possibly smaller. For a system at 100pc away this is structure at ∼5 AU.

In May 2015 we took data in relatively poor conditions (bad seeing and wind). Data analysis indicated vibrations that we identified to be in the same direction at previous secondary mirror (M2) 37Hz vibrations. Smearing in the data was also consistent with the direction of vibrations measured on the tip/tilt stage. We present our analysis of the May 2015 polarimetry data alongside AO telemetry taking during that observing run.

We took data again in 2016 after upgrades to the cryocooling system and repair of the M2 mirror. Results and latest performance of GPI's NRM polarimetry mode are presented in §4.3. Here we discuss diagnosis of vibrations in GPI seen through the NRM.

3.6.1 Vibrations in May 2015

The night of commissioning for the NRM on May 6, 2015 had poor seeing throughout the night as well as bad wind at times. In addition we noticed a consistent drop in power for spatial frequencies that corresponded to a particular direction with re-

spect to the telescope, regardless of sky position. This indicated the presence of some off-sky vibrations.

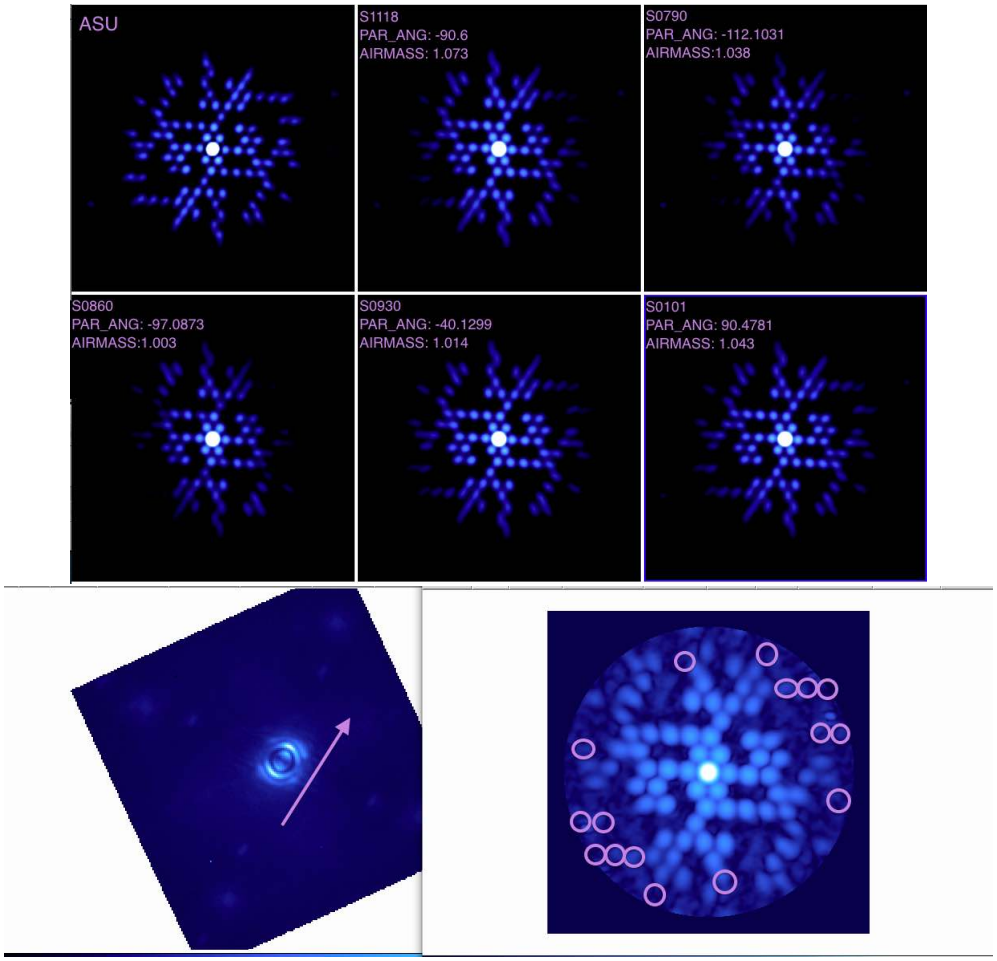

Figure 3.9: Top: Measured visibilities of NRM images from on-sky observations at various positions on the sky. All show varied SW-NE loss indicating vibration along that axis. **Bottom:** coronagraphic spectral datacube slice from January 2015 on the left, with 37Hz vibration, showing the same direction as visibility loss indicated by circled baselines to the right.

Simulating a tip/tilt vibration at the approximate direction of the vibrations seen we can convincingly reproduce the long baseline power loss we see in our data (Figure 3.10). The simulations indicate there may have been up to 20 mas vibration, in the

same direction as the 37 Hz vibrations seen at the beginning of 2015. Therefore a potential source of these vibrations could have been the same source – the M2 mirror.

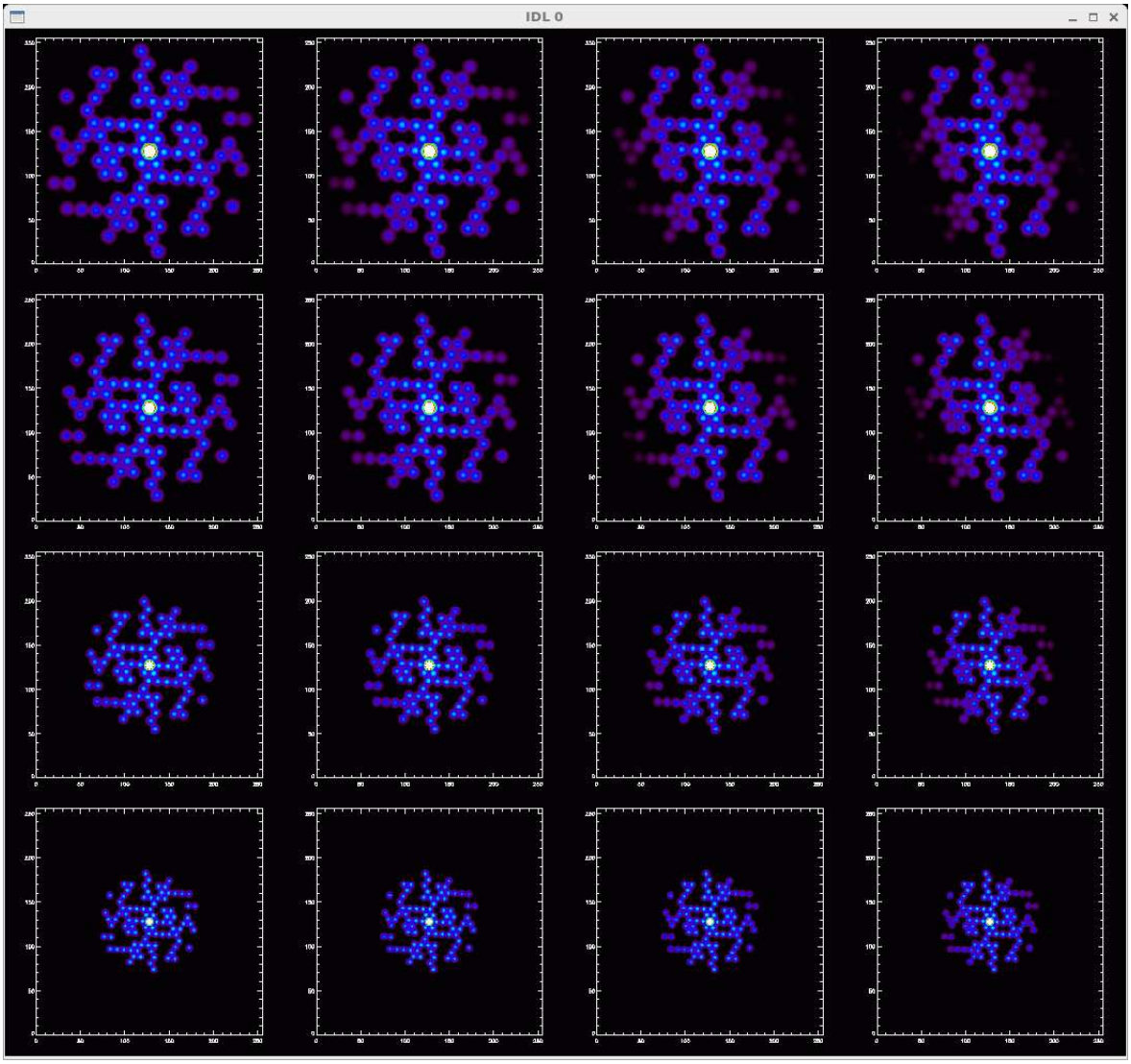

Figure 3.10: ***Left: Power spectra for NRM images with simulated tip/tilt vibrations.*** *Top to bottom: Y,J,H,K filters. Left to right: 5, 10, 15, 20 mas vibration. The simulation indicates that as much as 20 mas vibration could contribute to visibility loss in the NRM images from commissioning.*

We looked at AO telemetry from the night taken at various times during different telescope pointing and conditions. Figure 3.11 shows that the tip/tilt stage showed

generally more tilt than tip, potentially pointing to a vibration direction that is mostly aligned with the y-direction on the WFS coordinate grid. On the right of 3.11 we show the NRM hole positions projected on the WFS. A vibration in the y-direction will wash out fringes made from combinations of holes 0, 1, 5, and 9. This is in fact what we see in the data. The telemetry stage tip/tilt rms and NRM power spectra were consistent.

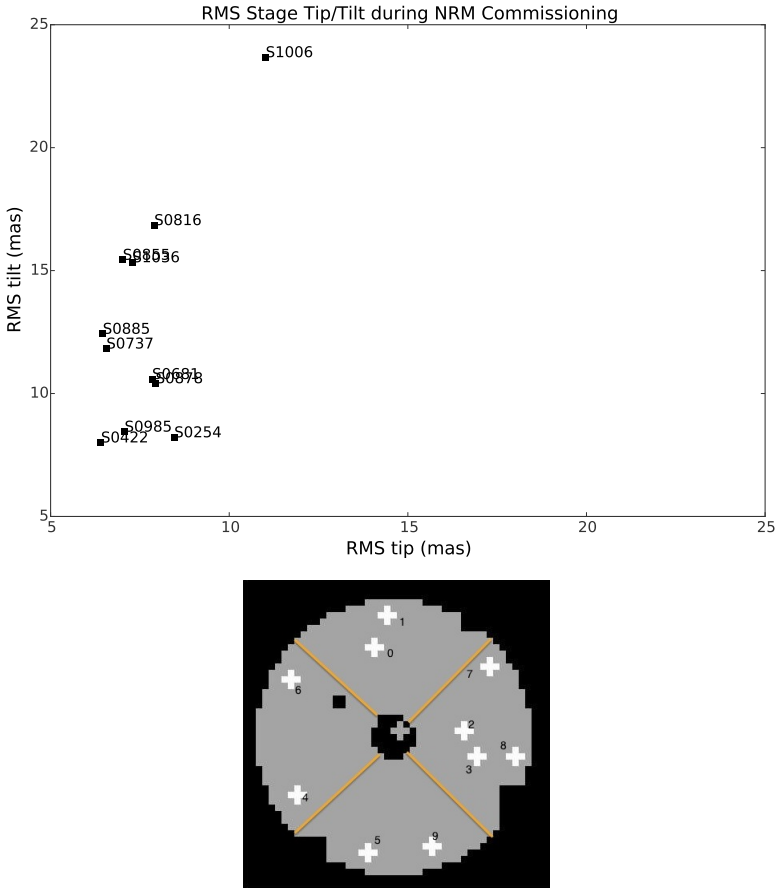

Figure 3.11: ***RMS stage tip/tilt, May 06 2015 observing.*** *Tilt was consistently higher in these datasets. We see that a tilt-dominated vibration (y-direction) will affect the baselines oriented this way, particularly ones formed with combinations of 0, 9, 1, and 5. This is consistent with the baseline power loss observed.*

With this level of vibrations it was not possible to obtain stable, well-behaved differential visibilities. The vibrations were likely made worse by poor on-sky conditions. The cryocooler upgrade significantly improvements to vibrations, but poor weather conditions can still severely effect the data quality.

Chapter 4

GPI NRM: Results and Performance

4.1 Verifying Image Plane Fringe Fitting Software for GPI

The development of image plane-based data reduction detailed in Chapter 2 has led to a nearly complete python software package "nrm_analysis." The package generates community-standard OIFITS interferometry data files and contains a growing set of analysis tools. The most developed is the binary modeling portion designed after Sydney University NRM pipeline. To verify the software performance we tested it on simulated NIRISS data. We chose NIRISS because with only one wavelength

axis all steps of the analysis run much more quickly; the verification is appropriate for multiwavelength data as well.

We model a binary signal in the fringe visibilities with the interferometric result:[97]

$$\nu = \frac{1 + r \exp\left(\Delta u \cdot \alpha + \Delta v \cdot \delta\right)}{1 + r} \tag{4.1}$$

Where r is the contrast ratio (for a faint companion, $r \ll 1$), Δu and Δv are the baselines formed by mask holes (spatial frequencies), and α and δ are the on-sky position of the secondary point source.The closure phase for holes 1, 2, and 3 is defined as $CP_{1,2,3} = Arg(\nu_{1,2} \cdot \nu_{2,3} \cdot \nu_{3,1})$.

For multiwavelength data, as in the case of GPI-spectral mode, contrast can vary across the band. For the purposes of detection we fit a single contrast, separation, and position angle to each full wavelength cube. Once a position and separation are measured, these can be fixed to measure the variation in contrast across the band and extract a spectrum of the companion.

We simulated sets of 22 NIRISS exposures containing 10^6 photons each. Four of these sets are images of a single star and four are images of a binary with properties shown in Table 4.1. With a total of $\sim 10^7$ photons we expect the photon noise limit at a contrast sensitivity around $10^{-2.5}$, which is roughly the 3σ detection limit at separations greater than $\sim \lambda/D$ (Figure 4.1). Other sources of noise in the simulated data include a negligible amount of telescope jitter (an order of magnitude smaller

Contrast Ratio	X position (mas)	Y position (mas)	Spectrum Model
0.16	78	78	A0V

Table 4.1: Simulated binary parameters (on sky). The position angle is automatically flipped in the analysis.

than the diffraction limit) and 0.1% flat field errors.

Detection limits were generated by adding random errors to model closure phases drawn from a Gaussian distribution centered on 0, with error equal to σ^2_{DATA} conservatively scaled by the ratio of the total number of closure phases to the number of independent closure phases. In this case 1000 realizations of noise were simulated at 24 different position angles and the total number of positive detections were counted in order to estimate 5σ detection limit. A detection was counted when $\chi^2_{binary} < \chi^2_{single}$, where

$$\chi^2_{binary} = \sum \frac{(CP_{measured} - CP_{model})^2}{\sigma^2_{CP}}$$

and

$$\chi^2_{single} = \sum \frac{(CP_{measured})^2}{\sigma^2_{CP}}$$

since the null detection should yield zero closure phase. Figure 4.1 displays the parameters of the simulated binary as a red diamond, well within the detection limits and also indicates λ/D and $\lambda/2D$ for the JWST 6.5m primary at $4.3\mu m$.

We can look at a map at χ^2 values over a grid of positions at contrasts that have minimum χ^2 for the binary model. A good indication that there is a companion in the data is a single minimum relative to the whole map, as seen in Figure 4.2. In

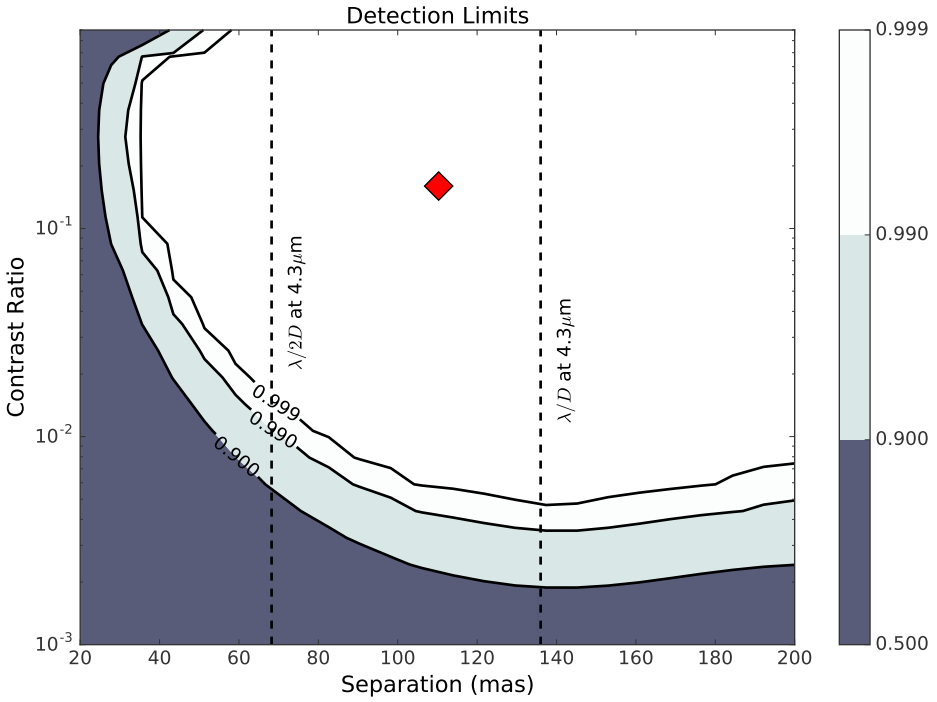

Figure 4.1: The detection limits from a shallow exposure dataset simulated for NIRISS containing small flat field errors. Dashed lines show λ/D and $\lambda/2D$ for the JWST primary mirror at 4.3μm. The red diamond shows our simulated binary position in separation-contrast space, well above the detection limits.

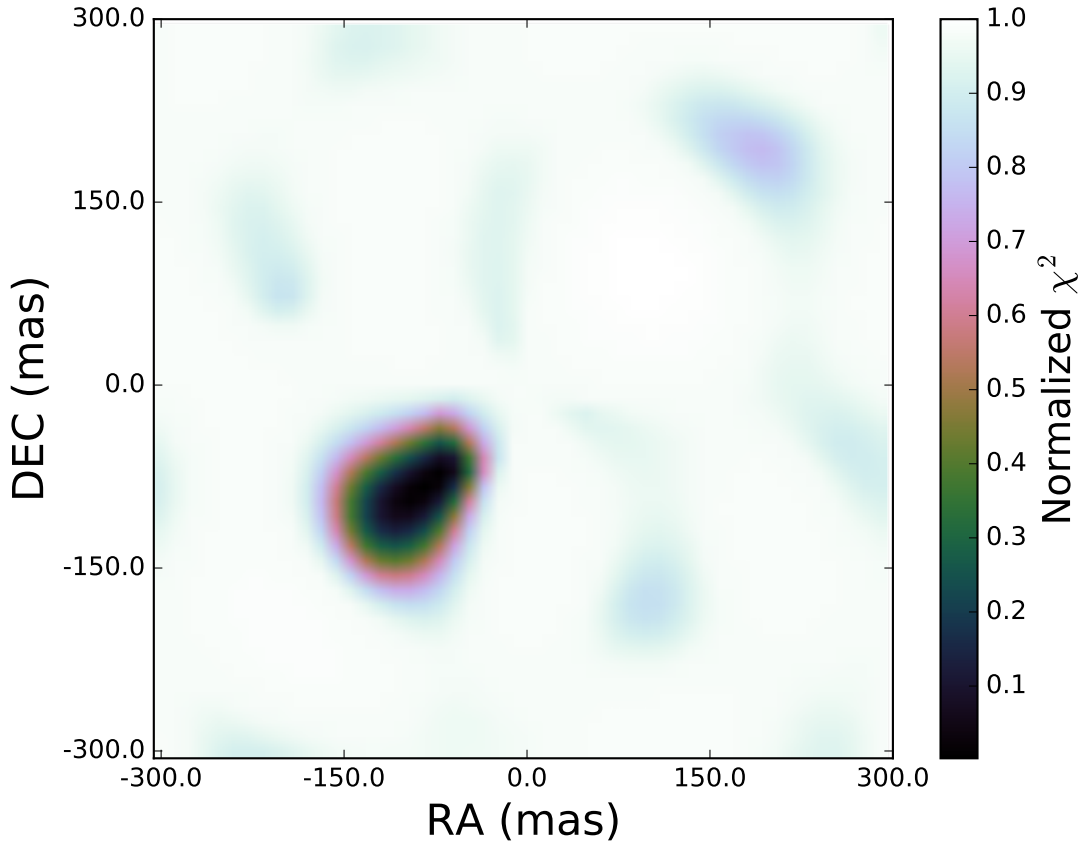

Figure 4.2: χ^2 map of simulated data fit to binary model. The χ^2 is calulated on a grid of positions and range of contrasts. The minimum χ^2 is plotted for each position in the grid. While this is not enough to make a detection, it provides good evidence of the presence of a companion.

this case the strong signal is obvious. This procedure provides a good starting guess for a more sophisticated search to recover the binary parameters. We use the *emcee* package for Markov Chain Monte Carlo analysis.[98,99]

In figure 4.3 we show an example results of fitting our simulated data. We repeated this test with four different simulated datasets and find that we recover the binary parameters within 2σ. Future work for NIRISS will include testing this anal-

ysis method at a range of contrasts and close-in separations where degeneracies can arise. For Gemini Planet Imager spectral mode data the procedure is similar but the data include an extra spectral dimension. For detection, the contrast is assumed constant to locate the best fit position of the companion. After the position is well-determined, a unique contrast can be fit in each wavelength channel. In doing so, we assume that the faint companion position is independent of wavelength. Of course, extended structure frequently exhibits color-dependent morphology, a caveat that must be borne in mind when analyzing real data.

4.2 Spectral mode performance

Both commissioning and queue observations using the NRM on GPI were performed in the semesters between the end of 2013 and 2016. Throughout this time period, both the instrument and telescope facility went through various states of performance. This section will report the binary detection sensitivity of GPI's NRM as of the most recent observations at which point the cryocooling system is upgraded and 37Hz vibrations on the telescope secondary mirror have been fixed. We demonstrate updated performance with data that were taken in May 2016.

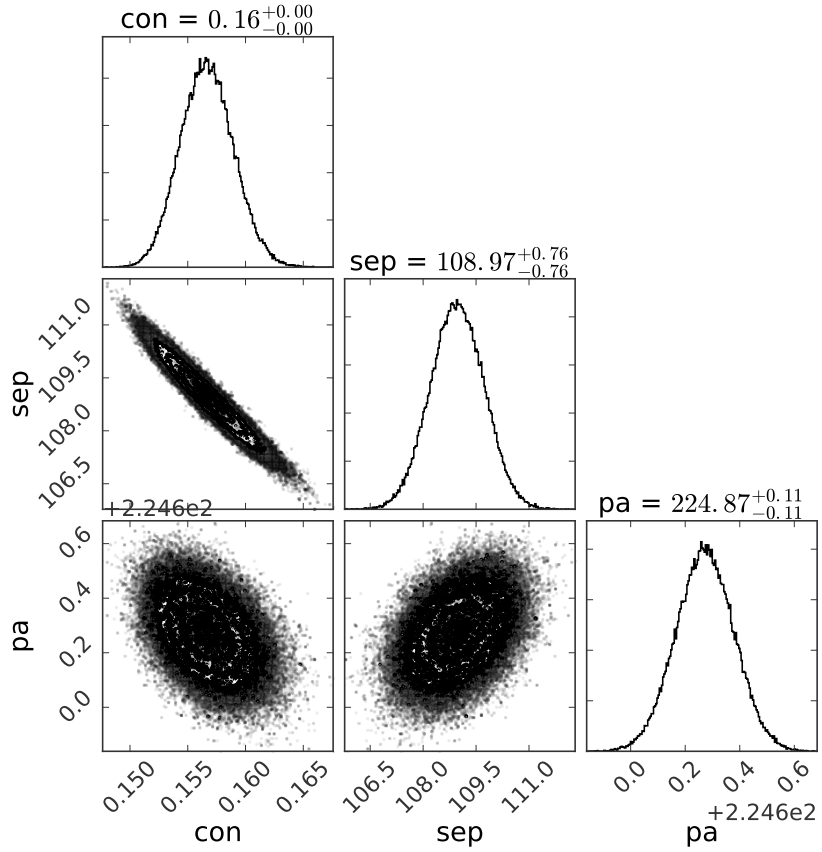

Figure 4.3: An example of MCMC results fitting simulated data with a binary model (using the python package *emcee*[99]). For four different simulations the fits converged well to their solutions and all answers were in agreement within $\sim 2\sigma$.

4.2.1 Detection limits - short exposures

In March and May 2014 we observed the bright single star HD 63852 as a calibration source, with 1.5s exposures (the minimum exposure time). Sky conditions were better during the March observations, so these two datasets give an impression of performance through varied conditions. We expect better performance, in general with short exposures, where the AO system can maintain good correction and vibrations of the instrument have minimal effect. During these two commissioning runs we noticed some pointing jitter, discussed in §3.5, that appeared to be worse with poorer conditions.

We can estimate detection limit in each data by calibrating the first half of the exposures with the second half. We also compare the the detection limits to those of the internal source (as in Figure 3.7). Internal source exposures show fairly deep contrast limits that are difficult to reach on sky where atmospheric conditions limit performance. The March 2014 data demonstrate more reasonable limits in good sky conditions when observing bright stars. In May, we saw reduced performance, expected from higher winds and poorer seeing conditions.

4.2.2 Detection limits - long exposures

Long exposures represent the most likely observing scenario for surveying young moving group stars. In longer exposures vibrations and imperfect AO wavefront

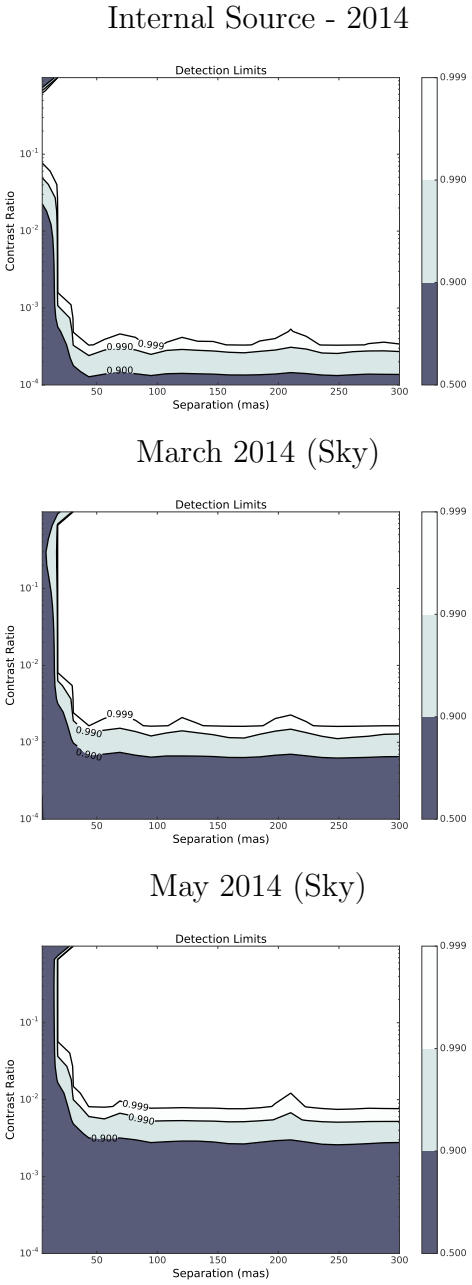

Figure 4.4: Estimating H-band detection limits from 2014A commissioning data (raw phases shown in Figure 3.7). Results from the internal source demonstrate the performance limit since the instrument does not have to mitigate on-sky conditions. Detection limits from March 2014 are more representative of real performance. Poorer conditions in May reflect reduced contrast sensitivity shown in the bottom panel.

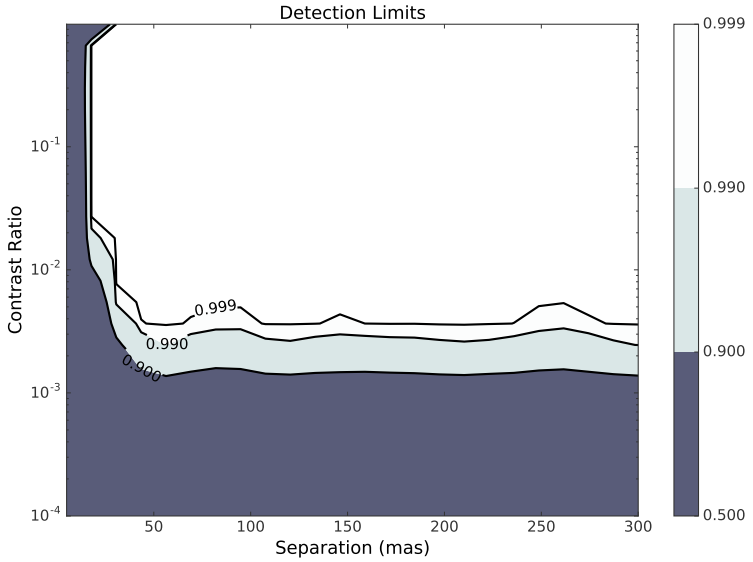

Figure 4.5: K-band detection limits in contrast and separation calculated by calibrating two targets that had non-detections with each other. The limits are slightly worse than those from March 2014 (Figure 4.4, panel 2), expected from longer exposures on fainter sources.

correction will lead to blurring of fringes that degrades performance.

Two stars were observed in May 2016 as a part of the 2016-Q-23 Gemini program (PI: Adam Kraus). We did not detect any secondary sources for these targets, but report upper limits on the existence of companions. The stars in this program present possible targets harboring protoplanetary material due to the young ages. K-band observations should be most sensitive to the thermal infrared emission of low-mass companions around these targets. Upper limits on mass can be estimated from our detection limits based on an appropriate model.

The two stars presented in this work did not show evidence for companions. We calibrated one against the other to measure detection limits. First, as described in

section §4.1 we drew many realizations of binary signal based on our measurement errors and counted the number detected with a hypothesis test. We show a 5σ detection limit of $\sim 4 \times 10^{-3}$ contrast ratio. We note that our two targets were K$\sim$ 5.8, and $\sim$ 8.0, respectively. Contrast limits might have been better if the second target was brighter.

We also show a detection map similar to a common procedure used on Sparse Aperture Masking (SAM) on the VLT,[42,100] setting the detection limit above the point at which χ^2_{binary} becomes equal to or less than $\chi^2_{singlestar} + 25$ where $\chi^2_{singlestar}$ is the null hypothesis. We show our detection map in Figure 4.6. The varying structure across the map is likely due to incomplete sampling of the holes and the uneven structures close in are artifacts. According to BCAH15 models[101] this preliminary result sets a mass upper limit of $\sim 0.06 M_\odot$ for any companions around the one of the stars, and $\sim 0.2 M_\odot$ around the other, assuming ages of $\sim 10 Myr$.[102]

4.3 Polarimetry performance

Polarimetry observations of single stars were taken in May 2016 as part of commissioning after an upgrade to the cryocooler system, which significantly reduced vibrations. Table 4.2 has a summary of the observations.

Conditions were poor on May 03 2016 and exposures were taken on only one source. The AO system reported wavefront errors upwards of 150 nm RMS. Inspect-

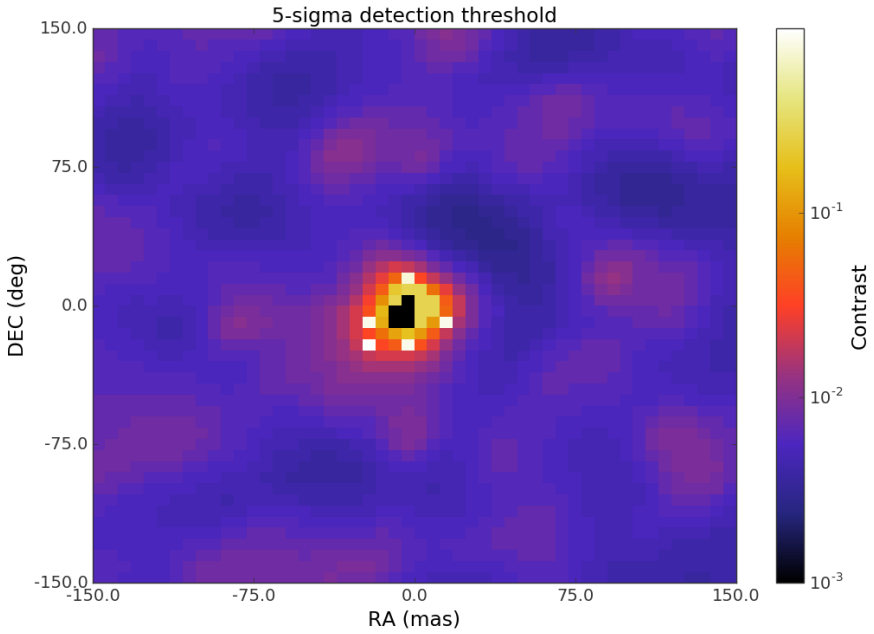

Figure 4.6: A 5σ binary detection map, showing contrast as a function of position. The map is created by setting a limit where $\chi^2_{binary} < \chi^2_{singlestar} + 25$.

Table 4.2: Summary of polarimetry+NRM observations in 2016. All targets are point sources.

Date	Target	Band	Notes
160503	**HR 4860**	H	Switched to J,Y and returned
		J	Poor conditions throughout
		Y	
160504	***nCen**	H - 1.5s	cc80, wfe rms 70 nm (very good)
	***iLup**	H - 1.5s	
		K1 - 4.5s	
	HR 3932	H - 1.5s	cc80, wfe rms 70 nm
	***56Hya**	H - 1.5s	
	HD 142695	H - 8.7s	Conditions worsened,
			visibilities did not calibrate well.

ing visibility amplitudes (in the Fourier Transform), the data do not seem to show the systematic loss of power in the same direction as observed in 2015. A number of exposures did have significant long-baseline power loss in some frames, but in a different orientation than the vibration attributed to the secondary mirror in May 2015. There was not a lot of field rotation for this dataset so it is still uncertain whether the source of these reduced vibilities follows the instrument or something on sky (e.g., wind pattern). However, conditions the following night improved significantly, producing much higher quality data, with strong signal in long baselines.

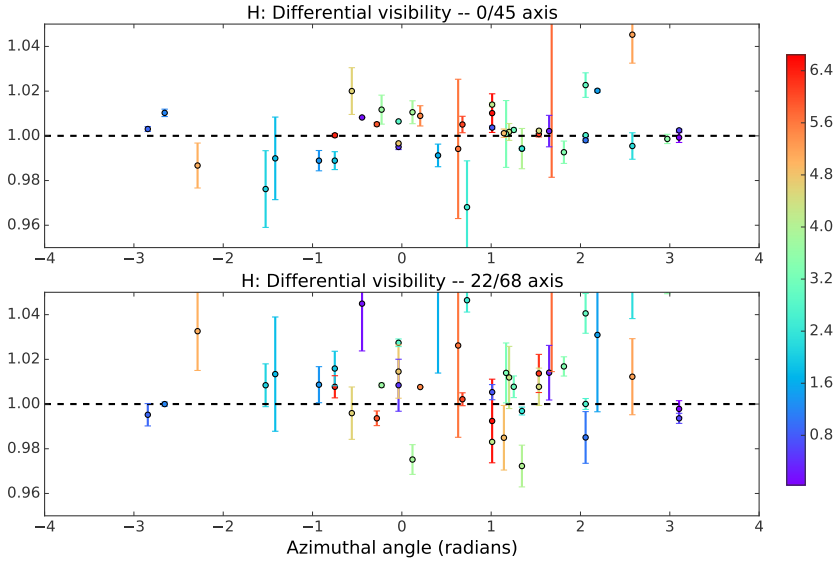

Figure 4.7: Polarimetry performance in 2016 after installation of new active dampers - May 03 (poor conditions). Polarimetry datasets were incomplete due to changing conditions and did not calibrate well. During the various observations header values for RMS wavefront error remained primarily above 150 nm. We display the H-band differential visibilities, which should calibrate to $V^2 = 1$ for a point source.

On May 04 2016 conditions were much better at times throughout the night, with

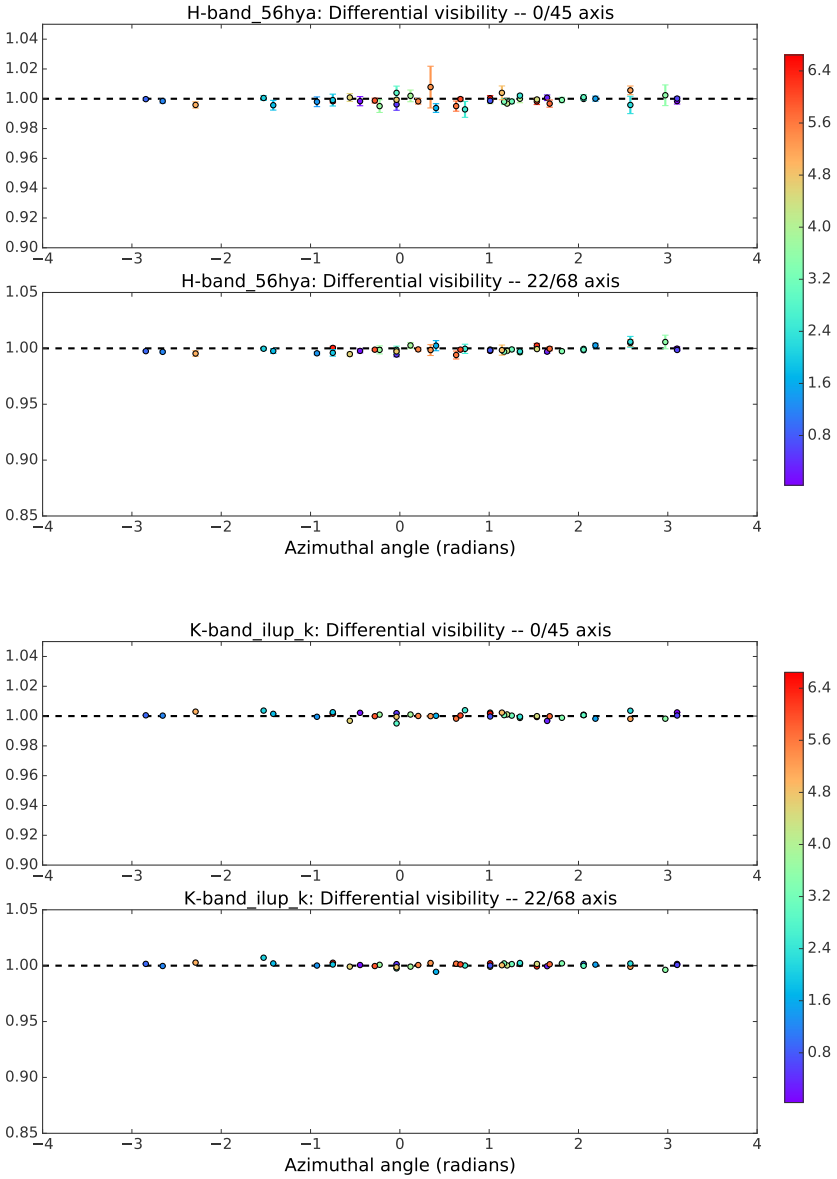

Figure 4.8: Polarimetry performance in 2016 after installation of new active dampers - May 04 (good conditions). Polarimetry datasets from May 04 2016 calibrated very well. During the various observations header values for RMS wavefront error hovered around 100-120 nm. Shown is an example point source calibration source. The theoretical differential visibilities should calibrate to $V^2 = 1$, and the data do to $< 1\%$ precision here.

70 nm rms wavefront error reported. Header values of total wavefront error (keyword RMSERR) were indeed lower for these data, in general around 110 nm. These data do not exhibit the power loss in long baselines. Figure 4.8 shows our calibrated visibilities for two examples, 56Hya in H band, and iLup in K1. The K1 iLup observations had slightly longer exposures (4.5 compared to 1.5s) and show that even with increased exposure time the visibilities calibrated very well, to precision of less than 1%. We were not completely able to test the performance with increased exposure time, as conditions degraded later in the night when we moved to a fainter target. However the results we obtained are very promising and definitely set the stage for exciting science with GPI NRM polarimetry for diffuse polarized source.

4.4 The HD142527 transitional disk system with GPI NRM

Investigating how planets form and dynamically evolve is essential to our understanding of planet populations. Targeting young systems with disks and companions can provide a view of early conditions and the planet formation process. Transitional disks are characterized by a lack of near-IR emission, and often have resolved disk gaps in sub-mm or IR. Disk gaps can be an indication of young planets sculpting out their disks, providing an eye into the planet formation process. The dynamics of accreting bodies inside these gaps is important to understanding how gaps are formed

in young protoplanetary disks.

An obvious system to observe with GPI's NRM was the transitional disk HD142527, a southern target with a known low-mass companion in its $\sim$ 130AU[103] disk gap, too close to the star for coronagraphic imaging. The M dwarf companion at $\sim$ 12AU was first discovered with aperture masking on VLT NACO[104] and later confirmed in Hα direct (non-coronagraphic) imaging on Magellan-AO.[105] The Hα detection indicates that it is accreting material. Despite the companion's presence, its estimated mass is not enough to explain the size of the disk gap. Orbital monitoring of the companion helps constrain the dynamics of the HD142527B in the context of its disk.

4.4.1 "Scaled Up" View of Planet Formation

While HD142527B is not planetary mass, the system can still provide an understanding of planet formation and disk clearing mechanisms. The system represents a likely scaled up view of the planet formation process, with an Herbig Ae/Be primary and M-dwarf secondary.[104–106] The presence of a planet or secondary mass is one proposed explanation for the opening of gaps in protoplanetary disks.[17] In this case one or multiple companions can dynamically clear a region of the disk.[107–110]

Tracking the orbit of HD142527B can help determine whether it has had a role in sculpting out the large gap in the HD142527 disk. Recent observations with ALMA[112,113] put the inner disk at an inclination of 70° relative to the outer disk. The estimated inclination of HD142527B from the astrometry to date[106] is so far

Table 4.3: Published astrometric measurements of HD142527B and their errors[104–106] from NACO's Sparse Aperture Masking (SAM) mode, Magellan direct mode, and GPI's NRM mode. The companion was also observed in polarimetry, but at an offset in position, possibly due to circumsecondary material,[111] so this point was not included in the most recent orbit fit[106] and is not included here.

Instrument	Date	Separation (mas)	Position Angle (°)
NACO SAM	March 11 2012	89.7 ± 2.6	133.1±1.9
	March 17 2013	82.0 ± 2.1	126.3 ± 1.6
MagAO continuum	April 11 2013	86.3 ±1.9	126.6±1.4
NACO SAM	July 14 2013	82.5 ± 1.1	123.8 ±1.2
MagAO Hα	April 2014	79.7 ± 5.6	119.5 ± 8.7
GPI NRM	May 12 2014	77.2 ± 0.6	116.6 ± 0.5

consistent with the inclination of the inner disk.

4.4.2 Plans for Followup

The orbit of HD 142527B remains unconstrained and it will require continuous monitoring to narrow down the orbital parameters. It has moved approximately 13 mas in 2 years. Instruments like GPI and SPHERE[10] both have aperture masking modes that can reach the inner working angles necessary to measure the binary signal from HD142527, and are capable of high precision astrometry. More observations, especially with higher precision will help remove degeneracies in possible orbits for HD142527B

Polarimetry mode observations with the NRM in good conditions will be able to measure a polarization fraction of $\sim$ 1% or better (Figure 4.8) to measure the scattered light properties of the dust in the unseen inner disk, its outer radius, and help confirm its possible relative inclination to the outer disk.[112,113]

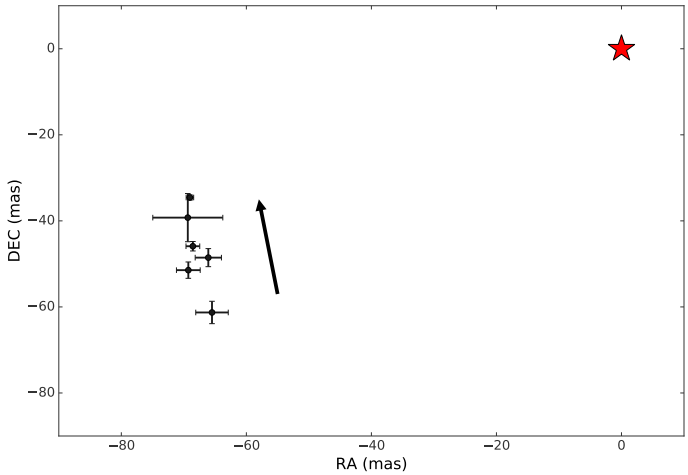

Figure 4.9: The astrometric points listed in Table 4.3 make up a small fraction of the full orbit. Many more years of monitoring are necessary to constrain its orbit.

Chapter 5

Forward modeling coronagraphic PSF subtraction

This chapter covers the development of Karhunen-Loève Image Projection (KLIP) forward modeling (FM) for coronagraphic PSF subtraction. KLIP-FM addresses biases in flux and position measurements of stellar companion. Section 5.1 will cover a very basic background of the KLIP algorithm and the forward modeling approximation that accounts for self- and over-subtraction of the real companion signal. Details of the algorithm are addressed thoroughly in Pueyo (2016).[114] The purpose of this background is to set the context for applying the algorithm in practice. Section 5.2 summarizes the application of KLIP-FM first on simulated signal, and applied to observations of the HR8799 planetary system with GPI in K band (1.9-2.4 μm). The three planets in GPI's field of view (Hr8799c, d, and e) span a range of regimes in

relative brightness and separation and provide a good test case for KLIP-FM. The HR8799e spectrum in K band has not been published by any other study to date. Finally, section 5.3 relates the development of KLIP and KLIP-FM for future non-redundant masking data on space telescopes.

5.1 KLIP Forward Modeling

5.1.1 KLIP background

PSF subtractions aims to assemble an appropriate PSF that captures the speckles in the image to optimally remove the instrument response, leaving only the companion source signal. KLIP uses the covariance matrix of a reference library of images to determine the most common speckle features that arise from instrument and atmospheric aberrations. The following recounts the KLIP procedure described in Soummer et al. (2012).[115] The KLIP algorithm performs the Karhunen-Loève transform on a set of reference images to compute the optimal basis set.

$$Z_k^{KL}(n) = \frac{1}{\sqrt{\Lambda_k}} \sum_{p=1}^{K} c_k(\psi_p) R_p(n) \tag{5.1}$$

This basis set is the product of the mean-subtracted references $R_p(n)$ with the kth eigenvector $c_k(\psi_p)$ of the covariance matrix $\sum_{n=1}^{N_s} R_i(n) R_j(n)$ of n reference images over the region of interest, divided by the kth eigenvalue Λ_k, summed over KL modes.

The estimate of the PSF is made by the projection of KL transform $Z_k^{KL}(n)_{k=1...K_{KLIP}}$ up to a chosen number of modes K_{KLIP} onto the science image. The PSF-subtracted image is then the target image subtracted from the PSF estimate.

5.1.2 Corruption of the companion signal

Several problems can arise in KLIP subtraction because the companion signal is projected onto KLIP modes. In general part of the companion signal can be subtracted, underestimating its flux and modifying its morphology. For precise photometry and spectral characterization this effect will bias the result and must be modeled. Additionally, not all the features of the PSF will be perfectly captured in the subtraction, leaving some residual speckle noise.

In the case of *RDI* (Reference Differential Imaging) where the reference set does not contain any companion signal (when a large reference library can be built[115–117]) is a convenient case to avoid self subtraction of the companion. In this case, corruption of the companion signal arises from over-subtraction – when speckle features overlap the astrophysical signal. Another problem arises when the reference library contains the companion signal. In the case of *ADI* (Angular Differential Imaging) and *SDI* (Spectral Differential Imaging), which take advantage of the movement of speckles through sky rotation and wavelength respectively, the companion signal lies in the reference cube, further biasing the measurement of its true flux. Forward modeling should estimate both *over-subtraction* and *self-subtraction* term that result from the

companion signal in the reference frames.

KLIP-FM approximates the corruption of the companion signal by perturbing the KLIP basis to account for the signal subtraction when the signal exists in the reference library. This is done by propagating the companion signal through the eigenvalue problem of the covariance matrix, yielding perturbed eigenvectors and values.

Over-subtraction is the subtraction of the companion signal due to the presence of speckles in the location of the companion. Over-subtraction is a linear process, given simply by the projection of the companion signal A onto the KL basis over the region of interest in the image, which can be estimated by projecting a model of the signal PSF onto the unperturbed KLIP basis.

$$\sum_{k=1}^{K_{klip}} < A_{model}, Z_k^{KL} > Z_k^{KL}(n)$$

Self-subtraction is the subtraction of the companion signal due to its presence in the reference library. There are two different forms of self subtraction. *Direct* self-subtraction arises from the presence of the signal inside the region of interest where the subtraction is taking place. *Indirect* self-subtraction accounts for the correlations between the companion signal and the speckles. Both terms corrupt the signal recovered from the astrophysical companion. Self subtracted can be estimated by projecting the image onto the perturbed component of the KLIP basis that models

the astrophysical signal's contribution.

5.1.3 Unbiased spectral extraction

This study uses the pyklip[118] software. Tunable parameters in the software include *movement*, K_{KLIP}, for which we vary in some results to demonstrate their effect and the stability of the algorithm. Movement determines how many images to use in the reference library depending on how much the the speckles move relative to the companion in sky rotation and in spectral dispersion. Close-in companions in necessarily require a more aggressive reduction (using more images in the sequence, a smaller movement parameter) since they do not move as far in sky rotation. This puts more companion flux in the reference library and is an appropriate case for KLIP-FM. K_{KLIP} determines how many components of the reference library are used for the assembly of the synthetic PSF. KLIP modes are arranged in descending order of the eigenvalues so that the first component is the strongest representation of the library.

For IFU data the forward model is built at each wavelength and should reproduce the KLIP-subtracted data when multiplied by the correct spectrum. The forward model can be inverted to calculate the source spectrum. We demonstrate the value of including the forward model by recovering spectra for 45 synthetic sources injected into a real IFU dataset. Figure 5.1 demonstrates how the over- and self- subtraction terms recover the lost flux of the companion in this example.

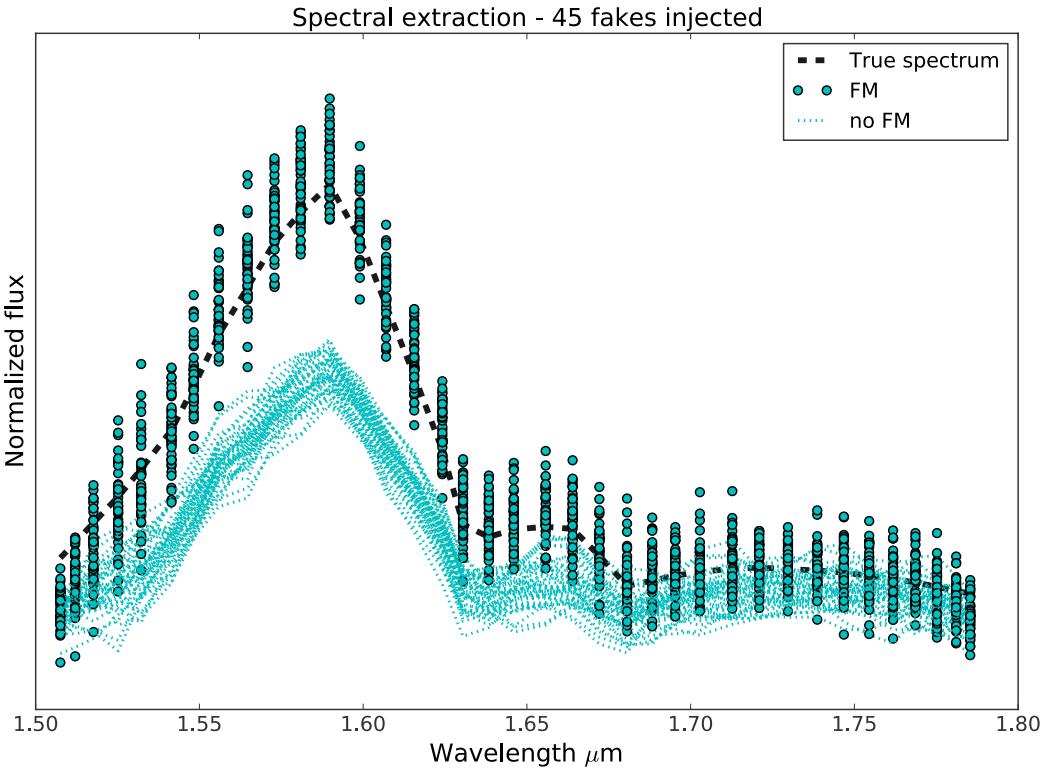

Figure 5.1: We simulate many fake point source signals in an existing dataset and recover the spectrum with and without forward modeling. The large filled circles show that accounting for over- and self-subtraction terms recovers the true spectrum (black dashed line) well, while regular KLIP underestimates the flux, especially at the brightest part of the spectrum.

5.2 Spectral extraction for HR8799 multi-planet system

HR8799 is the only directly imaged multi-planet system, containing four giant planets[119,120] that are an unique laboratory for studying planet properties. Since their discovery, these four planets have become very well studied for dynamical properties,[121–123] atmospheric composition,[124–132] and variability,[133] among other interesting properties. To date, various instruments have obtained spectroscopy in near infrared J, H bands of planets b, c, d, and e,[124,125,134–136] and K band spectroscopy has been obtained for planets b, c, and d.[136–138]

The K band ($\sim 1.9 - 2.5\mu$m) is sensitive to atmospheric composition (e.g., H_2O, CO, CH_4), clouds, and thermal structure. The presence of methane can be a strong indicator of age, but can also be absent due to non-equilibrium processes in the atmosphere. A K band spectrum of planet e, compared to the other 3 planets sheds light on its chemistry and relative composition. Studying the chemistry of all four planets in the same system reveals the variety of planet properties that could be linked to where they formed in the circumstellar disk. The relative compositions of HR8799's planetary companions help constrain evolutionary models and provides information on the mechanism of formation.

5.2.1 Estimating KLIP performance

HR8799 was observed during the verification and commissioning of the Gemini Planet Imager on November 17 and 18, 2013. Spectra of planets HR8799c and d were measured using the TLOCI technique[139] with Angular Differential Imaging only. Planet b was outside the field of view of GPI, and planet e was too close-in to recover a spectrum without bias using this method. The K1 observations on Nov. 17 were at airmass $\sim$ 1.65 and median seeing of $0.''97$. The K2 observations on Nov. 18 were taken at airmass $\sim$ 1.63 and seeing of $0.''75$. Both sets of observations were taken at high airmass and moderate to poor seeing conditions, which reduced image quality. To determine the performance and accuracy of KLIP-FM on this dataset we simulated fake companions at similar separation as planets c, d, and e with the spectra for c and d.[136] We use the spectrum of d at the separation of e.

We simulated 5 fake companions at 5 different position angles and separations corresponding to the positions of planets c, d, and e. We simulated spectra using the shape of published c and d K-band spectra, and assuming an A5V primary. We plan to repeat this with more fake injections after measuring the e spectrum. To extract the spectrum we used a small movement of 2 pixels (meaning that the companion must move 2 pixels relative to the speckles in rotation and spectral dispersion between consecutive reference slices). A small movement is not necessarily appropriate for planets c and d since they are so bright. But due to a limited number of exposures and sky rotation we kept the number small. Future work will include comparing different

choices of movement and K_{KLIP} for all the fake injections. Extending this analysis to more fake injections and further exploring K_{KLIP} and movement parameters will help to both better characterize the KLIP-FM results (i.e. estimate errors appropriately) and properly extract the spectrum of planet e in the real data.

In Figure 5.2 we show the spectral extraction results for the 5 fake companions we injected in the HR8799 K1 dataset. Due to throughput loss at band edges we focus on the middle channels of the band. In general the KLIP-FM extraction is within the published errorbars for c and d spectrum interpolated over the wavelengths in our dataset.

As a preliminary step, we measure the real c and d spectra with KLIP-FM at different values of K_{KLIP} and movement and compare these to recent published spectra for the two planets in K1.[136] We normalize both spectra by their sums to compare the relative shape. Our KLIP-FM spectra look most consistent at small movement and small K_{KLIP}. In general the agreement is much worse in this case than for our injected planets, possibly indicating an inconsistency in assumptions (e.g., of the primary star's spectrum). The fake injection exercise is self consistent since the spectrum is simulated. Future work includes checking that all calibration and normalization steps are accurate. We also plan to extend this work to K2-band data, similarly checking calibration accuracy. The fake injection results are promising for recovering an accurate spectrum of planet e in K1 and K2 bands.

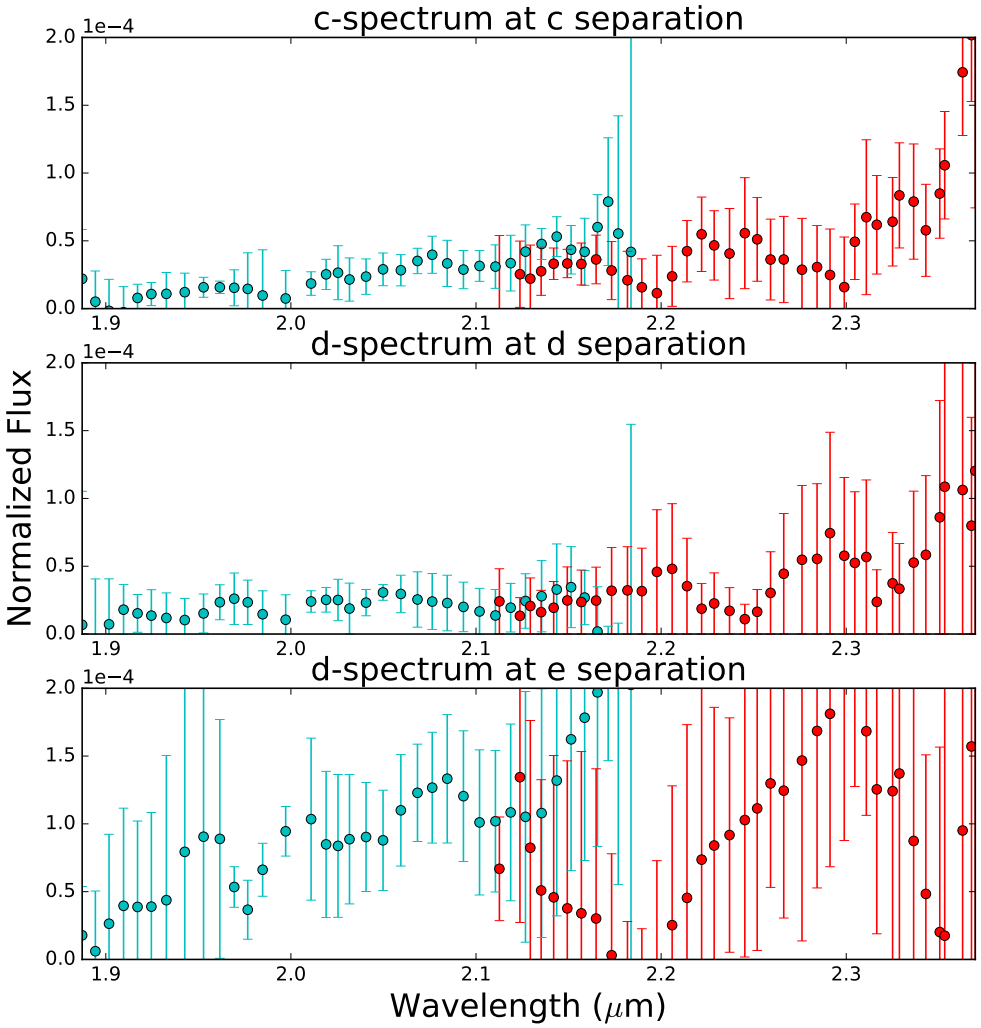

Figure 5.2: 5 fake planets are injected into the K1 and K2 datasets at each of the c,d,e planet separations, with similar spectra, all at the average contrast of planet e from Marois et al. 2010.[120] For planet e we use the spectrum of planet d since its K-band spectrum is not known. We extract the spectra K_{KLIP}=1 and movement of 2 pixels displaying the average flux and its error over the 5 injections. Cyan points represent the K1 band flux at each spectral slice, and red represents those for K2. We demonstrate the accuracy of the KLIP forward model to recover a spectrum consistently in this proof of concept. Planets c and d are recovered with relatively small error, especially in K1 away from band edges, while planet e closer in has larger error. We expect improved results, especially close in, with observations in better conditions.

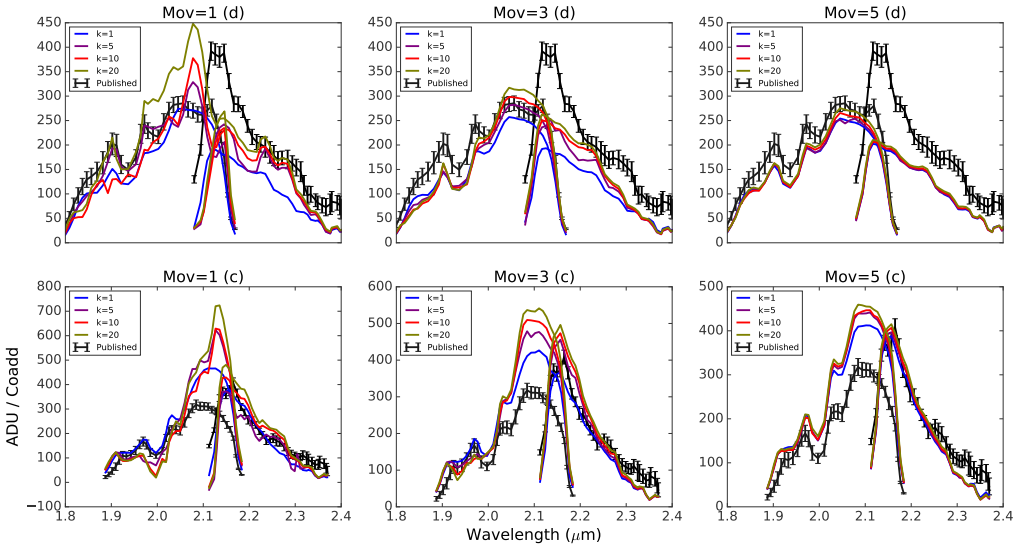

Figure 5.3: We explore a range of KLIP parameters, K_{KLIP} and movement, to test spectral extraction on HR8977 planets c and d in normalized contrast to compare the shape of our spectra to published ones.[136] We can see significant decrease in flux at band edges, a result of low throughput and focus on the center of the spectrum. The KLIP extraction seems to performs better at small movement, and in general small K_{KLIP}, though for the most part results are similar with similar K_{KLIP} values.

5.3 Applying KLIP to inteferometric analysis

We can draw many parallels between NRM data analysis and coronagraph PSF subtraction. It can be particularly difficult to define the errors in NRM detection, when correlations between observations and systematic errors are not well understood. Challenges and advances in PSF subtraction in signal to noise estimation and flux conservation can inform procedure in NRM data reduction. Both PSF subtraction and NRM calibration attempt to subtract the instrumental response from the observable. In the case of images, this is signal in the pixels. In the case of NRM, this is signal in the visibility, for example the closure phase. One can construct a similar KLIP procedure for interferometric phases. Ireland (2013)[58] describes a method to measure statistically independent phases.

This formalism will be particularly important for masking on NIRISS. NIRISS-AMI will be able to build up a sufficient library of reference stars. On a stable spacecraft, single stars from all regions of the sky are expected to be appropriate calibration sources, compared with ground-based practice of choosing a calibrator in or near the same region of the sky. As in the RDI case in coronagraphic subtraction, there is no companion signal in the reference library and forward modeling is straightforward.

Applying the forward modeling procedures described in this chapter towards NRM

data is less straightforward. ADI and SDI PSF subtraction take into account the predictable way the speckles move with respect to the astrophysical signal in sky rotation and wavelength dispersion. In the ADI case one might be able to construct reference phases from rotations (or "rolls") of the telescope on a single target. In the SDI case, phase errors are not all expected to change with wavelength, but the spectrum of the source is. Methods from optical long baseline interferometry such as differential phase[140,141] could benefit ground-based IFUs.

In general forward modeling will be very important for NIRISS-AMI observations. With the stability of space observations NIRISS-AMI will observe both multiple-point sources as well as more complicated structures,[60,73] including resolved solar system bodies[142] and the fueling structures of AGN,[66] which require both model-based and blind image reconstruction.

Chapter 6

Wavefront sensing with a non-redundant mask

6.1 Measuring low-order wavefront errors with GPI's NRM

Due to its geometry the non-redundant mask on GPI is sensitive to low frequency wavefront errors. Phase delays between mask holes (fringe phases) provide information about the wavefront at the focal plane, including non-common path errors relative to the wavefront sensor. In particular focus (e.g. Fig 6.1) and astigmatism produce fringe phase shifts between mask holes. These are very obvious in the data, resulting in noticeable PSF asymmetries.

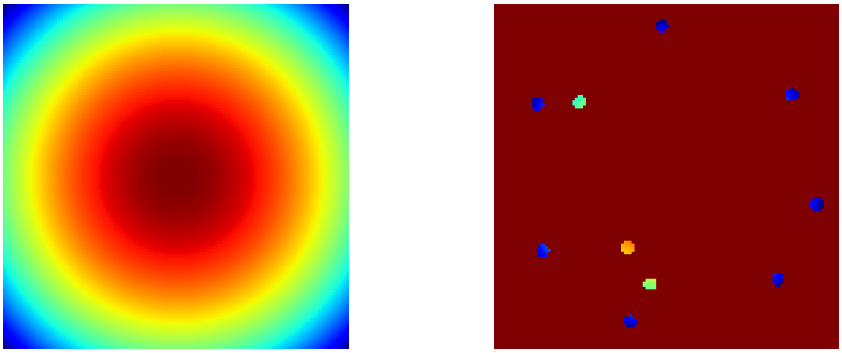

Figure 6.1: Left: focus aberration in the pupil. Right: Focus seen through GPI's 10-hole NRM, producing obvious fringe phase shifts in baselines associate with the inner 3 holes.

6.1.1 Fitting NRM data to low order aberrations

Information from NRM images made with GPI's internal source can be used to fit low order Zernike functions to the data. The following procedure details one approach:

- Remove global tilt from our fringe phase data.
- Simulate fringe phases for a set of low order Zernike modes (e.g. up to coma)
- Fit the appropriate amounts of each zernike to measured fringe phases

The dominant mode we recover is focus. To convert to nm we rely on the wavelength reported the GPI pipeline, which may not be a perfect match, and the knowledge of the plate scale. Uncertainty in these quantities produce errors in the measured wavefront error.

The first set of observations were taken on May 6, 2015 in various conditions on sky.

Changing conditions may account for additional variation in our results. The figure below displays measurements taken on two sets of data, 10 exposures in H band and K2 each. The median wavefront error in each Zernike mode was determined rejecting the band edges, which have low throughput. The K2 data showed lower contributions but much higher residuals.

This method provides an approximate approach to measuring the wavefront at the focal plane. Certain Zernike modes can mimic others over the NRM pupil (like coma and tip/tilt). Concentrating on focus and astigmatism produced the most consistent results.

6.1.2 Measuring and correcting GPI's focus

In 2016 we took several sets of exposures using GPI's NRM with the internal source to measure focus errors at the detector. Using the procedure described in the previous section we fit NRM fringe phases to a set of low order Zernike functions and report the measured focus error. We took exposures across GPI's Y,J,H, and K1 bandpasses (with the exception of K2 due to low throughput and high background). We found the data consistently pointed to a focus offset of 145nm, within measurement error. The data are summarized in Figure 6.2

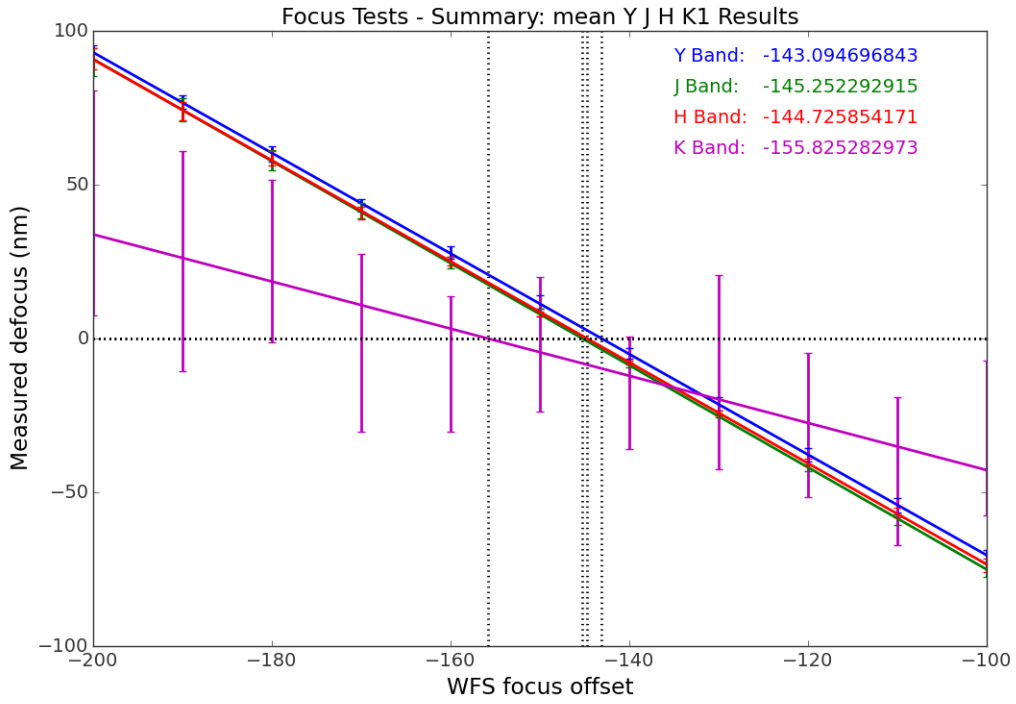

Figure 6.2: Results from focus measurements using GPI's non-redundant mask through GPI's Y, J, H, and K1 filters. Small differences between bands could represent uncertainty in either the wavelength solution or the plate scale.

6.2 Phase retrieval using an NRM

NRM images can be paired with full pupil images to recover the full wavefront with the Gerchberg Saxton (GS) algorithm. This section presents work published in OSA Journal Optics Express in June 2016.[143]

6.2.1 Gerchberg-Saxton Phase Retrieval

Intensity data from far-field or in-focus imagery of a point source is often used to determine the aberration in an optical system. Sometimes the aberration is an engineering or calibration quantity, as in the case of the immediately post-launch *Hubble Space Telescope* (HST), and sometimes it is interesting of itself, as occurs in lensless X-ray microscopy. The Gerchberg-Saxton (GS) algorithm[144] iteratively accomplishes an estimation of phase from image intensity and a knowledge of the pupil geometry, and does typically converge, but it can seem to converge to a spurious solution that is a local minimum, or converge to either of the two ambiguous solutions that are global minima. The unconstrained GS algorithm can converge to either the true pupil field $P(x)$ or its complex conjugate whose argument's sign is reversed, $P^*(-x)$.[145] Breaking the two-fold ambiguity can be accomplished in different ways. A consideration of more data taken with added defocus (or other kinds of phase diversity) can result in obtaining the true aberration.[146,147] Extra data in the form of pupil diversity can also be used to break the sign ambiguity of the phase. Our

approach is included amongst the latter class of methods.

The GS phase retrieval method iteratively applies the known pupil transmission constraint in the pupil domain and the measured image intensity constraint in the image domain.[148] Stepping from one domain to the other is accomplished by a Fourier transform of pupil plane or image plane complex amplitudes. In the special case where the aberration is *only* composed of functions where $P(x) = P^*(-x)$ (such as purely tip/tilt or coma) the phase can be recovered unambiguously with the unconstrained GS algorithm In practice the algorithm can converge to a local minimum rather than the true pupil phase unless the initial guess at the pupil phase is in some heuristic sense fairly close to the correct value.

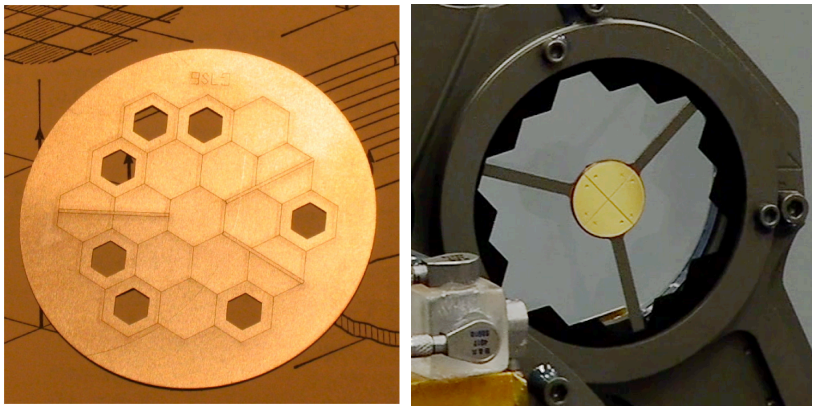

Figure 6.3: JWST NIRISS pupil optics NRM and CLEARP. A life-sized prototype of the NRM is shown on the left, and the flight mask CLEARP in the NIRISS Pupil Wheel on the right. The JWST primary mirror is reimaged to a 40 mm diameter pupil in the plane of the NIRISS Pupil Wheel. The high quality of the image of the primary in NIRISS's entrance pupil,[149] makes NIRISS well-suited for our wavefront sensing technique during both commissioning and routine science operations.

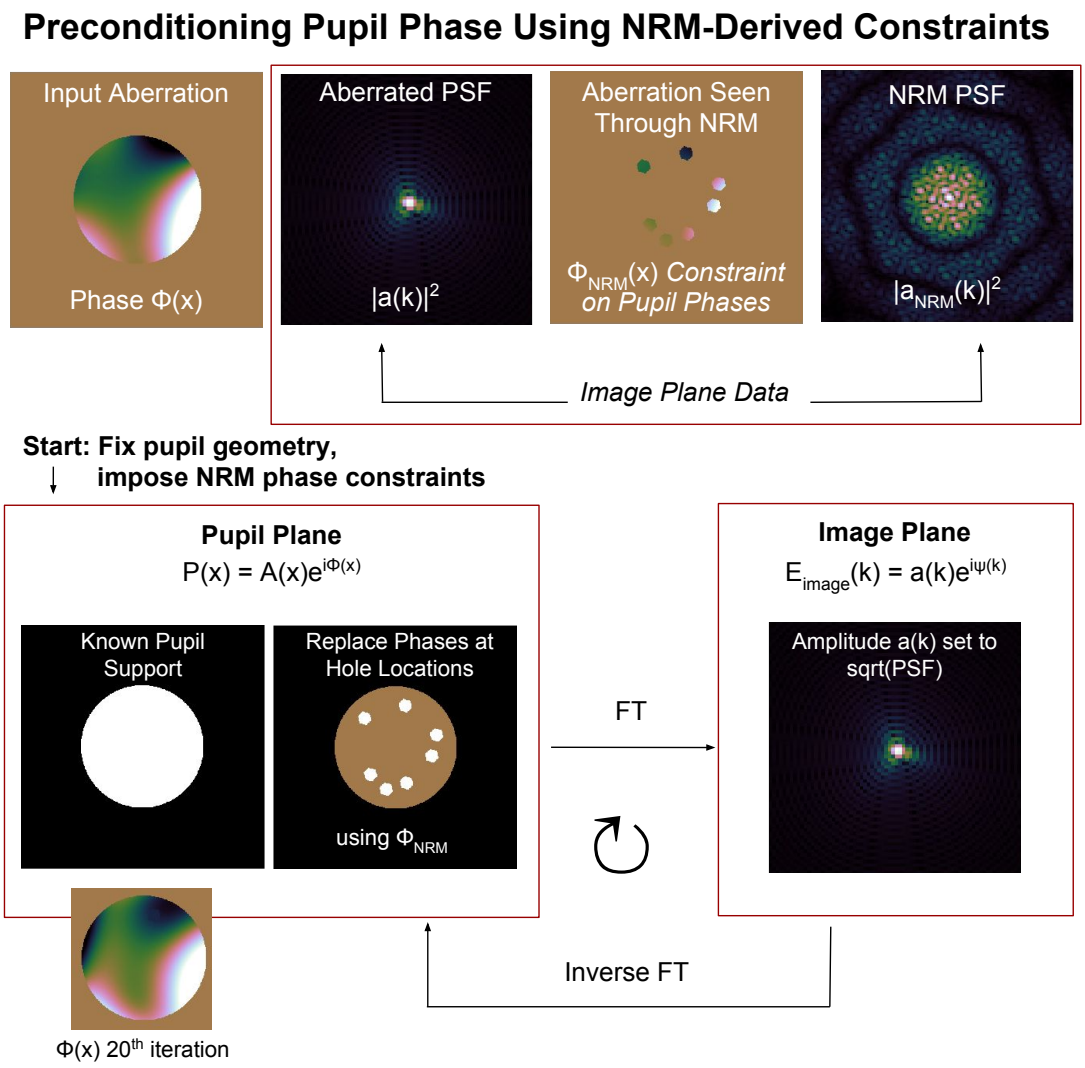

Figure 6.4: An example of true phase aberration, the quantity we are trying to measure, is shown at the top left. Exposures with the full pupil and the NRM produce aberrated PSFs. The NRM PSF is used to estimate the phases over each hole. We assume a known, fixed, pupil support $A(x)$, enforcing the pupil amplitude to match the known geometry of the pupil in each iteration. In addition, we also replace phases in the region shown with the average phase measured over each hole $\phi_{NRM}(x)$, measured from NRM fringe phases (bottom left two panels). We propagate between pupil and image planes since $P(x) \rightleftharpoons E_{\text{image}}(k)$. In each iteration we replace the image field amplitude $a(k)$ at the focus by the square root of the PSF intensity (bottom right). We show an example of the estimated pupil phase at the 20th iteration. In this study we remove the NRM constraint after a fixed number of iterations (typically 100).

6.2.2 Practical Motivations for in-focus phase retrieval

This section describe a phase retrieval method that uses a pair of in-focus images, one taken with the full pupil and the other with a non-redundant mask (NRM) in the pupil. A NRM consists of a set of holes in a mask where no hole-to-hole vector is repeated (e.g., Fig. 6.3 (left)). Our approach can be backup method for fine wavefront sensing that may typically be required in order to maintain diffraction-limited 2 μm image quality on the 6.5 m 18-segment infrared James Webb Space Telescope (JWST), especially during routine operation and later stages of commissioning. A flight-ready wavefront sensing scheme using JWST's *Near Infrared Camera* (NIRCam) has already been developed and tested.[150] However, JWSTs Near Infrared Imager and Slitless Spectrograph (NIRISS)[53] using its two pupil masks, NRM and CLEARP[151] (see Fig. 1) can serve as a backup sensing method. We show that these two pupil masks can be used to measure the telescopes aberrations without introducing focus diversity by sweeping the secondary mirror through focus or placing some of NIRCam's three weak lenses in the beam.

Our backup method reduces mission risk since it provides a second instrument that can measure JWST's wavefront. Using both NIRCam and NIRISS also provide wavefront measurements at different field points, which could assist with secondary mirror alignment when commissioning JWST. During routine astronomical observa-

tions a pair of images taken with the CLEARP and NRM pupil masks in one filter can provide a full wavefront measurement to interferometric accuracy. Such measurements could also support image deconvolution methods at all wavelengths in NIRISS, where all powered imaging optics are reflective. Using in-focus imagery and hardware optimized for science removes the need for dedicated wavefront sensing hardware, such as weak defocusing lenses, on future space telescopes. Our approach does not solve the persistent problem of non-common path wavefront aberrations in coronagraphs between the wavefront sensor and the focal plane mask,[152] because we measure the wavefront at the science detector (rather than at the focal plane containing the coronagraphic occulter).

This study quantifies the method's performance when faced with realistic limits of noise, size of the image (number of resolution elements), and wavefront error expected during certain commissioning phases of JWST. §6.2.3 motivates our approach and the design choices of our study. §6.2.4-6.2.5 show examples of how the algorithm performs under different conditions using both monochromatic and 8% bandwidth images, matching NIRISS's F480M filter on a continuous circular pupil. In §6.2.6 we apply the algorithm to a JWST-like pupil with segment tip, tilt and focus aberrations, as well as global pupil aberrations. We discuss our results in §6.2.7 in the context of JWST mirror phasing.

6.2.3 Methods

We presume that disjoint segments of the pupil have already been brought to a common pointing, and to near a common focus. This places an upper bound on the sizes of piston and tilt differences over the pupil (given the optical quality of each segment). In addition, we assume that every segment in the pupil is well within the coherence length of the filter bandpass, so that the PSF is somewhat coherent. Reaching this coarsely-phased stage is possible using JWST's NIRCam[150,153,154] or, as an alternative, with NIRISS and possibly MIRI.[153,154] After the 18 segments of JWST's primary mirror are coarsely phased we do not expect any phase wrapping if we only use NIRISS' 4.3 μm or 4.8 μm wavelength filters. Our study focuses on the problem of measuring a wavefront aberration that does not exhibit phase wrapping, in order to explore algorithmic efficacy rather than address technical complications.

The GS algorithm iterates between pupil plane field $P(x)$ and image plane field $E_{\text{image}}(k)$, applying constraints in each domain before returning to the other (by means of a Fourier Transform, for example). For our image plane constraint we replace the image plane amplitude by the square-root of the image intensity. We constrain the pupil plane amplitude by forcing it to be the pupil support function. We modify initial iterations of the GS algorithm by applying additional constraints in the pupil plane over the regions of the holes in the NRM.

By analyzing a PSF taken through an N hole NRM we obtain $N(N-1)/2$ *fringe phases*. Physically, a fringe phase is the piston component of the optical path delay

(OPD) between two holes in the NRM. We use these fringe phases to calculate the piston over each hole in the NRM. This can be done uniquely by making the N pistons possess a zero mean.

We initialize the pupil phase over the mask holes to the NRM PSF-derived OPDs and assert zero phase in the pupil everywhere else. In each subsequent constrained iteration the pupil phase over the mask holes is replaced with the NRM-measured phase piston. Elsewhere in the pupil we use the phase provided by the GS iteration without interpolation. We then smooth the entire pupil phase by representing it with a small set of low-order polynomials.

This starts the GS iterations off closer to the true phase, which we show enables robust and rapid phase retrieval without the need for defocused images. Our pupil phase estimate approaches the true pupil phase in a just a few iterations, even when we applied 5% errors to measured piston phases.

During the initial constrained GS iterations the phase over the remainder of the pupil can drift towards a solution while maintaining agreement with the NRM image data in selected areas. The basic process is outlined in Fig. 6.4. After this initial rapid convergence, the NRM-measured pupil phase constraints are lifted, and the unconstrained GS method converges to the true phase in most of the cases we tested. Pathological cases where NRM-derived constraints do not contain any information on the pupil phase can be constructed (e.g., pure segment tilt with zero hole piston).

We chose to constrain the pupil phase by applying the average hole piston over

the entirety of the mask hole locations rather than over smaller areas (or just a few points) in the pupil. If the region of replacement is too small it can add artificial high frequency signal in the reconstructed pupil. In general, unphysical high frequency (frequencies beyond the limit of the number of resolution elements in the image) phase will build up during this process, without smoothing. We smooth the pupil phase each iteration by representing it with the first 15 Zernike[155] or Hexike polynomials,[156] depending on the shape of the pupil. Choosing an optimal set of basis functions that are better suited to the actual segment geometry (including obstructions) is beyond the scope of this study. For this study we add 5% error to zero mean pupil phases (radians) that would be measured from the NRM image in order to introduce some measurement error.

We used 250 pixels across our circular pupils, and up to 1024 pixels for complicated obstructed apertures. We have assumed the OPD over each segment (or the full circular pupil) only contains low spatial frequencies (compared to the Nyquist frequency of our pupil sampling), so we can represent the pupil phase over a segment with a few low order polynomials.

6.2.4 Monochromatic Circular Pupil

In this section we apply our constrained GS phase retrieval algorithm to a simple circular pupil to demonstrate the principle. Using a known input wavefront, constructed with a random realization of the first 10 Zernike polynomials, we simulate

images at the NIRISS pixel scale of 64 mas using a 6.5m diameter pupil at 4.8μm to match JWST-NIRISS's F480M filter. NIRISS is Nyquist sampled at $\sim$4μm. Our images are slightly finer than Nyquist sampled. The technical complications of sub-Nyquist image sampling may be addressable using existing techniques.[157] Our goal is to measure this input wavefront. We apply our NRM phase constraint for the first 100 iterations and then remove the constraint, allowing the algorithm to run until it converges to a state where the solution is stable between consecutive iterations. We report two relevant quantities, the *true error* and the *convergence*. The *true error* is the difference between the actual zero-mean wavefront and the pupil phase estimate. We use the true error to evaluate the algorithm performance in this study. The *convergence* is the difference between pupil phase in consecutive iterations. The convergence criterion sets the stopping point of our iterations. We set our numerical convergence criterion to 10^{-6} radians difference between iteration i and $i-1$. We chose this criterion to be smaller than the expected true error. In a practical situation, the size of the true error will have to be estimated beforehand with simulations, such as ours, and optical testing.

We damp each iteration, computing the pupil phase as 80% of the new solution and 20% of the solution from the previous iteration. We did not optimize the damping in this study. Finally we smooth our estimated pupil phase by representing it with the first 15 Zernike polynomials when using a circular pupil. In the case of hexagonal mirror segments we use equivalent 15 Hexike polynomials on each segment. The

difference between iterations that decides the convergence condition is calculated inside a slightly undersized pupil to avoid any edge effects.

6.2.4.1 Concept: Phase Retrieval With and Without Constrained GS (Noiseless Case)

We demonstrate the advantage of our constrained approach compared to pure GS phase retrieval using a noiseless image made from an unobstructed circular pupil. Figure 6.5 compares the constrained case (using NRM fringe phases) with the unconstrained Gerchberg-Saxton algorithm. The initial pupil has 0.62 radians rms of phase ($\sim$ 460 nm). We convert angular measure to a physical distance assuming a wavelength of 4.8 μm, the central wavelength of the JWST filter we model. Figure 6.6 displays the true error and convergence for both the constrained and unconstrained cases. We refer to the true error as *residual wavefront* henceforth. In the unconstrained case the algorithm converges quickly (Fig. 6.6 blue solid line) but to the wrong solution – the true error increases over time (blue dotted line). The residual wavefront in this unconstrained case is 0.53 radians ($\sim$400 nm) rms phase, as seen in the rightmost panel of Fig. 6.5. In the constrained case the residual wavefront error falls quickly in just a few iterations. The final residual wavefront using the constrained GS algorithm has 0.1 radians ($\sim$76 nm) (middle panel of Fig. 6.5).

In some cases, after steadily decreasing, the true error between the measured wavefront and the true aberration, increases a small amount when the constraint is

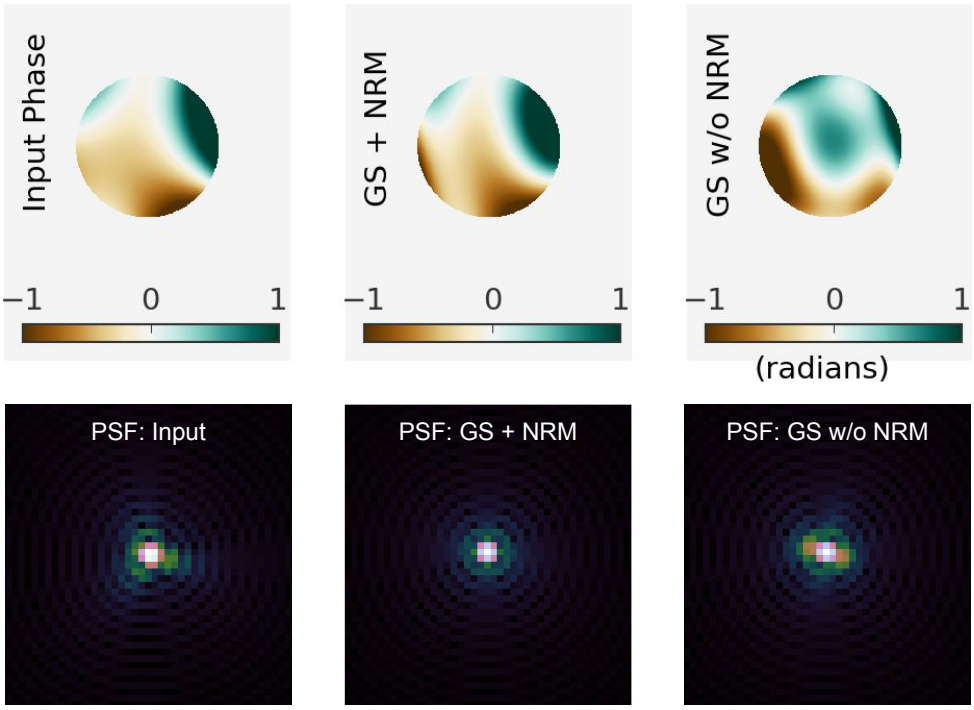

Figure 6.5: Top: Noiseless monochromatic phase retrieval of input aberration on the leftmost panel with 0.62 radians rms wavefront error. We display the phase retrieval with NRM constraint (middle panel) and with out (rightmost panel). With perfect correction the constrained phase retrieval can sense the wavefront to residual of 0.10 radians rms phase, while the unconstrained approach produces a residual of 0.53 radians rms phase. At $\lambda = 4.8\mu$m, 0.1 radians corresponds to $\sim$76 nm of phase. **Bottom**: PSFs corresponding the initial PSF in the leftmost panel and the residual wavefronts in the middle and rightmost panels

lifted and the algorithm is allowed to "relax," as shown in the black dotted line in Fig. 6.6. The performance details are most likely due to our specific choices of damping and smoothing and we anticipate that improvements can be made in the practical implementation of this approach. For the remaining sections of this study we focus on the major limiting factors that will guide the observations necessary to measure the wavefront from in-focus images.

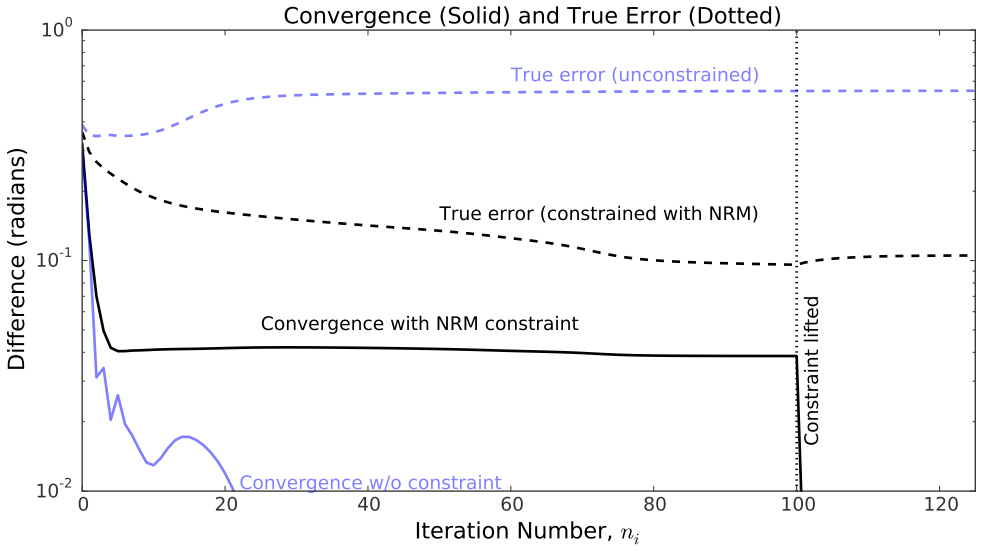

Figure 6.6: Algorithm *convergence*, the difference between pupil phase at n_i and n_{i-1} iterations, is shown in the solid curves. The *true error*, the difference between the true aberration and the measured phase, is shown in the dashed curves. These reflect the trials shown in Fig. 6.5. We remove the constraint after 100 iterations (vertical dotted line) and allow the algorithm to converge. Applying the NRM constraint resolves the GS degeneracy and allows the algorithm to converge in the correct solution. In the unconstrained case the algorithm converges quickly to the wrong solution.

6.2.4.2 Image Size Dependence

The reconstruction performance is ultimately limited by the size of the image used (in units of the resolution element λ/D). Roughly speaking, by limiting the measured spatial frequencies in the pupil, the image size governs how well we can correct the wavefront. This image size dependence applies only to the full pupil image, as the NRM image contributes only a guiding first estimate. In Fig. 6.7 we compare the residual error in the measured wavefront with the number of resolution elements in the PSF. We find that image sizes of $\sim 25\lambda/D$ can be used to correct the wavefront with acceptably small residual wavefront error. For the remaining simulations in Sections 6.2.4 and 6.2.5 we used an image size of 128 pixels, which corresponds to $\sim 50\lambda/D$. Deep coadded exposures are likely to be needed for the required dynamic range. In many of the following cases the image size sets the floor for our wavefront sensing accuracy.

As described in Perrin et al. (2003),[158] the direct correspondence between radial distance from the center of the PSF and the spatial frequency in the pupil plane is only true for Strehl ratios above about 90%, where the 1st order expansion of the PSF is a good representation. But for lower Strehl ratios the correspondence is only an approximation. Higher order PSF expansion terms show cause frequency mixing, so phase terms with a spatial frequency of eg. M cycles across the pupil can place speckles at harmonics located at $2M$, $3M$, ... resolution elements from the core. Since we use images with Strehl ratios below 90%, we find image size limits our

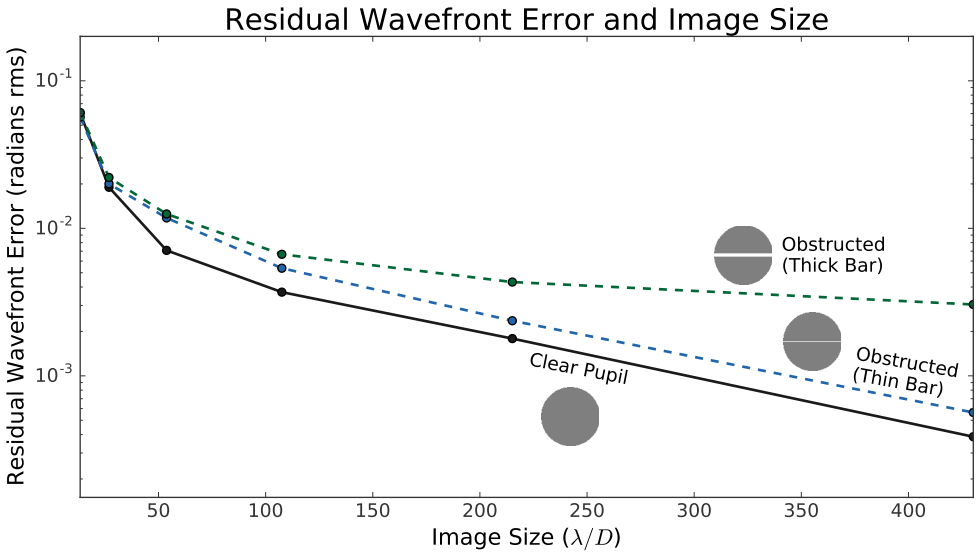

Figure 6.7: We compare reconstruction error with image size (number of resolution elements in the image). Pupil obstructions introduce more error with increasing obstruction size.

wavefront sensing precision.

In the presence of pupil obstructions (a single spider in Fig. 6.7) we still find acceptable, albeit slightly reduced performance; our accuracy improves with increasing image size. The larger obstruction limits the reconstruction accuracy most. We suspect that a different approach to smoothing each iteration may improve this performance. To mitigate the effects of pupil obstructions, in Section 6.2.6, where we simulate JWST-like segment gaps and spiders, we use larger image size of 524 pixels, approximately 70 λ/D.

6.2.4.3 Capture Range

In the noiseless case (using a $50\lambda/D$ image size) we can recover the wavefront with a standard deviation $\sigma = 10^{-2}$ radians residual error between the true aberration and the estimated wavefront from our algorithm. Our input aberrations do not exceed 2π radians P-V wavefront error because we do not implement any phase unwrapping in this study. Figure 6.8 displays the residual between the reconstructed wavefront and the true aberration as a function of P-V wavefront error of the true aberration, indicating the region above 2π radians where phase wrapping occurs. Incorporating phase unwrapping procedures may improve performance in this region.

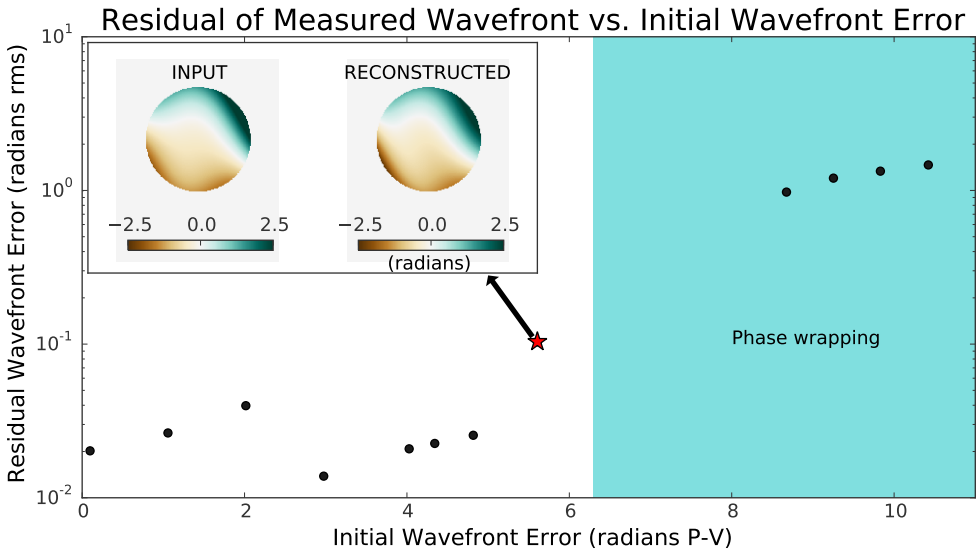

Figure 6.8: The residual wavefront error with increasing peak to valley input aberration. The inset shows wavefront errors $> \pm 2$ radians can be corrected to $\sim$0.1 radians.

Other in-pupil approaches to wavefront sensing use an interferometric analysis with an asymmetric pupil[159] or the differential optical transfer function (dOTF) using

a known pupil modification.[160] The dOTF approach is similar to ours in that it does not need to operate in closed control loop, and it also uses two in-focus images. However, it requires an additional hardware component or specific hardware capability to produce a small pupil obstruction. We discuss the operational differences between our approach and the dOTF method further in Section 6.2.7. Similar to our approach, the asymmetric pupil wavefront sensor (APWFS) can use existing science hardware in the case of JWST, but it works iteratively in closed loop. Our monochromatic case, where we have not applied phase unwrapping (e.g. Fig. 6.8), has similar capture range to APWFS.

Multiwavelength NRM data has been used to resolve phase wrapping ambiguity.[153] Since phase unwrapping is routinely used in successful Gerchberg-Saxton methods,[147] combining these approaches may work well on continuous pupils. Phase unwrapping on segmented apertures raises some fundamental issues that are beyond the scope of this study. Multiwavelength imaging may help resolve some of these issues. The APWFS works only in the regime where the small angle approximation is valid; when the wavefront errors are larger than ~ 1 radians it breaks down.[161] Our approach does not use a small angle approximation. The APWFS operates in a closed control loop with wavefront correction, whereas our approach provides a wavefront estimate with just one set of images. We note that the APWFS measurement could be used to constrain the Gerchberg-Saxton algorithm instead of pistons derived from NRM fringes, so that our initially constrained approach can be used with other JWST

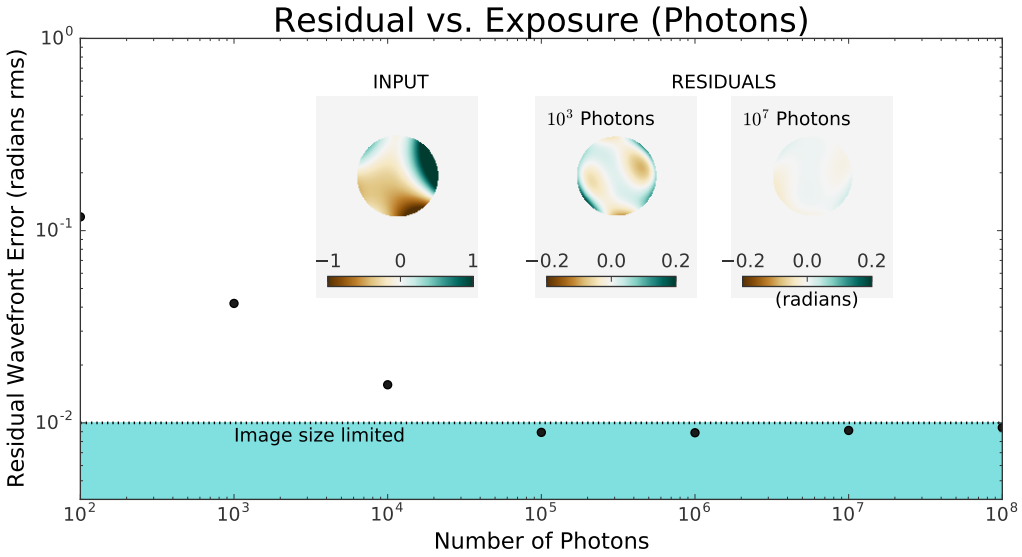

Figure 6.9: We compare results in the case of monochromatic images with photon noise between 1e3 and 1e7 photons. The leftmost panel shows the input pupil phase. The middle and left panels are the measured wavefront in the case of 10^3 and 10^7 photons. In practice on NIRISS 10^6 photons will be easily acquired on bright stars.

instruments that do not contain an NRM.

6.2.4.4 Photon Noise and Exposure Time

Our procedure requires two exposures, one with the full pupil, one with the NRM. We can tolerate fewer counts in the NRM images since the fringe phases are only used to move the estimated pupil phase in the right direction during the first few iterations. Here we consider the necessary exposure time for the full pupil image in the presence of photon noise. We find that even in shallow full pupil exposures, we can reconstruct the wavefront to an accuracy of ∼0.1 radians rms or better (compared to 0.62 radians rms in the initial aberrated pupil), as summarized in Fig. 6.9. The inset plot shows

two examples at 10^3 and 10^7 photons. While the residual error is larger for an exposure of 10^3 photons, the wavefront is recovered to $\sim$0.04 radians. Beyond $\sim 10^5$ photons we reach the reconstruction limit set by our 50 λ/D image size.

Shallow exposure images with the full pupil can be obtained quickly on bright sources with NIRISS. For example, a 7.5 magnitude star in NIRISS F480M filter will take of order seconds to reach 10^7 photons. For the NRM images 10^6 photons should be more than sufficient to achieve better than the 5% precision in pupil phases that we use in these simulations.[162] It will take seconds to reach 10^6 photons on the same 7.5 magnitude star with the NRM.

6.2.5 Finite Bandwith Images matching NIRISS's F480M Filter

In reality, images will be chromatic and will contain other sources of noise, such as from pointing jitter. In this section we extend our analysis to polychromatic images matching the bandwidth of NIRISS's 8% F480M filter. We consider constant transmission across the filter bandwidth centered at 4.8 μm. We additionally add pointing jitter by convolving the PSF with a Gaussian of standard deviation σ = pointing jitter.

The algorithm reconstructs phase errors in the wavefront at the central wavelength. The chromatic effects of our 8% bandwidth images increase the threshold

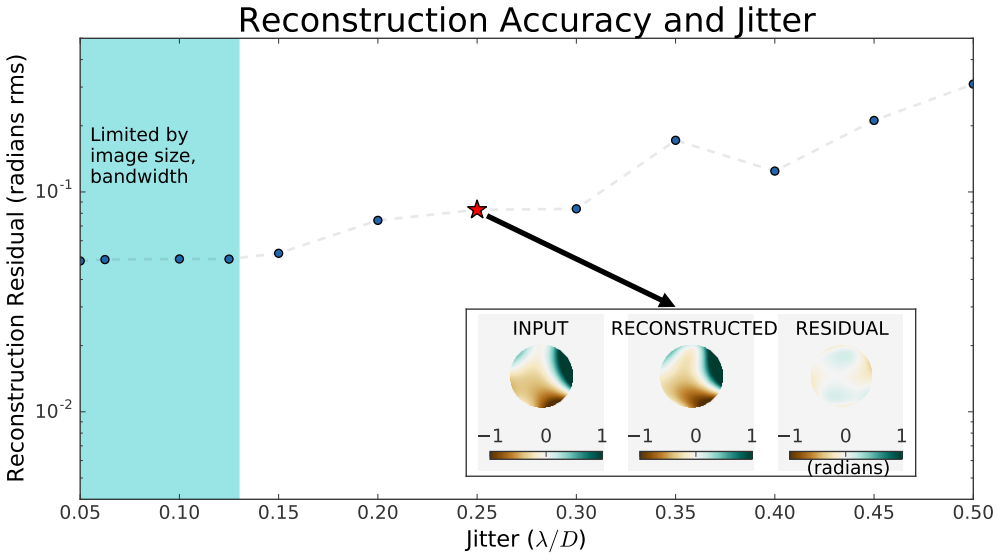

Figure 6.10: We analyze the effect of pointing jitter of up to nearly a full pixel on the rms residual error for 8% bandwidth images that have 10^6 photons. In this case, below about a quarter pixel of jitter, reconstruction error is limited by image size, consistent with the 50 λ/D point in Fig. 6.7. The inset plot shows an example of the reconstruction when the pointing jitter is 0.25 λ/D. The residual wavefront error in this case is < 0.1 radians rms compared to 0.62 radians rms before correction).

reconstruction error. Above ∼0.15 λ/D, jitter is the larger source of error. We summarize these results in Fig. 6.10, and mark the region where the simulation is limited by other sources of error (image size and chromatic bandwidth). The inset plot shows an example of our results in the particular case of $0.25\lambda/D$ jitter and 10^6 photons (data point indicated by a star marker). In our example, which has less than ideal conditions, we are able to recover the wavefront very well, with a residual wavefront error of < 0.1 radians rms. We investigated this effect up to about a full pixel of jitter, 0.5 λ/D, where performance is degraded, but still produces a residual wavefront error of ~ 0.3 radians rms.

The JWST pointing requirement is 7 mas rms,[87] which is ∼0.05 λ/D jitter at 4.8 μm. In our illustrative example we find that our algorithm is limited by the PSF image size (128 pixels) when the jitter is less than $\sim \lambda/8D$. Up to about a quarter pixel of jitter is correctable to ∼0.05 radians rms (or ∼40 nm at the 4.8 μm wavelength). If JWST's pointing jitter remains at or below requirement, it will not be a limiting factor to this kind of wavefront reconstruction.

6.2.6 Correctable Wavefront Errors on the JWST Segmented Mirror

JWST mirror segments have seven actuators. These control the six solid body degrees of freedom as well as the segment radius of curvature.[150] Individual JWST

mirror segments have been measured to have very small aberrations, and are designed to be stiff. The commissioning plan is to adjust segment radius of curvature only during fine phasing,[163] so the range of radius of curvature actuation need only be of the order of $\sim$ 100 nm at ($\sim$ 0.13 radians at 4.8μm). Prior fine phasing, pupil aberrations (including global defocus) are expected to be dominated by misplaced primary mirror segments, and, during early commissioning, from a misaligned secondary.

In this section we consider piston, tilt and focus segment aberrations, errors which are expected from segment drifts between phasing. We apply our algorithm to images made with a pupil matching the JWST primary hexagonal segments and mirror obstructions. For this example we do not consider the central obstruction in the CLEARP pupil (Fig. 6.3 right). We use the Hexike polynomials implemented in WebbPSF[164,165] for smoothing the measured wavefront each iteration. We do not assume anything about the particular set of Hexike terms present in the wavefront. In practice, it may be useful to limit smoothing modes to only piston, tip/tilt, and focus. In these test cases, we consider images that are sampled three times better than NIRISS's F480M filter to focus on the algorithm performance for a segmented pupil rather than sampling effects. We use images of size 524 pixels ($\sim 74\lambda/D$).

6.2.6.1 Segment Tilt

In the special case of pure, random segment tip/tilt with no segment piston or higher order aberrations, constraining the GS with NRM data (which measures hole

piston) only supplies zero piston constraint over all holes. In our pure segment tilt test case the constrained GS did not recover all the segment tilts correctly. Because this is a special case, we address segment tilt separate from piston and defocus.

Once mixed with any other (symmetric) phase, NRM can break the GS ambiguity. When we added coma (a global aberration that often arises from secondary mirror misalignment) the wavefront was retrieved unambiguously (Fig. 6.11). We also mix tilt with segment piston and focus, and again recover the wavefront (Fig. 6.12).

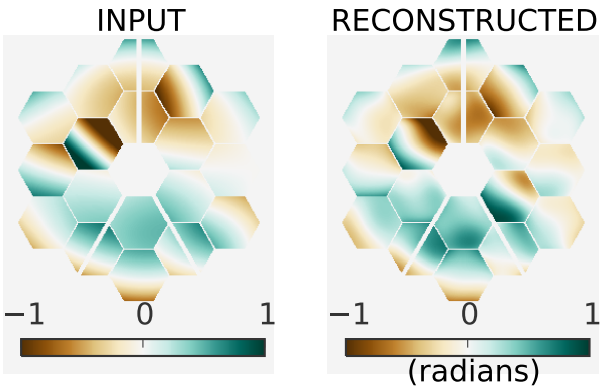

Figure 6.11: Segment tip/tilt is mixed with a global coma. The initial wavefront errors are 0.35 radians rms and the reconstruction residuals are 0.14 radians rms.

6.2.6.2 Combinations of Segment Piston, Tilt and Focus

In general we may expect a combination of segment-base wavefront errors, of which piston, tilt and focus are correctable. We split these into pure segement defocus and pure segment piston as a demonstration of correcting single even functions on the JWST segmented pupil. Both defocus and piston introduce nonzero fringe phases in

the NRM image (since the NRM holes are smaller than the segments). In reality, piston error on a curved segment contributes other aberrations. We then mix segment piston, tilt, and focus errors (Fig. 6.12-bottom) and can reconstruct both the symmetric and antisymmetric wavefront error terms unambiguously. While the accuracy of wavefront retrieval is reduced at segment edges and obstructions, the general structure and the sign of the phase is preserved in the reconstruction. Fine tuning this procedure may manage segment edges and obstructions either with different smoothing function, or by incorporating a gain factor for known discontinuities.

6.2.6.3 Secondary Mirror Misalignment

JWST wavefront sensing has been developed around using NIRCam. NIRCam uses specialized hardware to determine segment co-phasing, and large and small wavefront aberrations. All wavefront sensing is initially performed at one field point in NIRCam. This telescope phasing may result in a sub-optimal positioning of the secondary mirror due to a degenerate combination of certain primary and secondary misalignment modes that cannot be sensed at a single field point. In order improve the wavefront in other JWST instruments, wavefront sensing needs to be performed in the other imaging instruments, namely NIRISS and JWST's Mid-Infrared Imager (MIRI). The most thoroughly tested approach to this Multi-Instrument Multi-Field (MIMF) wavefront sensing[166] involves sweeping through focus with a secondary mirror move and using a focus-diverse Misell-Gerchberg-Saxton phase retrieval algorithm.[144,146]

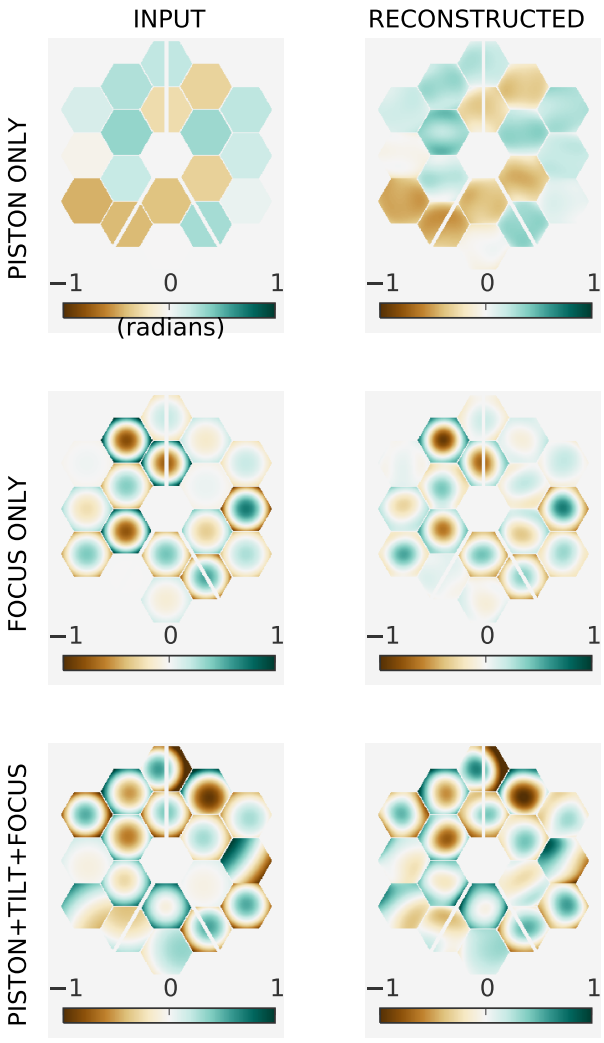

Figure 6.12: We simulate segment piston, tip/tilt, and focus aberrations on the JWST pupil simulating the F480M filter bandwidth and $\sim$ 7 mas jitter. The left column shows the input and the right the reconstructed wavefront. In the case of pure segment piston (top) the input wavefront has 0.27 radians rms global wavefront error and the reconstruction residual has 0.06 radians rms. For the case of pure segment defocus (middle) the input wavefront produces a global wavefront error of 0.25 radians rms, while the reconstructed wavefront has residual error of 0.1 radians rms. In the combined piston, tip/tilt, and focus case the input wavefront has 0.34 radians rms phase and the reconstruction residual has 0.1 radians rms. At a wavelength of 4.8μm 0.1 radians corresponds to 76nm.

Using our approach, we can accomplish an unambiguous wavefront measurement by combining NIRISS' CLEARP and NRM pupil masks without invoking a secondary mirror move. This might enable a shorter commissioning period for JWST, since the secondary mirror focus sweep is a slow exercise.

A mixture of astigmatism and coma are likely to result from the secondary mirror misalignment. In NIRISS this aberration might be up to 200 nm in size. In Fig. 6.13 we show a simulated measurement of this kind of aberration using our method. From this single measurement we cannot determine where the aberrations are from (primary or secondary misalignments), but NIRISS can add an additional field point compared to NIRCam's wavefront measurements. Multiple field points are required to determine the secondary misalignment without moving the secondary.

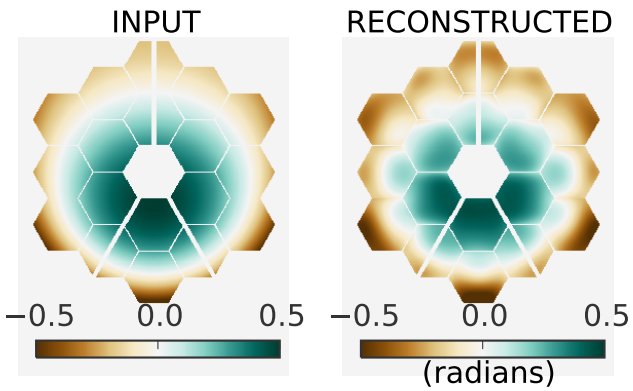

Figure 6.13: Unaberrated segments with secondary mirror misalignment (MIMF).[166] Our constrained GS approach will be able to reconstruct low order global aberrations in the F480M filter on NIRISS, observing with a star of magnitude of 7.5 and an exposure time of $<$ 1s, with $\sim$ 7 mas jitter. In this test case the initial wavefront error is 0.22 radians rms and the reconstruction residuals are 0.04 radians rms.

6.2.7 Discussion

Our constrained Gerchberg-Saxton approach to phase retrieval provides an efficient way to measure wavefront aberrations on current and future space telescopes using only in-focus images. The algorithm is suited to both continuous and segmented/obstructed pupils, though segment obstructions appear to limit the performance in our simple implementation. We use the first 15 Zernike or Hexike polynomial to smooth the wavefront in the pupil. We smooth over the full pupil in the case of a continuous pupil, and segment-wise in the case of the segmented pupil, using the appropriate set of polynomials. Alternative basis functions could handle different wavefront errors better. We ignore the edge effects of thin pupil obstructions. Mitigating the errors introduced by these effects may take more study.

In this section we have discussed our wavefront retrieval approach primarily in the context of commissioning JWST, although the method could provide wavefront knowledge during JWST science observations (for example, to support image deconvolution). On JWST this work may help avoid some secondary mirror focus sweeps during the commissioning phase of the telescope. We have presented a proof of concept of our method; further optimization of the method can be tailored to individual cases.

On JWST, two in-focus exposures containing 10^6 photons each (requiring exposure times of $<$ 1s full pupil images and seconds in NRM images for a star of 7.5^{th} magnitude through the F480M filter) will provide enough signal to measure the wavefront

errors of ~ 100 nm, even in the presence of jitter, finite bandwidth and limited image size. Chromatic smearing, and finite image size are larger sources of error than the anticipated pointing jitter of JWST. Our method can tolerate up to 16 mas of pointing jitter, which is twice as large as JWST's required pointing accuracy. Frequent monitoring of mirror segment drift can be measured with our approach on NIRISS (which contains the 7-hole NRM used in this study) as a part of normal telescope operations. This provides a complimentary capability to trend wavefront stability over time in NIRISS alongside the main wavefront sensing monitoring program using NIRCam.

We have focused on using a non-redundant mask to break the phase degeneracy in the unconstrained GS algorithm. It may also be possible to accomplish this with a redundant pupil that possesses asymmetries, using the asymmetric pupil wavefront sensor (APWFS) method,[159] which also uses in-focus images. The APWFS algorithm could be used on data from other JWST instruments, such as NIRCam or MIRI.

Our method has some key differences compared to the differential optical transfer function approach to wavefront sensing. The dOTF method similarly requires two in-focus images, one with a pupil modification, though the modification must be small. For JWST, Codona[160] suggests using small motions of the pupil wheel to block a portion of the pupil and achieve its required pupil diversity, which is not possible for MIRI's rachet-mechanism filter wheel. Our constrained GS approach uses two standard filter settings on NIRISS. With the possibility of using APWFS

measurements, a single image could suffice for doing constrained GS wavefront sensing with MIRI.

Using these methods for both monolithic and segmented future telescopes (such as the Wide Field Infrared Survey Telescope[167] or the High Definition Space Telescope[3]) can utilize science hardware for wavefront sensing, which has obvious benefits for weight, cost, complexity, and scope.

6.3 Preliminary Constrained Gerchberg-Saxton Laboratory Results

This section builds upon the theoretical work developing a constrained GS algorithm using NIRISS's NRM and an arbitrary pupil in the previous sections of this Chapter. We test the algorithm on laboratory data and show some preliminary results. In Section 6.3.1 we discuss progress with laboratory demonstrations at the Makidon Optics lab at the Space Telescope Science Institute. In Section 6.3.2 we discuss future work that can verify our laboratory results and extension of our algorithm using another interferometric approach to provide the pupil constraint.

6.3.1 Progress on laboratory tests

Our implementation of the constrained GS procedure in the pupil plane for lab data is as follows:

- Measure pistons over each hole from NRM data
- Set numerical pupil phase equal to measured pistons over the region of the mask holes in each iteration
- Keep the phases determined by GS everywhere else.
- Zero mean phase and smooth with a set of low-order polynomials to remove high frequency noise.
- Set pupil amplitude equal to the pupil support.

We do not interpolate between NRM hole locations letting the phase in these regions evolve over time. In the image plane we replace the amplitude with the square-root of the PSF. After the difference in pupil phase between consecutive iterations falls below 10^{-2} radians RMS, we remove the constraint.

We assume our laboratory data is dominated by low order aberrations. We smooth the phase each GS iteration with the first 15 Zernike polynomials. We use 400 pixels across our numerical pupil in the retrieval.

6.3.1.1 Bench Setup

Data were taken in the summers of 2014 and 2015 at the STScI Makidon Optics Laboratory with a simple setup that allows an NRM or circular pupil to be used. Figure 6.14 shows our basic lab setup. Our two different pupils were placed in the collimated portion of the beam between the two mirrors. We took exposures using each pupil and subtracted the dark background. In this experiment we used a glass microscope slide to add small phase aberrations. We ran sets of exposures both with (GLASS) and without (CLEAR) the slide in the path of the beam. Our source is centered at 650nm with a $\sim 1\%$ bandpass.

6.3.1.2 Data cleaning

Before running our phase retrieval algorithm we reduced the data to clean up dark background, noise, and bad pixels in the camera. First we took the median image over all source and dark exposures. We subtracted the dark background and cropped our image down to the portion containing the signal. We treated bad pixels using a nearest neighbor average[1].

We then filtered the data in the Fourier plane by setting signal outside the pupil support to zero and transforming the data back to the image plane. The pupil support in this step was chosen by eye and was slightly oversized. This led to slight extra ringing in the filtered PSF. Our PSF signal is reliable to only about the first 6 or

[1]Using the bfixpix routine from http://www.lpl.arizona.edu/ ianc/python/nsdata.html

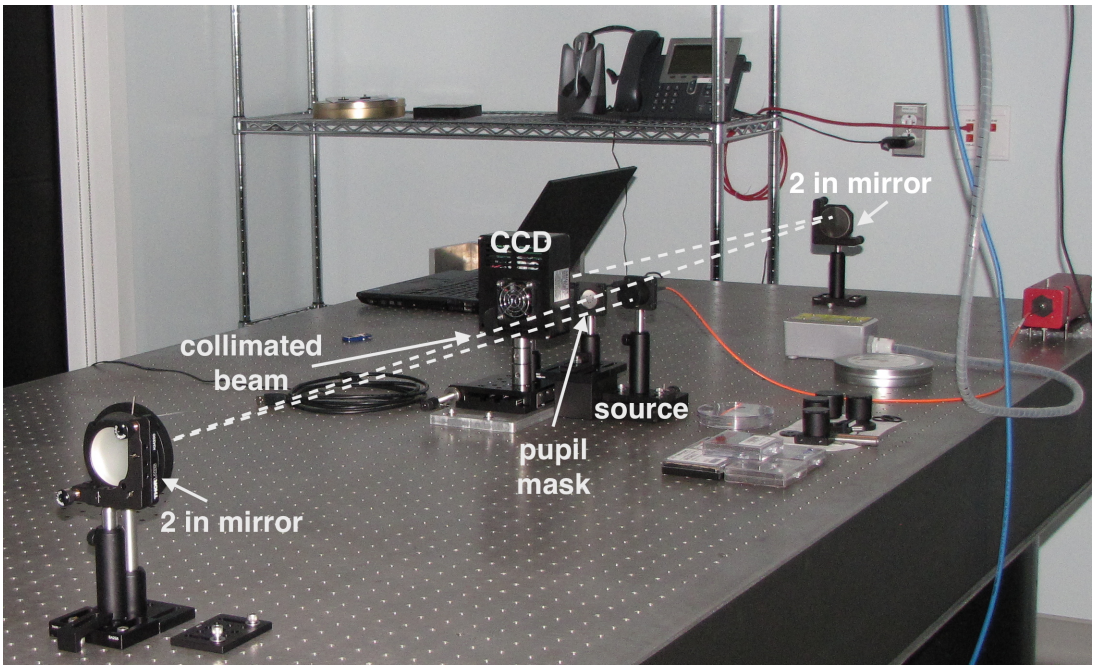

Figure 6.14: A picture of our bench set up, which included a thermal source, cicular pupil stop, G7S6 design NRM, two 2-inch mirrors, and an SBIG CCD camera. The Source was placed one focal length from the first mirror. Pupils were placed in the path of the collimated beam between the two mirrors. We chose to use a small pupil roughly the size of the longest baseline on our NRM, and also to take advantage of the higher quality part of the mirrors, closer to the center

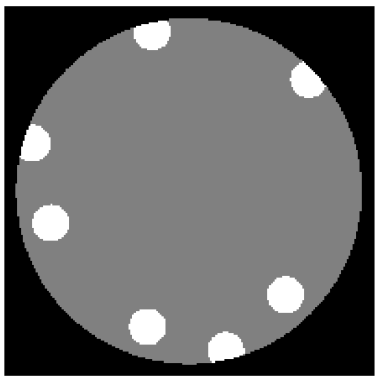

Figure 6.15: Constraint region (white) overlaid on the full PSF pupil (gray). We use slightly undersized circular holes that fit entirely within each hexagonal subaperture for the pupil constraint.

7 Airy rings. These basic steps were sufficient to feed our full pupil PSFs into our phase retrieval algorithm.

6.3.1.3 Extracting NRM phases

The NRM-derived pupil phases are only a first estimate of the pupil phase and do not need to be very precise. We measured visibility phases in the Fourier transform of the data, averaging over each visibility splodge. We then solved for zero mean pupil phases. Our "full pupil" was slightly undersized compared to the mask holes. We carefully matched the two pupils in our numeric arrays to reflect their true sizes. We applied the pupil pistons over circles that fit within each full hexagonal subaperture. Figure 6.15 shows the region in which we replace NRM-derived pupil phases (in white).

6.3.1.4 Results

We ran our constrained Gerberg-Saxton algorithm, using the pupil phase estimate from the NRM images as a starting guess. We applied the NRM-derived constraint until the difference between pupil phase in consecutive iterations exceeded 10^{-2} radians rms. Afterwards, we lifted the constraint and let the algorithm converge so that the difference between consecutive iterations was below 10^{-5} radians rms. We smoothed the pupil phase each iteration with a set of 36 Zernike polynomials. We performed this procedure on cleaned data with and without the glass slide.

As a first test to verify our results we simulated full-pupil PSFs given the measured phase errors and compared those to our cleaned data. Our reconstructed PSFs closely match the data. In Figure 6.16 we show this comparison on the right half of the figure. The left shows our retrieved phase and the pupil constraint used to start our GS algorithm. We are working on aligning interferometer measurement of our glass slide with its position on the testbed, to verify these results.

We also varied the pixel scale by up to $\pm 5.0\%$ to test how sensitive our results were to a possible mismatch in PSF sampling. We provided a guess for the pixel scale to start, close to the true value. For the GLASS data we see very little change in our recovered phase. However, for the CLEAR data we measure a different phase when the pixel scale is too far from the correct value. In this case the reconstructed PSF does not match the data, indicating that the solution is incorrect.

Figure 6.17 shows how the results change as we modified the pixel scale. For the

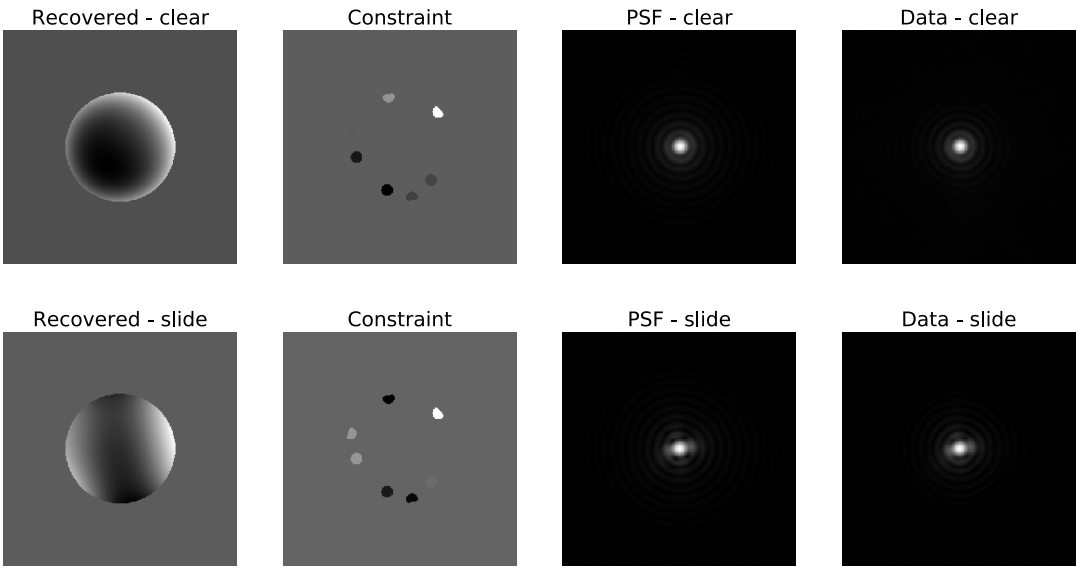

Figure 6.16: Phase retrieval results for CLEAR on the top, and slide on the bottom. On the left are the recovered phases with global tilt removed and zero mean. In the center are the NRM-derived pupil pistons that we used as a constraint in the first set of GS iterations. On the right are PSFs constructed from the phases on the left assuming uniform illumination in the pupil.

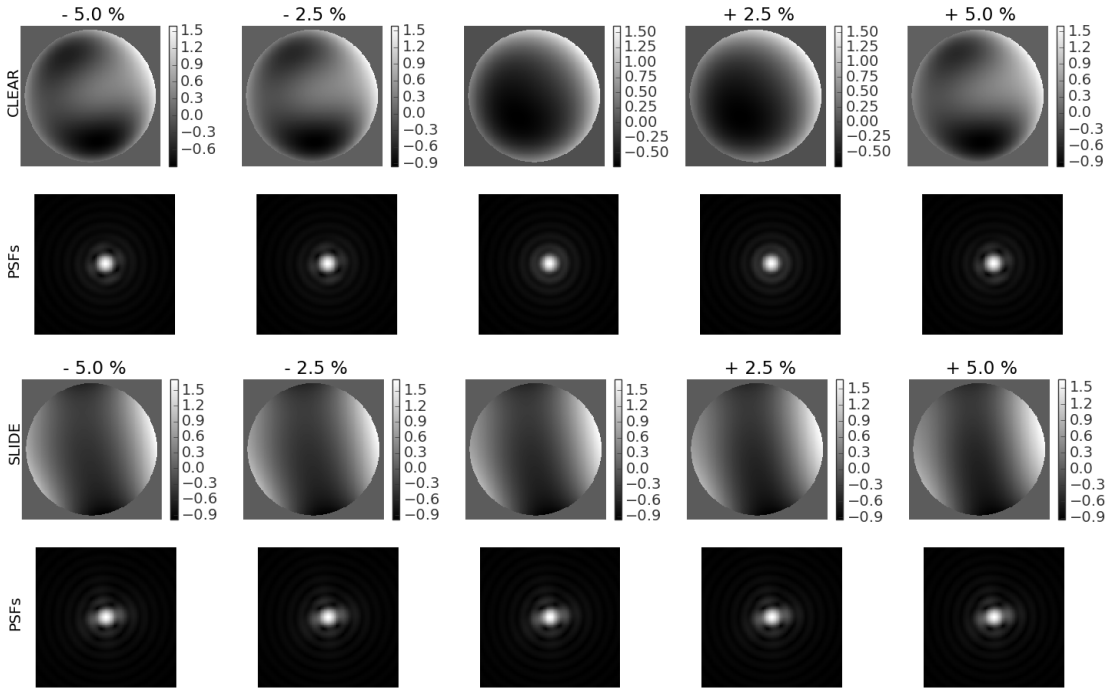

Figure 6.17: Varying the pixel scale in our phase retrieval: We calculate the wavefront in radians on each dataset by running our algorithm with up to ±5% change in the pixel scale. The results are displayed from −5% to 5% from left to right, with the recovered wavefront shown above the reconstructed PSF. On top are the CLEAR data and on the bottom are the GLASS data. Our results indicate that some mismatch in the pixel scale can be tolerated.

CLEAR data the PSF only matches the data in cases of the nominal pixel scale value and the +2.5% change (columns 3 and 4, in the top panel). Phase retrieval of the GLASS data (bottom panel) all show similar structures and all the reconstructed PSFs match our data (Figure 6.16, rightmost column). These results indicate that 1-2% of error in the pixel scale is tolerable, which agrees with some simple simulations. Pixel scale tolerance may vary with different aberration shapes explaining the difference between the CLEAR and GLASS reconstructions at large pixel scale errors.

6.3.2 Future work for the constrained Gerchberg-Saxton algorithm

This study describes our latest work using a modified Gerchberg-Saxton algorithm to measure the wavefront of data we obtained in our lab. We use the phase retrieval results to reconstruct PSFs and compare with our data. This is a first step in verifying the approach in a lab experiment. Using interferometer measurements of our glass slide, we plan to compare the measured glass wavefront with our phase retrieval results. Ongoing work includes aligning the glass slide wavefront measurements with its setup on our testbed.

This method can be straightforwardly applied to other existing point source images. NIRISS cryovacuum tests include images using both the NRM and full pupil. We also plan to use this algorithm on existing GPI data, primarily using its internal source. Our method could provide a measurement of the wavefront including non-common path aberrations between the wavefront sensor and the focal plane. In closed loop on sky, it is possible that enough data could be taken in stable conditions between NRM and full pupil exposures to make an estimate of GPI's wavefront, but it will be challenging. It is also difficult to find a source that is bright enough for the NRM and faint enough to not saturate the full pupil.

We demonstrate our constrained phase retrieval using phases measured from NRM data. It is likely that other interferometric approaches like the asymmetric pupil

Fourier wavefront sensor[?] could also be used to start a GS loop in the right direction. In the case of a future space telescopes that will likely be segmented, or contain spiders there should already be sufficient asymmetry for this approach to provide a close first estimate of the phase. Wavefront sensing that combines these two approaches would only require one in-focus image. This could make our phase retrieval approach more practical for ground-based AO data. In the context of JWST mirror phasing, this could expand our method to work both with NIRISS and MIRI images, providing estimates of the phase at two different parts of the field compared with baseline wavefront sensing on NIRCam. For future space telescopes this approach enables wavefront sensing without dedicated hardware, especially if it can be done with one image.

Chapter 7

Looking towards the future

The field of planet formation and exoplanet demographics has been extremely observationally driven, especially in the last decade. The huge demographics of exoplanets discovered through transit and radial velocity measurements predicted the presence of young gas giant planets within 20AU from their stars that could be observed with sufficient contrast and adaptive optics performance with the new generation of ground-base planet imagers. The new ground based imagers have begun to reveal that either fewer planets exist in wider orbit, or they are intrinsically less bright than previously thought. Upcoming missions, like JWST and WFIRST will expand the search with improved stability at infrared wavelengths and deeper contrast a short wavelengths, respectively.

Major questions still remain in putting the direct imaging observations in context. Ages of directly imaged stars are often assumed from their coeval groups or other

indicators.[168] Since estimated masses of new directly imaged systems depend on the assumed ages there remains a lot of uncertainty in characterizing the demographics of young, wide separation giant planets. Testing evolutionary models with low mass binaries at more moderate contrasts can provide more direct measurements of mass and dynamics. High resolution is required to overlap radial velocity sensitivity and resolve msini mass uncertainty. Advancement will come in deeper contrasts at small inner working angles as well as sensitivity to lower mass primaries that cannot be observed from the ground due to their faintness. JWST's infrared instruments will target companions to M dwarf primaries, which will be intrinsically cooler, but at moderate contrast.

We investigated limiting systematics for non-redundant masking data analysis, presenting an image-plane based algorithm for measuring fringe visibilities. Image-plane methods sidestep bad pixels, can model pixel varied response and undersampled images, and can potentially manage saturated data. The image plane approach is also appropriate for ground-based IFU data, which has small fields of view, in general. Our analysis identified the importance of accurate pointing on JWST-NIRISS in order to mitigate flat field errors across the detector. Accurate placement of the target object will help calibrate out any systematic effects coming from pixel variations and other instrument effects. This work has guided the observing plan for NIRISS-AMI target acquisition and integration and led to analysis of early JWST-NIRISS test data.[61]

We presented the results and lessons learned from commissioning the NRM on the

Gemini Planet Imager. The experience outlines the utility of having an NRM, both for complementary science at small inner working angles, as well as instrument diagnosis. There are few stars for which GPI can lock on with the AO system that do not also saturate the detector, before recent upgrades that added a neutral density filter. Asymmetry in NRM images were able to diagnose a defocus in direct (non-occulted) exposures. The NRM also identified bad on-telescope vibrations that were not present in internal source exposures. While a few science observation early in commissioning demonstrated the NRM resolution inside the region of the coronagraphic occulter, recent upgrades to the instrument will allow the best NRM performance yet.

As of May 2016 the NRM is reaching 5σ contrast of a few 10^3. According to models of, e.g. Baraffe et al. (2015)[169] GPI's NRM is sensitive to low mass stars and brown dwarfs around primaries of a range of stellar types and ages $1 - 10Myr$. At least an order of magnitude better contrast with NIRISS at 4μm will be able to reach much smaller companion masses, where their infrared thermal emission will be peaking as the stellar radiation is falling. An illustrative example of this can come from plotting black body curves for objects from a range of temperatures. For this example we use models from Burrows et al. (2001)[170] assuming an age of 1 Myr. NRM on an instrument like GPI, operating at the short end of IR, where the atmosphere is not as bright, will fall short of planetary mass companions to solar-type stars. At NIRISS bands the contrast ratios are more moderate and the same contrast begins to probe planetary masses. An extra order of magnitude better contrast afforded from a stable

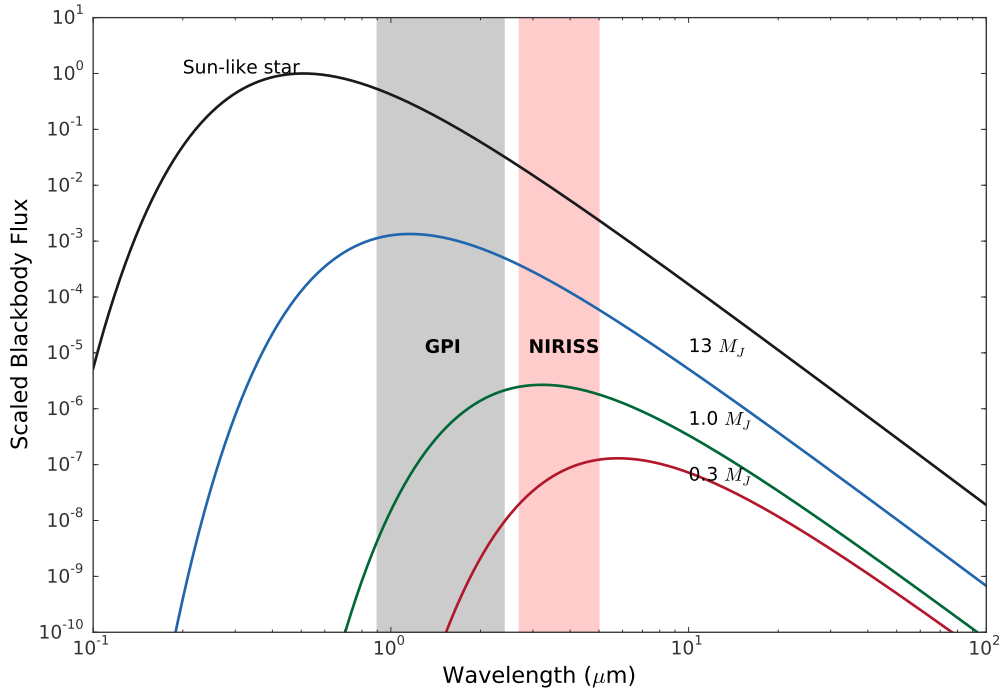

Figure 7.1: A simple illustration of the gain in sensitivity toward companion mass by gaining an order of magnitude better contrast farther into infrared wavelengths. NIRISS will be able to probe lower, possibly planet mass objects compared to what is accessible with ground-based NRM. This simple demonstration assumes perfect blackbody emission and uses mass-temperature relations from Burrows 2001 models at an age of 1 Myr. The observing bands for GPI and NIRISS are shown in shaded regions.

space telescope can probe even lower in mass. WFIRST, which will observe in visible light, all the way to the left of the plot, will target reflected light from planets rather than thermal emission, which will clearly be too challenging, even for a space-borne coronagraph. State of the art coronagraphy coupled with wavefront control will allow WFIRST to detected the reflected light.

High resolution imaging goes hand in hand with coronagraphic instruments, together sensitive to a larger parameter space in contrast and separation from the

host star. We presented recent work applying a new forward modeling algorithm for Karhunen-Loeve Image Projects, a PCA-based approach to PSF subtraction. In the challenging conditions of angular or spectral differential imaging the reference library for PSF subtraction necessarily contains the astrophysical signal we are trying to measure, and so general KLIP can underestimate its flux, especially if the signal is especially faint or close in to the coronagraphic mask, where more aggressive PSF subtraction must be done. We demonstrate KLIP-FM in practice accounting for the missed flux by estimating over-subtraction and self-subtraction of the signal. We apply this method to a particularly noisy dataset in early GPI commissioning of the star HR8799 containing 4 directly imaged giant planets, in an attempt to measure the K-band spectrum of the closest in planet HR8799e.

From the ground, with GPI plan to follow up transitional disks at close in separations corresponding to the disk gaps to look for new companions or rule out their presence above some mass limit. Spectroscopic measurements will help characterize known companions and any new discoveries and may help constrain accretion properties and effective temperatures. Future work includes leveraging the spectral dimension for differential as is done in Long baseline optical interferometry.[140,141]

We have demonstrated the $< 1\%$ polarization precision of the GPI NRM in polarimetry mode, when conditions are appropriate. The remaining test is to observe young systems with close in disks and detect their polarized signal. Many transitional disks have structures predicted by their spectral energy distributions, possibly

further characterized by imaging and interferometry. In some cases GPI NRM will be able to confirm structures probed by instruments like ALMA, and in other cases GPI NRM will be able to measure new constraints on inner disk structures. The polarized signal measured in azimuth around the host stars will provide information on the composition and scattering properties of the grains. Modeling the properties of these disks will help put these observations in context.

There are many exciting science opportunities to pursue with NIRISS-AMI both in point sources and extended objects. In the search for new young exoplanets or low mass companions, NIRISS-AMI will aim to reach contrasts of 10^4 on the brightest sources at an inner working angle of $\sim 60-70$mas. These sources will be bright enough for ground-based ex-AO imagers, but too bright for the unmasked NIRISS detector. NIRISS-AMI will aim for moderate contrast around fainter targets, like M dwarf primaries. Low mass companions to these stars will have less severe contrast ratios. NIRISS-AMI should have many synergies with RV and GAIA astrometry detections around close (within $\sim$ 30pc) low mass primaries.[171] Monitoring these companions through both imaging and either radial velocity or astrometry will yield direct mass and luminosity measurements of low mass objects. The stability of JWST will also enable better image reconstruction than ground-based NRM. NIRISS will target young disks, solar system bodies, and active galactic nuclei, among other possible interesting possibilities. A combination of forward modeling and image reconstruction will be necessary.

There are advantages and drawbacks to masking the NIRISS pupil to remove redundancy. The major drawback is that a significant fraction of the light is masked and integration times will be long for faint targets. On the other hand, NRM can look at very bright targets and reach sub-λ/D resolution. Kernel phase will also play an important roll on NIRISS and other JWST instruments, as it has been demonstrated on archival Hubble Space Telescope data.[64] Together these two methods will provide the high spatial resolution imaging available to JWST. For the two similar methods the accumulation of reference stars will provide enough observations to set up KLIP for NRM, matching the ALICE project with *HST*.[116]

Wavefront sensing and control is an important component of developing next generation ground and space-based high contrast instruments. We have outlined a new approach to phase retrieval that does not require any moving mirrors to introduce defocus for phase diversity. Instead we use an NRM to break the pupil symmetry and constrain phase retrieval on a full pupil image. This procedure requires only two images to gain enough information to measure the wavefront. It stands apart from closed-loop wavefront sensing and is appropriate for active control on space-based segmented telescopes. Combined with a starting guess from the asymmetric pupil Fourier wavefront sensor, this approach would only require a single image. Every science image could also come with a measurement of the wavefront, helping to monitor the alignment of the optics over time and providing additional image quality information to the observer.

Bibliography

[1] ALMA Partnership, C. L. Brogan, L. M. Pérez, T. R. Hunter, W. R. F. Dent, A. S. Hales, R. E. Hills, S. Corder, E. B. Fomalont, C. Vlahakis, Y. Asaki, D. Barkats, A. Hirota, J. A. Hodge, C. M. V. Impellizzeri, R. Kneissl, E. Liuzzo, R. Lucas, N. Marcelino, S. Matsushita, K. Nakanishi, N. Phillips, A. M. S. Richards, I. Toledo, R. Aladro, D. Broguiere, J. R. Cortes, P. C. Cortes, D. Espada, F. Galarza, D. Garcia-Appadoo, L. Guzman-Ramirez, E. M. Humphreys, T. Jung, S. Kameno, R. A. Laing, S. Leon, G. Marconi, A. Mignano, B. Nikolic, L.-A. Nyman, M. Radiszcz, A. Remijan, J. A. Rodón, T. Sawada, S. Takahashi, R. P. J. Tilanus, B. Vila Vilaro, L. C. Watson, T. Wiklind, E. Akiyama, E. Chapillon, I. de Gregorio-Monsalvo, J. Di Francesco, F. Gueth, A. Kawamura, C.-F. Lee, Q. Nguyen Luong, J. Mangum, V. Pietu, P. Sanhueza, K. Saigo, S. Takakuwa, C. Ubach, T. van Kempen, A. Wootten, A. Castro-Carrizo, H. Francke, J. Gallardo, J. Garcia, S. Gonzalez, T. Hill, T. Kaminski, Y. Kurono, H.-Y. Liu, C. Lopez, F. Morales, K. Plarre, G. Schieven, L. Testi, L. Videla, E. Villard, P. Andreani, J. E. Hibbard, and K. Tatematsu, "The 2014

ALMA Long Baseline Campaign: First Results from High Angular Resolution Observations toward the HL Tau Region," *Astrophysical Journal Leters*, vol. 808, p. L3, Jul. 2015.

[2] S. M. Andrews, D. J. Wilner, Z. Zhu, T. Birnstiel, J. M. Carpenter, L. M. Pérez, X.-N. Bai, K. I. Öberg, A. M. Hughes, A. Isella, and L. Ricci, "Ringed Substructure and a Gap at 1 au in the Nearest Protoplanetary Disk," *Astrophysical Journal Leters*, vol. 820, p. L40, Apr. 2016.

[3] J. Dalcanton, S. Seager, S. Aigrain, S. Battel, N. Brandt, C. Conroy, L. Feinberg, S. Gezari, O. Guyon, W. Harris, C. Hirata, J. Mather, M. Postman, D. Redding, D. Schiminovich, H. P. Stahl, and J. Tumlinson, "From cosmic birth to living earths: the future of UVOIR space astronomy," *ArXiv e-prints*, Jul. 2015.

[4] B. Macintosh, J. R. Graham, P. Ingraham, Q. Konopacky, C. Marois, M. Perrin, L. Poyneer, B. Bauman, T. Barman, A. S. Burrows, A. Cardwell, J. Chilcote, R. J. De Rosa, D. Dillon, R. Doyon, J. Dunn, D. Erikson, M. P. Fitzgerald, D. Gavel, S. Goodsell, M. Hartung, P. Hibon, P. Kalas, J. Larkin, J. Maire, F. Marchis, M. S. Marley, J. McBride, M. Millar-Blanchaer, K. Morzinski, A. Norton, B. R. Oppenheimer, D. Palmer, J. Patience, L. Pueyo, F. Rantakyro, N. Sadakuni, L. Saddlemyer, D. Savransky, A. Serio, R. Soummer, A. Sivaramakrishnan, I. Song, S. Thomas, J. K. Wallace, S. Wiktorowicz, and S. Wolff,

"First light of the Gemini Planet Imager," *Proceedings of the National Academy of Science*, vol. 111, pp. 12 661–12 666, Sep. 2014.

[5] J.-L. Beuzit, M. Feldt, K. Dohlen, D. Mouillet, P. Puget, F. Wildi, L. Abe, J. Antichi, A. Baruffolo, P. Baudoz, A. Boccaletti, M. Carbillet, J. Charton, R. Claudi, M. Downing, C. Fabron, P. Feautrier, E. Fedrigo, T. Fusco, J.-L. Gach, R. Gratton, T. Henning, N. Hubin, F. Joos, M. Kasper, M. Langlois, R. Lenzen, C. Moutou, A. Pavlov, C. Petit, J. Pragt, P. Rabou, F. Rigal, R. Roelfsema, G. Rousset, M. Saisse, H.-M. Schmid, E. Stadler, C. Thalmann, M. Turatto, S. Udry, F. Vakili, and R. Waters, "SPHERE: a planet finder instrument for the VLT," in *Society of Photo-Optical Instrumentation Engineers (SPIE) Conference Series*, vol. 7014, Aug. 2008.

[6] A. Cumming, R. P. Butler, G. W. Marcy, S. S. Vogt, J. T. Wright, and D. A. Fischer, "The Keck Planet Search: Detectability and the Minimum Mass and Orbital Period Distribution of Extrasolar Planets," *Publications of the Astronomical Society of the Pacific*, vol. 120, pp. 531–554, May 2008.

[7] S. Lacour, P. Tuthill, P. Amico, M. Ireland, D. Ehrenreich, N. Huelamo, and A.-M. Lagrange, "Sparse aperture masking at the VLT. I. Faint companion detection limits for the two debris disk stars HD 92945 and HD 141569," *Astronomy Astrophysics*, vol. 532, p. A72, Aug. 2011.

[8] A. Z. Greenbaum, S. Sivaramakrishnan, L. Pueyo, P. Ingraham, S. Thomas,

S. Wolff, M. D. Perrin, B. Norris, and P. G. Tuthill, "Wavelength Calibration and Closure Phases with the Gemini Planet Imager," in *Society of Photo-Optical Instrumentation Engineers (SPIE) Conference Series*, vol. 8864, Aug. 2013.

[9] B. Norris, G. Schworer, P. Tuthill, N. Jovanovic, O. Guyon, P. Stewart, and F. Martinache, "The VAMPIRES instrument: imaging the innermost regions of protoplanetary discs with polarimetric interferometry," *Monthly Notices of the Royal Astronomical Society*, vol. 447, pp. 2894–2906, Mar. 2015.

[10] A. C. Cheetham, J. H. V. Girard, S. Lacour, G. Schworer, H. X., and B. J.-L., "Sparse aperture masking with sphere," in *Society of Photo-Optical Instrumentation Engineers (SPIE) Conference Series*, vol. 9907, Jul. 2016.

[11] M. S. Marley, J. J. Fortney, O. Hubickyj, P. Bodenheimer, and J. J. Lissauer, "On the Luminosity of Young Jupiters," *Astrophysical Journal*, vol. 655, pp. 541–549, Jan. 2007.

[12] S. E. Strom, S. Edwards, and M. F. Skrutskie, "Evolutionary time scales for circumstellar disks associated with intermediate- and solar-type stars," in *Protostars and Planets III*, E. H. Levy and J. I. Lunine, Eds., 1993, pp. 837–866.

[13] J. B. Pollack, O. Hubickyj, P. Bodenheimer, J. J. Lissauer, M. Podolak, and Y. Greenzweig, "Formation of the Giant Planets by Concurrent Accretion of Solids and Gas," *Icarus*, vol. 124, pp. 62–85, Nov. 1996.

[14] A. P. Boss, "Giant planet formation by gravitational instability." *Science*, vol. 276, pp. 1836–1839, 1997.

[15] K. M. Kratter, R. A. Murray-Clay, and A. N. Youdin, "The Runts of the Litter: Why Planets Formed Through Gravitational Instability Can Only Be Failed Binary Stars," *Astrophysical Journal*, vol. 710, pp. 1375–1386, Feb. 2010.

[16] S. A. Metchev and L. A. Hillenbrand, "The Palomar/Keck Adaptive Optics Survey of Young Solar Analogs: Evidence for a Universal Companion Mass Function," *Astrophysical Journal Supplement Series*, vol. 181, pp. 62–109, Mar. 2009.

[17] C. Espaillat, J. Muzerolle, J. Najita, S. Andrews, Z. Zhu, N. Calvet, S. Kraus, J. Hashimoto, A. Kraus, and P. D'Alessio, "An Observational Perspective of Transitional Disks," *Protostars and Planets VI*, pp. 497–520, 2014.

[18] A. C. Rizzuto, M. J. Ireland, T. J. Dupuy, and A. L. Kraus, "Dynamical Masses of Young Stars. I. Discordant Model Ages of Upper Scorpius," *Astrophysical Journal*, vol. 817, p. 164, Feb. 2016.

[19] D. Thatte, A. Greenbaum, A. Martel, A. Sivaramakrishnan, and É. Artigau, "Astrometric accuracy of aperture making interferometry with JWST-NIRISS," in *Techniques and Instrumentation for Detection of Exoplanets VII*, ser. Society of Photo-Optical Instrumentation Engineers (SPIE) Conference Series, vol. 9605, Sep. 2015, p. 96052F.

[20] J. E. Baldwin, C. A. Haniff, C. D. Mackay, and P. J. Warner, "Closure phase in high-resolution optical imaging," *Nature*, vol. 320, pp. 595–597, Apr. 1986.

[21] P. G. Tuthill, J. D. Monnier, W. C. Danchi, E. H. Wishnow, and C. A. Haniff, "Michelson Interferometry with the Keck I Telescope," *Publications of the Astronomical Society of the Pacific*, vol. 112, pp. 555–565, Apr. 2000.

[22] A. L. Kraus and M. J. Ireland, "LkCa 15: A Young Exoplanet Caught at Formation?" *Astrophysical Journal*, vol. 745, p. 5, Jan. 2012.

[23] S. Sallum, K. B. Follette, J. A. Eisner, L. M. Close, P. Hinz, K. Kratter, J. Males, A. Skemer, B. Macintosh, P. Tuthill, V. Bailey, D. Defrère, K. Morzinski, T. Rodigas, E. Spalding, A. Vaz, and A. J. Weinberger, "Accreting protoplanets in the LkCa 15 transition disk," *Nature*, vol. 527, pp. 342–344, Nov. 2015.

[24] N. Huélamo, S. Lacour, P. Tuthill, M. Ireland, A. Kraus, and G. Chauvin, "A companion candidate in the gap of the T Chamaeleontis transitional disk," *Astronomy & Astrophysics*, vol. 528, p. L7, Apr. 2011.

[25] S. Sallum, J. A. Eisner, L. M. Close, P. M. Hinz, A. J. Skemer, V. Bailey, R. Briguglio, K. B. Follette, J. R. Males, K. M. Morzinski, A. Puglisi, T. J. Rodigas, A. J. Weinberger, and M. Xompero, "New Spatially Resolved Observations of the T Cha Transition Disk and Constraints on the Previously Claimed Substellar Companion," *Astrophysical Journal*, vol. 801, p. 85, Mar. 2015.

[26] A. Cheetham, N. Huélamo, S. Lacour, I. de Gregorio-Monsalvo, and P. Tuthill, "Near-IR imaging of T Cha: evidence for scattered-light disc structures at Solar system scales," *Monthly Notices of the Royal Astronomical Society*, vol. 450, pp. L1–L5, Jun. 2015.

[27] J. P. Lloyd, F. Martinache, M. J. Ireland, J. D. Monnier, S. H. Pravdo, S. B. Shaklan, and P. G. Tuthill, "Direct Detection of the Brown Dwarf GJ 802B with Adaptive Optics Masking Interferometry," *Astrophysical Journal Leters*, vol. 650, pp. L131–L134, Oct. 2006.

[28] A. L. Kraus, M. J. Ireland, F. Martinache, and J. P. Lloyd, "Mapping the Shores of the Brown Dwarf Desert. I. Upper Scorpius," *Astrophysical Journal*, vol. 679, pp. 762–782, May 2008.

[29] A. L. Kraus, M. J. Ireland, F. Martinache, and L. A. Hillenbrand, "Mapping the Shores of the Brown Dwarf Desert. II. Multiple Star Formation in Taurus-Auriga," *Astrophysical Journal*, vol. 731, p. 8, Apr. 2011.

[30] T. M. Evans, M. J. Ireland, A. L. Kraus, F. Martinache, P. Stewart, P. G. Tuthill, S. Lacour, J. M. Carpenter, and L. A. Hillenbrand, "Mapping the Shores of the Brown Dwarf Desert. III. Young Moving Groups," *Astrophysical Journal*, vol. 744, p. 120, Jan. 2012.

[31] A. C. Cheetham, A. L. Kraus, M. J. Ireland, L. Cieza, A. C. Rizzuto, and P. G.

Tuthill, "Mapping the Shores of the Brown Dwarf Desert. IV. Ophiuchus," *Astrophysical Journal*, vol. 813, p. 83, Nov. 2015.

[32] S. Hinkley, A. L. Kraus, M. J. Ireland, A. Cheetham, J. M. Carpenter, P. Tuthill, S. Lacour, T. M. Evans, and X. Haubois, "Discovery of Seven Companions to Intermediate-mass Stars with Extreme Mass Ratios in the Scorpius-Centaurus Association," *Astrophysical Journal Leters*, vol. 806, p. L9, Jun. 2015.

[33] A. Z. Greenbaum, L. Pueyo, A. Sivaramakrishnan, and S. Lacour, "An Image-plane Algorithm for JWST's Non-redundant Aperture Mask Data," *Atrophysical Journal*, vol. 798, p. 68, Jan. 2015.

[34] Z. Wahhaj, M. C. Liu, E. L. Nielsen, B. A. Biller, T. L. Hayward, L. M. Close, J. R. Males, A. Skemer, C. Ftaclas, M. Chun, N. Thatte, M. Tecza, E. L. Shkolnik, M. Kuchner, I. N. Reid, E. M. de Gouveia Dal Pino, S. H. P. Alencar, J. Gregorio-Hetem, A. Boss, D. N. C. Lin, and D. W. Toomey, "The Gemini Planet-finding Campaign: The Frequency Of Giant Planets around Debris Disk Stars," *Astrophysical Journal*, vol. 773, p. 179, Aug. 2013.

[35] E. L. Nielsen, M. C. Liu, Z. Wahhaj, B. A. Biller, T. L. Hayward, L. M. Close, J. R. Males, A. J. Skemer, M. Chun, C. Ftaclas, S. H. P. Alencar, P. Artymowicz, A. Boss, F. Clarke, E. de Gouveia Dal Pino, J. Gregorio-Hetem, M. Hartung, S. Ida, M. Kuchner, D. N. C. Lin, I. N. Reid, E. L. Shkolnik, M. Tecza, N. Thatte, and D. W. Toomey, "The Gemini NICI Planet-Finding Campaign:

The Frequency of Giant Planets around Young B and A Stars," *Astrophysical Journal*, vol. 776, p. 4, Oct. 2013.

[36] B. A. Biller, M. C. Liu, Z. Wahhaj, E. L. Nielsen, T. L. Hayward, J. R. Males, A. Skemer, L. M. Close, M. Chun, C. Ftaclas, F. Clarke, N. Thatte, E. L. Shkolnik, I. N. Reid, M. Hartung, A. Boss, D. Lin, S. H. P. Alencar, E. de Gouveia Dal Pino, J. Gregorio-Hetem, and D. Toomey, "The Gemini/NICI Planet-Finding Campaign: The Frequency of Planets around Young Moving Group Stars," *Astrophysical Journal*, vol. 777, p. 160, Nov. 2013.

[37] A. Vigan, J. Patience, C. Marois, M. Bonavita, R. J. De Rosa, B. Macintosh, I. Song, R. Doyon, B. Zuckerman, D. Lafrenière, and T. Barman, "The International Deep Planet Survey. I. The frequency of wide-orbit massive planets around A-stars," *Astronomy Astrophysics*, vol. 544, p. A9, Aug. 2012.

[38] B. R. Oppenheimer, C. Beichman, D. Brenner, R. Burruss, E. Cady, J. Crepp, L. Hillenbrand, S. Hinkley, E. R. Ligon, T. Lockhart, I. Parry, L. Pueyo, E. Rice, L. C. Roberts, J. Roberts, M. Shao, A. Sivaramakrishnan, R. Soummer, G. Vasisht, F. Vescelus, J. K. Wallace, C. Zhai, and N. Zimmerman, "Project 1640: the world's first ExAO coronagraphic hyperspectral imager for comparative planetary science," in *Society of Photo-Optical Instrumentation Engineers (SPIE) Conference Series*, vol. 8447, Jul. 2012.

[39] B. A. Macintosh, A. Anthony, J. Atwood, N. Barriga, B. Bauman, K. Ca-

puta, J. Chilcote, D. Dillon, R. Doyon, J. Dunn, D. T. Gavel, R. Galvez, S. J. Goodsell, J. R. Graham, M. Hartung, J. Isaacs, D. Kerley, Q. Konopacky, K. Labrie, J. E. Larkin, J. Maire, C. Marois, M. Millar-Blanchaer, A. Nunez, B. R. Oppenheimer, D. W. Palmer, J. Pazder, M. Perrin, L. A. Poyneer, C. Quirez, F. Rantakyro, V. Reshtov, L. Saddlemyer, N. Sadakuni, D. Savransky, A. Sivaramakrishnan, M. Smith, R. Soummer, S. Thomas, J. K. Wallace, J. Weiss, and S. Wiktorowicz, "The Gemini Planet Imager: integration and status," in *Society of Photo-Optical Instrumentation Engineers (SPIE) Conference Series*, vol. 8446, Sep. 2012.

[40] J.-L. Beuzit, M. Feldt, D. Mouillet, K. Dohlen, P. Puget, F. Wildi, and SPHERE Consortium, "SPHERE: a planet imager for the VLT," in *In the Spirit of Lyot 2010*, Oct. 2010.

[41] F. Martinache and O. Guyon, "The Subaru Coronagraphic Extreme-AO Project," in *Society of Photo-Optical Instrumentation Engineers (SPIE) Conference Series*, ser. Society of Photo-Optical Instrumentation Engineers (SPIE) Conference Series, vol. 7440, Aug. 2009, p. 0.

[42] S. Lacour, P. Tuthill, P. Amico, M. Ireland, D. Ehrenreich, N. Huelamo, and A.-M. Lagrange, "Sparse aperture masking at the VLT. I. Faint companion detection limits for the two debris disk stars HD 92945 and HD 141569," *Astronomy Astrophysics*, vol. 532, p. A72, Aug. 2011.

[43] L. A. Cieza, S. Lacour, M. R. Schreiber, S. Casassus, A. Jordán, G. S. Mathews, H. Cánovas, F. Ménard, A. L. Kraus, S. Pérez, P. Tuthill, and M. J. Ireland, "Sparse Aperture Masking Observations of the FL Cha Pre-transitional Disk," *Astrophysical Journal Leters*, vol. 762, p. L12, Jan. 2013.

[44] C. A. Haniff, C. D. Mackay, D. J. Titterington, D. Sivia, and J. E. Baldwin, "The first images from optical aperture synthesis," *Nature*, vol. 328, pp. 694–696, Aug. 1987.

[45] M. J. Ireland, A. Kraus, F. Martinache, J. P. Lloyd, and P. G. Tuthill, "Dynamical Mass of GJ 802B: A Brown Dwarf in a Triple System," *Astrophysical Journal*, vol. 678, pp. 463–471, May 2008.

[46] D. Bernat, A. H. Bouchez, M. Ireland, P. Tuthill, F. Martinache, J. Angione, R. S. Burruss, J. L. Cromer, R. G. Dekany, S. R. Guiwits, J. R. Henning, J. Hickey, E. Kibblewhite, D. L. McKenna, A. M. Moore, H. L. Petrie, J. Roberts, J. C. Shelton, R. P. Thicksten, T. Trinh, R. Tripathi, M. Troy, T. Truong, V. Velur, and J. P. Lloyd, "A Close Companion Search Around L Dwarfs Using Aperture Masking Interferometry and Palomar Laser Guide Star Adaptive Optics," *Astrophysical Journal*, vol. 715, pp. 724–735, Jun. 2010.

[47] F. Martinache, B. Rojas-Ayala, M. J. Ireland, J. P. Lloyd, and P. G. Tuthill, "Visual Orbit of the Low-Mass Binary GJ 164 AB," *Astrophysical Journal*, vol. 695, pp. 1183–1190, Apr. 2009.

[48] F. Martinache, J. P. Lloyd, M. J. Ireland, R. S. Yamada, and P. G. Tuthill, "Precision Masses of the Low-Mass Binary System GJ 623," *Astrophysical Journal*, vol. 661, pp. 496–501, May 2007.

[49] S. Hinkley, J. M. Carpenter, M. J. Ireland, and A. L. Kraus, "Observational Constraints on Companions Inside of 10 AU in the HR 8799 Planetary System," *Astrophysical Journal Leters*, vol. 730, p. L21, Apr. 2011.

[50] A. Sivaramakrishnan, R. Soummer, B. R. Oppenheimer, G. L. Carr, J. L. Mey, D. Brenner, C. W. Mandeville, N. Zimmerman, B. A. Macintosh, J. R. Graham, L. Saddlemyer, B. Bauman, A. Carlotti, L. Pueyo, P. G. Tuthill, C. Dorrer, R. Roberts, and A. Greenbaum, "Gemini Planet Imager coronagraph testbed results," in *Society of Photo-Optical Instrumentation Engineers (SPIE) Conference Series*, vol. 7735, Jul. 2010.

[51] N. T. Zimmerman, "High-Contrast Observations with an Integral Field Spectrograph," Ph.D. dissertation, Columbia University, 2011.

[52] N. Zimmerman, A. Sivaramakrishnan, D. Bernat, B. R. Oppenheimer, S. Hinkley, J. P. Lloyd, P. G. Tuthill, D. Brenner, I. R. Parry, M. Simon, J. E. Krist, and L. Pueyo, "Aperture mask interferometry with an integral field spectrograph," in *Society of Photo-Optical Instrumentation Engineers (SPIE) Conference Series*, vol. 8445, Jul. 2012.

[53] R. Doyon, J. B. Hutchings, M. Beaulieu, L. Albert, D. Lafrenière, C. Willott,

D. Touahri, N. Rowlands, M. Maszkiewicz, A. W. Fullerton, K. Volk, A. R. Martel, P. Chayer, A. Sivaramakrishnan, R. Abraham, L. Ferrarese, R. Jayawardhana, D. Johnstone, M. Meyer, J. L. Pipher, and M. Sawicki, "The JWST Fine Guidance Sensor (FGS) and Near-Infrared Imager and Slitless Spectrograph (NIRISS)," in *Society of Photo-Optical Instrumentation Engineers (SPIE) Conference Series*, vol. 8442, Sep. 2012.

[54] A. Sivaramakrishnan, D. Lafrenière, K. E. S. Ford, B. McKernan, A. Cheetham, A. Z. Greenbaum, P. G. Tuthill, J. P. Lloyd, M. J. Ireland, R. Doyon, M. Beaulieu, A. Martel, A. Koekemoer, F. Martinache, and P. Teuben, "Non-redundant Aperture Masking Interferometry (AMI) and segment phasing with JWST-NIRISS," in *Society of Photo-Optical Instrumentation Engineers (SPIE) Conference Series*, vol. 8442, Sep. 2012.

[55] A. Z. Greenbaum, S. Sivaramakrishnan, and L. Pueyo, "Flat Field Errors and Intral-Pixel Sensitivities For Non-Redundant Aperture Masking Interferometry on JWST NIRISS," in *Society of Photo-Optical Instrumentation Engineers (SPIE) Conference Series*, vol. 8864, Aug. 2013.

[56] C. A. Beichman, J. Krist, J. T. Trauger, T. Greene, B. Oppenheimer, A. Sivaramakrishnan, R. Doyon, A. Boccaletti, T. S. Barman, and M. Rieke, "Imaging Young Giant Planets From Ground and Space," *Publications of the Astronomical Society of the Pacific*, vol. 122, pp. 162–200, Feb. 2010.

[57] F. Martinache, "Kernel Phase in Fizeau Interferometry," *Astrophysical Journal*, vol. 724, pp. 464–469, Nov. 2010.

[58] M. J. Ireland, "Phase errors in diffraction-limited imaging: contrast limits for sparse aperture masking," *Monthly Notices of the Royal Astronomical Society*, vol. 433, pp. 1718–1728, Aug. 2013.

[59] B. J. Bos, D. A. Kubalak, S. R. Antonille, R. G. Ohl, J. G. Hagopian, P. S. Davila, J. Sullivan, M. Sánchez, D. Sabatke, R. A. Woodruff, M. te Plate, C. Evans, V. Isbrucker, S. Somerstein, M. Wells, and S. Ronayette, "Cryogenic pupil alignment test architecture for the James Webb Space Telescope integrated science instrument module," in *Society of Photo-Optical Instrumentation Engineers (SPIE) Conference Series*, vol. 7010, Aug. 2008.

[60] A. Sivaramakrishnan, D. Lafrenière, P. G. Tuthill, M. J. Ireland, J. P. Lloyd, F. Martinache, R. B. Makidon, R. Soummer, R. Doyon, M. Beaulieu, S. Parmentier, and C. A. Beichman, "Planetary system and star formation science with non-redundant masking on JWST," in *Society of Photo-Optical Instrumentation Engineers (SPIE) Conference Series*, vol. 7731, Jul. 2010.

[61] A. Z. Greenbaum, A. R. Martel, A. Sivaramakrishnan, K. Volk, L. Pueyo, É. Artigau, and P. Tuthill, "Analyzing the first JWST-NIRISS NRM test data," in *Space Telescopes and Instrumentation 2014: Optical, Infrared, and Millimeter*

Wave, ser. Society of Photo-Optical Instrumentation Engineers (SPIE) Conference Series, vol. 9143, Aug. 2014, p. 91434M.

[62] A. C. S. Readhead, T. S. Nakajima, T. J. Pearson, G. Neugebauer, J. B. Oke, and W. L. W. Sargent, "Diffraction-limited imaging with ground-based optical telescopes," *Astronomical Journal*, vol. 95, pp. 1278–1296, Apr. 1988.

[63] F. Martinache, "Kernel-phases for high-contrast detection beyond the resolution limit," in *Society of Photo-Optical Instrumentation Engineers (SPIE) Conference Series*, vol. 8151, Sep. 2011.

[64] B. Pope, F. Martinache, and P. Tuthill, "Dancing in the Dark: New Brown Dwarf Binaries from Kernel Phase Interferometry," *Astrophysical Journal*, vol. 767, p. 110, Apr. 2013.

[65] A. R. Thompson, J. M. Moran, and G. W. Swenson, *Interferometry and synthesis in radio astronomy*, 1986.

[66] K. E. S. Ford, B. McKernan, A. Sivaramakrishnan, A. R. Martel, A. Koekemoer, D. Lafrenière, and S. Parmentier, "Active Galactic Nucleus and Quasar Science with Aperture Masking Interferometry on the James Webb Space Telescope," *Astrophysical Journal*, vol. 783, p. 73, Mar. 2014.

[67] J. D. Monnier, "Optical interferometry in astronomy," *Reports on Progress in Physics*, vol. 66, pp. 789–857, May 2003.

[68] S. A. Metchev and L. A. Hillenbrand, "Initial Results from the Palomar Adaptive Optics Survey of Young Solar-Type Stars: A Brown Dwarf and Three Stellar Companions," *Astrophysical Journal*, vol. 617, pp. 1330–1346, Dec. 2004.

[69] M. J. Ireland, A. Kraus, F. Martinache, N. Law, and L. A. Hillenbrand, "Two Wide Planetary-mass Companions to Solar-type Stars in Upper Scorpius," *Astrophysical Journal*, vol. 726, p. 113, Jan. 2011.

[70] J. Girard, *NACO User Manual*, European Southern Observatory, 2013, VLT-MAN-ESO-14200-2761.

[71] A. C. Cheetham, P. G. Tuthill, A. Sivaramakrishnan, and J. P. Lloyd, "Fizeau interferometric cophasing of segmented mirrors," *Opt. Express*, vol. 20, no. 28, pp. 29 457–29 471, Dec 2012. [Online]. Available: http://www.opticsexpress.org/abstract.cfm?URI=oe-20-28-29457

[72] A. Sivaramakrishnan, P. G. Tuthill, M. J. Ireland, J. P. Lloyd, F. Martinache, R. Soummer, R. B. Makidon, R. Doyon, M. Beaulieu, and C. A. Beichman, "Planetary system and star formation science with non-redundant masking on JWST," in *Society of Photo-Optical Instrumentation Engineers (SPIE) Conference Series*, vol. 7440, Aug. 2009.

[73] A. Sivaramakrishnan, P. Tuthill, F. Martinache, M. Ireland, J. P. Lloyd, M. D. Perrin, R. Soummer, B. McKernan, and S. Ford, "Planetary system, star formation, and black hole science with non-redundant masking on space telescopes,"

in *astro2010: The Astronomy and Astrophysics Decadal Survey*, ser. ArXiv Astrophysics e-prints, vol. 2010, 2009, p. 40.

[74] T. Hardy, M. R. Baril, J. Pazder, and J. S. Stilburn, "Intra-pixel response of infrared detector arrays for JWST," in *Society of Photo-Optical Instrumentation Engineers (SPIE) Conference Series*, vol. 7021, Aug. 2008.

[75] E. Sabatke, J. Burge, and D. Sabatke, "Analytic diffraction analysis of a 32-m telescope with hexagonal segments for high-contrast imaging," *Applied Optics*, vol. 44, pp. 1360–1365, Mar. 2005.

[76] M. Troy and G. Chanan, "Diffraction effects from giant segmented-mirror telescopes," *Applied Optics*, vol. 42, pp. 3745–3753, Jul. 2003.

[77] M. R. Teague, "Irradiance moments - Their propagation and use for unique retrieval of phase," *Journal of the Optical Society of America (1917-1983)*, vol. 72, pp. 1199–1209, Sep. 1982.

[78] T. R. Lauer, "The Photometry of Undersampled Point-Spread Functions," *Publications of the Astronomical Society of the Pacific*, vol. 111, pp. 1434–1443, Nov. 1999.

[79] A. M. Koekemoer and K. Lindsay, "An investigation of optimal dither strategies for JWST (JWST-STScI-000674 SM-12)." Baltimore: STScI, 2005.

[80] M. C. Cushing, T. L. Roellig, M. S. Marley, D. Saumon, S. K. Leggett, J. D.

Kirkpatrick, J. C. Wilson, G. C. Sloan, A. K. Mainzer, J. E. Van Cleve, and J. R. Houck, "A Spitzer Infrared Spectrograph Spectral Sequence of M, L, and T Dwarfs," *Astrophysical Journal*, vol. 648, pp. 614–628, Sep. 2006.

[81] D. C. Stephens, S. K. Leggett, M. C. Cushing, M. S. Marley, D. Saumon, T. R. Geballe, D. A. Golimowski, X. Fan, and K. S. Noll, "The 0.8-14.5 μm Spectra of Mid-L to Mid-T Dwarfs: Diagnostics of Effective Temperature, Grain Sedimentation, Gas Transport, and Surface Gravity," *Astrophysical Journal*, vol. 702, pp. 154–170, Sep. 2009.

[82] T. Currie, A. Burrows, N. Madhusudhan, M. Fukagawa, J. H. Girard, R. Dawson, R. Murray-Clay, S. Kenyon, M. Kuchner, S. Matsumura, R. Jayawardhana, J. Chambers, and B. Bromley, "A Combined VLT and Gemini Study of the Atmosphere of the Directly-Imaged Planet, beta Pictoris b," *ArXiv e-prints*, Jun. 2013.

[83] F. Castelli and R. L. Kurucz, "Computed Hbeta indices from ATLAS9 model (Castelli+, 2006)," *VizieR Online Data Catalog*, vol. 345, p. 40333, May 2006.

[84] M. D. Perrin, R. Soummer, E. M. Elliott, M. D. Lallo, and A. Sivaramakrishnan, "Simulating point spread functions for the James Webb Space Telescope with WebbPSF," in *Society of Photo-Optical Instrumentation Engineers (SPIE) Conference Series*, vol. 8442, Sep. 2012.

[85] J. S. Knight, D. S. Acton, P. Lightsey, and A. Barto, "Integrated telescope

model for the James Webb Space Telescope," in *Society of Photo-Optical Instrumentation Engineers (SPIE) Conference Series*, vol. 8449, Sep. 2012.

[86] P. A. Lightsey, A. A. Barto, and J. Contreras, "Optical performance for the James Webb Space Telescope," in *Optical, Infrared, and Millimeter Space Telescopes*, ser. Society of Photo-Optical Instrumentation Engineers (SPIE) Conference Series, J. C. Mather, Ed., vol. 5487, Oct. 2004, pp. 825–832.

[87] J. P. Gardner, J. C. Mather, M. Clampin, R. Doyon, M. A. Greenhouse, H. B. Hammel, J. B. Hutchings, P. Jakobsen, S. J. Lilly, K. S. Long, J. I. Lunine, M. J. McCaughrean, M. Mountain, J. Nella, G. H. Rieke, M. J. Rieke, H.-W. Rix, E. P. Smith, G. Sonneborn, M. Stiavelli, H. S. Stockman, R. A. Windhorst, and G. S. Wright, "The James Webb Space Telescope," *Space Science Reviews*, vol. 123, pp. 485–606, Apr. 2006.

[88] R. B. Makidon, A. Sivaramakrishnan, R. Soummer, J. Anderson, and R. P. van der Marel, "Towards observing extrasolar giant-planet environments with JWST," in *Society of Photo-Optical Instrumentation Engineers (SPIE) Conference Series*, vol. 7010, Aug. 2008.

[89] A. Sivaramakrishnan, R. Soummer, B. R. Oppenheimer, G. L. Carr, J. L. Mey, D. Brenner, C. W. Mandeville, N. Zimmerman, B. A. Macintosh, J. R. Graham, L. Saddlemyer, B. Bauman, A. Carlotti, L. Pueyo, P. G. Tuthill, C. Dorrer, R. Roberts, and A. Greenbaum, "Gemini Planet Imager coronagraph testbed

results," in *Ground-based and Airborne Instrumentation for Astronomy III*, ser. Society of Photo-Optical Instrumentation Engineers (SPIE) Conference Series, vol. 7735, Jul. 2010, p. 773586.

[90] J. E. Larkin, J. K. Chilcote, T. Aliado, B. J. Bauman, G. Brims, J. M. Canfield, A. Cardwell, D. Dillon, R. Doyon, J. Dunn, M. P. Fitzgerald, J. R. Graham, S. Goodsell, M. Hartung, P. Hibon, P. Ingraham, C. A. Johnson, E. Kress, Q. M. Konopacky, B. A. Macintosh, K. G. Magnone, J. Maire, I. S. McLean, D. Palmer, M. D. Perrin, C. Quiroz, F. Rantakyrö, N. Sadakuni, L. Saddlemyer, A. Serio, S. Thibault, S. J. Thomas, P. Vallee, and J. L. Weiss, "The integral field spectrograph for the Gemini planet imager," in *Ground-based and Airborne Instrumentation for Astronomy V*, ser. Society of Photo-Optical Instrumentation Engineers (SPIE) Conference Series, vol. 9147, Jul. 2014, p. 91471K.

[91] C. Pinte, F. Ménard, G. Duchêne, and P. Bastien, "Monte Carlo radiative transfer in protoplanetary disks," *Astronomy Astrophysics*, vol. 459, pp. 797–804, Dec. 2006.

[92] T. P. Robitaille, "HYPERION: an open-source parallelized three-dimensional dust continuum radiative transfer code," *Astronomy Astrophysics*, vol. 536, p. A79, Dec. 2011.

[93] T. Robitaille, "Hyperion: Parallelized 3D Dust Continuum Radiative Transfer Code," Astrophysics Source Code Library, Jul. 2012.

[94] Lenox Laser (Glen Arm, MD).

[95] A. Z. Greenbaum, A. Sivaramakrishnan, L. Pueyo, P. Ingraham, S. Thomas, S. Wolff, M. D. Perrin, B. Norris, and P. G. Tuthill, "Wavelength calibration and closure phases with the Gemini Planet Imager IFS using its non-redundant mask," in *Techniques and Instrumentation for Detection of Exoplanets VI*, ser. Society of Photo-Optical Instrumentation Engineers (SPIE) Conference Series, vol. 8864, Sep. 2013, p. 88641V.

[96] B. R. M. Norris, P. G. Tuthill, M. J. Ireland, S. Lacour, A. A. Zijlstra, F. Lykou, T. M. Evans, P. Stewart, and T. R. Bedding, "A close halo of large transparent grains around extreme red giant stars," *Nature*, vol. 484, pp. 220–222, Apr. 2012.

[97] P. R. Lawson, Ed., *Principles of Long Baseline Stellar Interferometry*, 2000.

[98] D. Foreman-Mackey, D. W. Hogg, D. Lang, and J. Goodman, "emcee: The MCMC Hammer," *Publications of the Astronomical Society of the Pacific*, vol. 125, pp. 306–312, Mar. 2013.

[99] D. Foreman-Mackey, A. Conley, W. Meierjurgen Farr, D. W. Hogg, D. Long, P. Marshall, A. Price-Whelan, J. Sanders, and J. Zuntz, "emcee: The MCMC Hammer," Astrophysics Source Code Library, Mar. 2013.

[100] L. Gauchet, S. Lacour, A.-M. Lagrange, D. Ehrenreich, M. Bonnefoy, J. H.

Girard, and A. Boccaletti, "Sparse aperture masking at the VLT II. Detection limits for the eight debris disks stars β Pic, AU Mic, 49 Cet, η Tel, Fomalhaut, g Lup, HD181327 and HR8799," *ArXiv e-prints*, Jun. 2016.

[101] I. Baraffe, D. Homeier, F. Allard, and G. Chabrier, "New evolutionary models for pre-main sequence and main sequence low-mass stars down to the hydrogen-burning limit," *Astronomy Astrophysics*, vol. 577, p. A42, May 2015.

[102] M. J. Pecaut, E. E. Mamajek, and E. J. Bubar, "A Revised Age for Upper Scorpius and the Star Formation History among the F-type Members of the Scorpius-Centaurus OB Association," *Astrophysical Journal*, vol. 746, p. 154, Feb. 2012.

[103] A. P. Verhoeff, M. Min, E. Pantin, L. B. F. M. Waters, A. G. G. M. Tielens, M. Honda, H. Fujiwara, J. Bouwman, R. van Boekel, S. M. Dougherty, A. de Koter, C. Dominik, and G. D. Mulders, "The complex circumstellar environment of HD 142527," *Astronomy Astrophysics*, vol. 528, p. A91, Apr. 2011.

[104] B. Biller, S. Lacour, A. Juhász, M. Benisty, G. Chauvin, J. Olofsson, J.-U. Pott, A. Müller, A. Sicilia-Aguilar, M. Bonnefoy, P. Tuthill, P. Thebault, T. Henning, and A. Crida, "A Likely Close-in Low-mass Stellar Companion to the Transitional Disk Star HD 142527," *Astrophysical Journal Leters*, vol. 753, p. L38, Jul. 2012.

[105] L. M. Close, K. B. Follette, J. R. Males, A. Puglisi, M. Xompero, D. Apai,

J. Najita, A. J. Weinberger, K. Morzinski, T. J. Rodigas, P. Hinz, V. Bailey, and R. Briguglio, "Discovery of Hα Emission from the Close Companion inside the Gap of Transitional Disk HD 142527," *Astrophysical Journal Leters*, vol. 781, p. L30, Feb. 2014.

[106] S. Lacour, B. Biller, A. Cheetham, A. Greenbaum, T. Pearce, S. Marino, P. Tuthill, L. Pueyo, E. E. Mamajek, J. H. Girard, A. Sivaramakrishnan, M. Bonnefoy, I. Baraffe, G. Chauvin, J. Olofsson, A. Juhasz, M. Benisty, J.-U. Pott, A. Sicilia-Aguilar, T. Henning, A. Cardwell, S. Goodsell, J. R. Graham, P. Hibon, P. Ingraham, Q. Konopacky, B. Macintosh, R. Oppenheimer, M. Perrin, F. Rantakyrö, N. Sadakuni, and S. Thomas, "An M-dwarf star in the transition disk of Herbig HD 142527. Physical parameters and orbital elements," *Astronomy Astrophysics*, vol. 590, p. A90, May 2016.

[107] A. Crida, A. Morbidelli, and F. Masset, "On the width and shape of gaps in protoplanetary disks," *Icarus*, vol. 181, pp. 587–604, Apr. 2006.

[108] J. C. B. Papaloizou, R. P. Nelson, W. Kley, F. S. Masset, and P. Artymowicz, "Disk-Planet Interactions During Planet Formation," *Protostars and Planets V*, pp. 655–668, 2007.

[109] S. E. Dodson-Robinson and C. Salyk, "Transitional Disks as Signposts of Young, Multiplanet Systems," *Astrophysical Journal*, vol. 738, p. 131, Sep. 2011.

[110] W. Kley and R. P. Nelson, "Planet-Disk Interaction and Orbital Evolution," *Annual Review of Astronomy and Astrophysics*, vol. 50, pp. 211–249, Sep. 2012.

[111] T. J. Rodigas, K. B. Follette, A. Weinberger, L. Close, and D. C. Hines, "Polarized Light Imaging of the HD 142527 Transition Disk with the Gemini Planet Imager: Dust around the Close-in Companion," *Astrophysical Journal Leters*, vol. 791, p. L37, Aug. 2014.

[112] S. Marino, S. Perez, and S. Casassus, "Shadows Cast by a Warp in the HD 142527 Protoplanetary Disk," *Astrophysical Journal Leters*, vol. 798, p. L44, Jan. 2015.

[113] S. Casassus, S. Marino, S. Pérez, P. Roman, A. Dunhill, P. J. Armitage, J. Cuadra, A. Wootten, G. van der Plas, L. Cieza, V. Moral, V. Christiaens, and M. Montesinos, "Accretion Kinematics through the Warped Transition Disk in HD142527 from Resolved CO(6-5) Observations," *Astrophysical Journal*, vol. 811, p. 92, Oct. 2015.

[114] L. Pueyo, "Detection and Characterization of Exoplanets using Projections on Karhunen Loeve Eigenimages: Forward Modeling," *Astrophysical Journal*, vol. 824, p. 117, Jun. 2016.

[115] R. Soummer, L. Pueyo, and J. Larkin, "Detection and Characterization of Exoplanets and Disks Using Projections on Karhunen-Loève Eigenimages," *Astrophysical Journal Leters*, vol. 755, p. L28, Aug. 2012.

[116] É. Choquet, L. Pueyo, J. B. Hagan, E. Gofas-Salas, A. Rajan, C. Chen, M. D. Perrin, J. Debes, D. Golimowski, D. C. Hines, M. N'Diaye, G. Schneider, D. Mawet, C. Marois, and R. Soummer, "Archival legacy investigations of circumstellar environments: overview and first results," in *Space Telescopes and Instrumentation 2014: Optical, Infrared, and Millimeter Wave*, ser. Society of Photo-Optical Instrumentation Engineers (SPIE) Conference Series, vol. 9143, Aug. 2014, p. 914357.

[117] R. Soummer, M. D. Perrin, L. Pueyo, É. Choquet, C. Chen, D. A. Golimowski, J. Brendan Hagan, T. Mittal, M. Moerchen, M. N'Diaye, A. Rajan, S. Wolff, J. Debes, D. C. Hines, and G. Schneider, "Five Debris Disks Newly Revealed in Scattered Light from the Hubble Space Telescope NICMOS Archive," *Astrophysical Journal Leters*, vol. 786, p. L23, May 2014.

[118] J. J. Wang, J.-B. Ruffio, R. J. De Rosa, J. Aguilar, S. G. Wolff, and L. Pueyo, "pyKLIP: PSF Subtraction for Exoplanets and Disks," Astrophysics Source Code Library, Jun. 2015.

[119] C. Marois, B. Macintosh, T. Barman, B. Zuckerman, I. Song, J. Patience, D. Lafrenière, and R. Doyon, "Direct Imaging of Multiple Planets Orbiting the Star HR 8799," *Science*, vol. 322, p. 1348, Nov. 2008.

[120] C. Marois, B. Zuckerman, Q. M. Konopacky, B. Macintosh, and T. Barman,

"Images of a fourth planet orbiting HR 8799," *Nature*, vol. 468, pp. 1080–1083, Dec. 2010.

[121] Q. M. Konopacky, C. Marois, B. A. Macintosh, R. Galicher, T. S. Barman, S. A. Metchev, and B. Zuckerman, "Astrometric Monitoring of the HR 8799 Planets: Orbit Constraints from Self-consistent Measurements," *Astronomical Journal*, vol. 152, p. 28, Aug. 2016.

[122] L. Pueyo, R. Soummer, J. Hoffmann, R. Oppenheimer, J. R. Graham, N. Zimmerman, C. Zhai, J. K. Wallace, F. Vescelus, A. Veicht, G. Vasisht, T. Truong, A. Sivaramakrishnan, M. Shao, L. C. Roberts, Jr., J. E. Roberts, E. Rice, I. R. Parry, R. Nilsson, T. Lockhart, E. R. Ligon, D. King, S. Hinkley, L. Hillenbrand, D. Hale, R. Dekany, J. R. Crepp, E. Cady, R. Burruss, D. Brenner, C. Beichman, and C. Baranec, "Reconnaissance of the HR 8799 Exosolar System. II. Astrometry and Orbital Motion," *Astrophysical Journal*, vol. 803, p. 31, Apr. 2015.

[123] R. Soummer, J. Brendan Hagan, L. Pueyo, A. Thormann, A. Rajan, and C. Marois, "Orbital Motion of HR 8799 b, c, d Using Hubble Space Telescope Data from 1998: Constraints on Inclination, Eccentricity, and Stability," *Astrophysical Journal*, vol. 741, p. 55, Nov. 2011.

[124] M. Bonnefoy, A. Zurlo, J. L. Baudino, P. Lucas, D. Mesa, A.-L. Maire, A. Vigan, R. Galicher, D. Homeier, F. Marocco, R. Gratton, G. Chauvin, F. Allard,

S. Desidera, M. Kasper, C. Moutou, A.-M. Lagrange, J. Antichi, A. Baruffolo, J. Baudrand, J.-L. Beuzit, A. Boccaletti, F. Cantalloube, M. Carbillet, J. Charton, R. U. Claudi, A. Costille, K. Dohlen, C. Dominik, D. Fantinel, P. Feautrier, M. Feldt, T. Fusco, P. Gigan, J. H. Girard, L. Gluck, C. Gry, T. Henning, M. Janson, M. Langlois, F. Madec, Y. Magnard, D. Maurel, D. Mawet, M. R. Meyer, J. Milli, O. Moeller-Nilsson, D. Mouillet, A. Pavlov, D. Perret, P. Pujet, S. P. Quanz, S. Rochat, G. Rousset, A. Roux, B. Salasnich, G. Salter, J.-F. Sauvage, H. M. Schmid, A. Sevin, C. Soenke, E. Stadler, M. Turatto, S. Udry, F. Vakili, Z. Wahhaj, and F. Wildi, "First light of the VLT planet finder SPHERE. IV. Physical and chemical properties of the planets around HR8799," *Astronomy Astrophysics*, vol. 587, p. A58, Mar. 2016.

[125] A. Zurlo, A. Vigan, R. Galicher, A.-L. Maire, D. Mesa, R. Gratton, G. Chauvin, M. Kasper, C. Moutou, M. Bonnefoy, S. Desidera, L. Abe, D. Apai, A. Baruffolo, P. Baudoz, J. Baudrand, J.-L. Beuzit, P. Blancard, A. Boccaletti, F. Cantalloube, M. Carle, E. Cascone, J. Charton, R. U. Claudi, A. Costille, V. de Caprio, K. Dohlen, C. Dominik, D. Fantinel, P. Feautrier, M. Feldt, T. Fusco, P. Gigan, J. H. Girard, D. Gisler, L. Gluck, C. Gry, T. Henning, E. Hugot, M. Janson, M. Jaquet, A.-M. Lagrange, M. Langlois, M. Llored, F. Madec, Y. Magnard, P. Martinez, D. Maurel, D. Mawet, M. R. Meyer, J. Milli, O. Moeller-Nilsson, D. Mouillet, A. Origné, A. Pavlov, C. Petit, P. Puget, S. P. Quanz, P. Rabou, J. Ramos, G. Rousset, A. Roux, B. Salasnich, G. Salter, J.-F.

Sauvage, H. M. Schmid, C. Soenke, E. Stadler, M. Suarez, M. Turatto, S. Udry, F. Vakili, Z. Wahhaj, F. Wildi, and J. Antichi, "First light of the VLT planet finder SPHERE. III. New spectrophotometry and astrometry of the HR 8799 exoplanetary system," *Astronomy Astrophysics*, vol. 587, p. A57, Mar. 2016.

[126] A. Rajan, T. Barman, R. Soummer, J. Brendan Hagan, J. Patience, L. Pueyo, É. Choquet, Q. Konopacky, B. Macintosh, and C. Marois, "Characterizing the Atmospheres of the HR8799 Planets with HST/WFC3," *Astrophysical Journal Leters*, vol. 809, p. L33, Aug. 2015.

[127] T. S. Barman, Q. M. Konopacky, B. Macintosh, and C. Marois, "Simultaneous Detection of Water, Methane, and Carbon Monoxide in the Atmosphere of Exoplanet HR8799b," *Astrophysical Journal*, vol. 804, p. 61, May 2015.

[128] T. Currie, A. Burrows, J. H. Girard, R. Cloutier, M. Fukagawa, S. Sorahana, M. Kuchner, S. J. Kenyon, N. Madhusudhan, Y. Itoh, R. Jayawardhana, S. Matsumura, and T.-S. Pyo, "Deep Thermal Infrared Imaging of HR 8799 bcde: New Atmospheric Constraints and Limits on a Fifth Planet," *Astrophysical Journal*, vol. 795, p. 133, Nov. 2014.

[129] M. S. Marley, D. Saumon, M. Cushing, A. S. Ackerman, J. J. Fortney, and R. Freedman, "Masses, Radii, and Cloud Properties of the HR 8799 Planets," *Astrophysical Journal*, vol. 754, p. 135, Aug. 2012.

[130] A. J. Skemer, P. M. Hinz, S. Esposito, A. Burrows, J. Leisenring, M. Skrutskie,

S. Desidera, D. Mesa, C. Arcidiacono, F. Mannucci, T. J. Rodigas, L. Close, D. McCarthy, C. Kulesa, G. Agapito, D. Apai, J. Argomedo, V. Bailey, K. Boutsia, R. Briguglio, G. Brusa, L. Busoni, R. Claudi, J. Eisner, L. Fini, K. B. Follette, P. Garnavich, R. Gratton, J. C. Guerra, J. M. Hill, W. F. Hoffmann, T. Jones, M. Krejny, J. Males, E. Masciadri, M. R. Meyer, D. L. Miller, K. Morzinski, M. Nelson, E. Pinna, A. Puglisi, S. P. Quanz, F. Quiros-Pacheco, A. Riccardi, P. Stefanini, V. Vaitheeswaran, J. C. Wilson, and M. Xompero, "First Light LBT AO Images of HR 8799 bcde at 1.6 and 3.3 μm: New Discrepancies between Young Planets and Old Brown Dwarfs," *Astrophysical Journal*, vol. 753, p. 14, Jul. 2012.

[131] R. Galicher, C. Marois, B. Macintosh, T. Barman, and Q. Konopacky, "M-band Imaging of the HR 8799 Planetary System Using an Innovative LOCI-based Background Subtraction Technique," *Astrophysical Journal Leters*, vol. 739, p. L41, Oct. 2011.

[132] B. P. Bowler, M. C. Liu, T. J. Dupuy, and M. C. Cushing, "Near-infrared Spectroscopy of the Extrasolar Planet HR 8799 b," *Astrophysical Journal*, vol. 723, pp. 850–868, Nov. 2010.

[133] D. Apai, M. Kasper, A. Skemer, J. R. Hanson, A.-M. Lagrange, B. A. Biller, M. Bonnefoy, E. Buenzli, and A. Vigan, "High-cadence, High-contrast Imaging for Exoplanet Mapping: Observations of the HR 8799 Planets with

VLT/SPHERE Satellite-spot-corrected Relative Photometry," *Astrophysical Journal*, vol. 820, p. 40, Mar. 2016.

[134] S. Hinkley, B. R. Oppenheimer, N. Zimmerman, D. Brenner, I. R. Parry, J. R. Crepp, G. Vasisht, E. Ligon, D. King, R. Soummer, A. Sivaramakrishnan, C. Beichman, M. Shao, L. C. Roberts, A. Bouchez, R. Dekany, L. Pueyo, J. E. Roberts, T. Lockhart, C. Zhai, C. Shelton, and R. Burruss, "A New High Contrast Imaging Program at Palomar Observatory," *Publications of the Astronomical Society of the Pacific*, vol. 123, pp. 74–86, Jan. 2011.

[135] B. R. Oppenheimer, C. Beichman, D. Brenner, R. Burruss, E. Cady, J. Crepp, L. Hillenbrand, S. Hinkley, E. R. Ligon, T. Lockhart, I. Parry, L. Pueyo, E. Rice, L. C. Roberts, J. Roberts, M. Shao, A. Sivaramakrishnan, R. Soummer, G. Vasisht, F. Vescelus, J. K. Wallace, C. Zhai, and N. Zimmerman, "Project 1640: the world's first ExAO coronagraphic hyperspectral imager for comparative planetary science," in *Adaptive Optics Systems III*, ser. Society of Photo-Optical Instrumentation Engineers (SPIE) Conference Series, vol. 8447, Jul. 2012, p. 844720.

[136] P. Ingraham, M. S. Marley, D. Saumon, C. Marois, B. Macintosh, T. Barman, B. Bauman, A. Burrows, J. K. Chilcote, R. J. De Rosa, D. Dillon, R. Doyon, J. Dunn, D. Erikson, M. P. Fitzgerald, D. Gavel, S. J. Goodsell, J. R. Graham, M. Hartung, P. Hibon, P. G. Kalas, Q. Konopacky, J. A. Larkin, J. Maire,

F. Marchis, J. McBride, M. Millar-Blanchaer, K. M. Morzinski, A. Norton, R. Oppenheimer, D. W. Palmer, J. Patience, M. D. Perrin, L. A. Poyneer, L. Pueyo, F. Rantakyrö, N. Sadakuni, L. Saddlemyer, D. Savransky, R. Soummer, A. Sivaramakrishnan, I. Song, S. Thomas, J. K. Wallace, S. J. Wiktorowicz, and S. G. Wolff, "Gemini Planet Imager Spectroscopy of the HR 8799 Planets c and d," *Astrophysical Journal Leters*, vol. 794, p. L15, Oct. 2014.

[137] T. S. Barman, B. Macintosh, Q. M. Konopacky, and C. Marois, "Clouds and Chemistry in the Atmosphere of Extrasolar Planet HR8799b," *Astrophysical Journal*, vol. 733, p. 65, May 2011.

[138] Q. M. Konopacky, T. S. Barman, B. A. Macintosh, and C. Marois, "Detection of Carbon Monoxide and Water Absorption Lines in an Exoplanet Atmosphere," *Science*, vol. 339, pp. 1398–1401, Mar. 2013.

[139] C. Marois, C. Correia, R. Galicher, P. Ingraham, B. Macintosh, T. Currie, and R. De Rosa, "GPI PSF subtraction with TLOCI: the next evolution in exoplanet/disk high-contrast imaging," in *Adaptive Optics Systems IV*, ser. Society of Photo-Optical Instrumentation Engineers (SPIE) Conference Series, vol. 9148, Jul. 2014, p. 91480U.

[140] F. Millour, M. Vannier, R. G. Petrov, O. Chesneau, L. Dessart, and P. Stee, "Differential Interferometry with the AMBER/VLTI instrument: Description, performances and illustration," in *EAS Publications Series*, ser. EAS Publica-

tions Series, M. Carbillet, A. Ferrari, and C. Aime, Eds., vol. 22, 2006, pp. 379–388.

[141] E. Tatulli, F. Millour, A. Chelli, G. Duvert, B. Acke, O. Hernandez Utrera, K.-H. Hofmann, S. Kraus, F. Malbet, P. Mège, R. G. Petrov, M. Vannier, G. Zins, P. Antonelli, U. Beckmann, Y. Bresson, M. Dugué, S. Gennari, L. Glück, P. Kern, S. Lagarde, E. Le Coarer, F. Lisi, K. Perraut, P. Puget, F. Rantakyrö, S. Robbe-Dubois, A. Roussel, G. Weigelt, M. Accardo, K. Agabi, E. Altariba, B. Arezki, E. Aristidi, C. Baffa, J. Behrend, T. Blöcker, S. Bonhomme, S. Busoni, F. Cassaing, J.-M. Clausse, J. Colin, C. Connot, A. Delboulbé, A. Domiciano de Souza, T. Driebe, P. Feautrier, D. Ferruzzi, T. Forveille, E. Fossat, R. Foy, D. Fraix-Burnet, A. Gallardo, E. Giani, C. Gil, A. Glentzlin, M. Heiden, M. Heininger, D. Kamm, M. Kiekebusch, D. Le Contel, J.-M. Le Contel, T. Lesourd, B. Lopez, M. Lopez, Y. Magnard, A. Marconi, G. Mars, G. Martinot-Lagarde, P. Mathias, J.-L. Monin, D. Mouillet, D. Mourard, E. Nussbaum, K. Ohnaka, J. Pacheco, C. Perrier, Y. Rabbia, S. Rebattu, F. Reynaud, A. Richichi, A. Robini, M. Sacchettini, D. Schertl, M. Schöller, W. Solscheid, A. Spang, P. Stee, P. Stefanini, M. Tallon, I. Tallon-Bosc, D. Tasso, L. Testi, F. Vakili, O. von der Lühe, J.-C. Valtier, and N. Ventura, "Interferometric data reduction with AMBER/VLTI. Principle, estimators, and illustration," *Astronomy Astrophysics*, vol. 464, pp. 29–42, Mar. 2007.

[142] L. Keszthelyi, W. Grundy, J. Stansberry, A. Sivaramakrishnan, D. Thatte, M. Gudipati, C. Tsang, A. Greenbaum, and C. McGruder, "Observing Outer Planet Satellites (Except Titan) with the James Webb Space Telescope: Science Justification and Observational Requirements," *Publications of the Astronomical Society of the Pacific*, vol. 128, no. 1, p. 018006, Jan. 2016.

[143] A. Z. Greenbaum and A. Sivaramakrishnan, "In-focus wavefront sensing using non-redundant mask-induced pupil diversity," *Optics Express*, vol. 000, Mar. 2016.

[144] R. W. Gerchberg and W. O. Saxton, "A practical algorithm for the determination on phase from image and diffraction plane pictues," *Optik*, vol. 35, no. 2, pp. 237–246, 1972. [Online]. Available: http://stacks.iop.org/0022-3727/6/i=5/a=101

[145] J. R. Fienup and C. C. Wackerman, "Phase-retrieval stagnation problems and solutions," *Journal of the Optical Society of America A*, vol. 3, pp. 1897–1907, Nov. 1986.

[146] D. L. Misell, "A method for the solution of the phase problem in electron microscopy," *Journal of Physics D: Applied Physics*, vol. 6, pp. L6–L9, 1973. [Online]. Available: http://stacks.iop.org/0022-3727/6/i=5/a=101

[147] J. E. Krist and C. J. Burrows, "Phase-retrieval analysis of pre-and post-repair

Hubble Space Telescope images," *Applied Optics*, vol. 34, pp. 4951–4964, Aug. 1995.

[148] J. R. Fienup, "Comparison of phase retrieval algorithms (A)," *Journal of the Optical Society of America*, vol. 71, Dec. 1981.

[149] B. J. Bos, D. A. Kubalak, S. R. Antonille, R. G. Ohl, J. G. Hagopian, P. S. Davila, J. Sullivan, M. Sánchez, D. Sabatke, R. A. Woodruff, M. te Plate, C. Evans, V. Isbrucker, S. Somerstein, M. Wells, and S. Ronayette, "Cryogenic pupil alignment test architecture for the James Webb Space Telescope integrated science instrument module," *Society of Photo-Optical Instrumentation Engineers (SPIE) Conference Series*, vol. 7010, p. 70103C, Jul. 2008.

[150] D. S. Acton, T. Towell, J. Schwenker, J. Swensen, D. Shields, E. Sabatke, L. Klingemann, A. R. Contos, B. Bauer, K. Hansen, P. D. Atcheson, D. Redding, F. Shi, S. Basinger, B. Dean, and L. Burns, "Demonstration of the James Webb Space Telescope commissioning on the JWST testbed telescope," *Society of Photo-Optical Instrumentation Engineers (SPIE) Conference Series*, vol. 6265, p. 62650R, Jun. 2006.

[151] A. Sivaramakrishnan, P. G. Tuthill, M. J. Ireland, J. P. Lloyd, F. Martinache, R. Soummer, R. B. Makidon, R. Doyon, M. Beaulieu, and C. A. Beichman, "Planetary system and star formation science with non-redundant masking on

JWST," *Society of Photo-Optical Instrumentation Engineers (SPIE) Conference Series*, vol. 7440, p. 74400Y, Aug. 2009.

[152] A. Sivaramakrishnan, R. Soummer, L. Pueyo, J. K. Wallace, and M. Shao, "Sensing phase aberrations behind Lyot coronagraphs," *Astrophysical Journal*, vol. 688, pp. 701–708, Nov. 2008.

[153] A. C. Cheetham, P. G. Tuthill, A. Sivaramakrishnan, and J. P. Lloyd, "Fizeau interferometric cophasing of segmented mirrors," *Optics Express*, vol. 20, p. 29457, Dec. 2012.

[154] A. Cheetham, N. Cvetojevic, B. Norris, A. Sivaramakrishnan, and P. Tuthill, "Fizeau interferometric cophasing of segmented mirrors: experimental validation," *Optics Express*, vol. 22, p. 12924, Jun. 2014.

[155] R. J. Noll, "Zernike polynomials and atmospheric turbulence," *Journal of the Optical Society of America*, vol. 66, pp. 207–211, Mar. 1976.

[156] R. Upton and B. Ellerbroek, "Gram-Schmidt orthogonalization of the Zernike polynomials on apertures of arbitrary shape," *Optics Letters*, vol. 29, pp. 2840–2842, Dec. 2004.

[157] J. R. Fienup, "Phase retrieval for undersampled broadband images," *Journal of the Optical Society of America A*, vol. 16, pp. 1831–1837, Jul. 1999.

[158] M. D. Perrin, A. Sivaramakrishnan, R. B. Makidon, B. R. Oppenheimer, and

J. R. Graham, "The Structure of High Strehl Ratio Point-Spread Functions," *Astrophysical Journal*, vol. 596, pp. 702–712, Oct. 2003.

[159] F. Martinache, "The asymmetric pupil fourier wavefront sensor," *Publications of the Astronomical Society of the Pacific*, vol. 125, pp. 422–430, Apr. 2013.

[160] J. L. Codona and N. Doble, "James Webb Space Telescope segment phasing using differential optical transfer functions," *Journal of Astronomical Telescopes, Instruments, and Systems*, vol. 1, no. 2, p. 029001, Apr. 2015.

[161] B. Pope, N. Cvetojevic, A. Cheetham, F. Martinache, B. Norris, and P. Tuthill, "A demonstration of wavefront sensing and mirror phasing from the image domain," *Monthly Notices of the Royal Astronomical Society*, vol. 440, pp. 125–133, May 2014.

[162] A. Z. Greenbaum, L. Pueyo, A. Sivaramakrishnan, and S. Lacour, "An image-plane algorithm for JWST's non-redundant aperture mask data," *Astrophysical Journal*, vol. 798, p. 68, Jan. 2015.

[163] A. R. Contos, D. S. Acton, P. D. Atcheson, A. A. Barto, P. A. Lightsey, and D. M. Shields, "Aligning and maintaining the optics for the James Webb Space Telescope (JWST) on-orbit: the wavefront sensing and control concept of operations," *Society of Photo-Optical Instrumentation Engineers (SPIE) Conference Series*, vol. 6265, p. 62650X, Jun. 2006.

[164] M. D. Perrin, J. Long, A. Sivaramakrishnan, C.-P. Lajoie, E. Elliot, L. Pueyo, and L. Albert, "WebbPSF: James Webb Space Telescope PSF simulation tool," Astrophysics Source Code Library, Apr. 2015.

[165] M. D. Perrin, A. Sivaramakrishnan, C.-P. Lajoie, E. Elliott, L. Pueyo, S. Ravindranath, and L. Albert, "Updated point spread function simulations for JWST with WebbPSF," *Society of Photo-Optical Instrumentation Engineers (SPIE) Conference Series*, vol. 9143, p. 91433X, Aug. 2014.

[166] D. S. Acton and J. S. Knight, "Multi-field alignment of the James Webb Space Telescope," *Society of Photo-Optical Instrumentation Engineers (SPIE) Conference Series*, vol. 8442, p. 84423C, Sep. 2012.

[167] D. Spergel, N. Gehrels, J. Breckinridge, M. Donahue, A. Dressler, B. S. Gaudi, T. Greene, O. Guyon, C. Hirata, J. Kalirai, N. J. Kasdin, W. Moos, S. Perlmutter, M. Postman, B. Rauscher, J. Rhodes, Y. Wang, D. Weinberg, J. Centrella, W. Traub, C. Baltay, J. Colbert, D. Bennett, A. Kiessling, B. Macintosh, J. Merten, M. Mortonson, M. Penny, E. Rozo, D. Savransky, K. Stapelfeldt, Y. Zu, C. Baker, E. Cheng, D. Content, J. Dooley, M. Foote, R. Goullioud, K. Grady, C. Jackson, J. Kruk, M. Levine, M. Melton, C. Peddie, J. Ruffa, and S. Shaklan, "Wide-Field InfraRed Survey Telescope-Astrophysics Focused Telescope Assets WFIRST-AFTA final report," *ArXiv e-prints*, May 2013.

[168] D. R. Soderblom, "The Ages of Stars," *Annual Review of Astronomy and Astrophysics*, vol. 48, pp. 581–629, Sep. 2010.

[169] I. Baraffe, D. Homeier, F. Allard, and G. Chabrier, "New evolutionary models for pre-main sequence and main sequence low-mass stars down to the hydrogen-burning limit," *Astronomy Astrophysics*, vol. 577, p. A42, May 2015.

[170] A. Burrows, W. B. Hubbard, J. I. Lunine, and J. Liebert, "The theory of brown dwarfs and extrasolar giant planets," *Reviews of Modern Physics*, vol. 73, pp. 719–765, Jul. 2001.

[171] É. Artigau, A. Sivaramakrishnan, A. Z. Greenbaum, R. Doyon, P. Goudfrooij, A. W. Fullerton, D. Lafrenière, K. Volk, L. Albert, A. Martel, K. E. S. Ford, and B. L. McKernan, "NIRISS aperture masking interferometry: an overview of science opportunities," in *Space Telescopes and Instrumentation 2014: Optical, Infrared, and Millimeter Wave*, ser. Society of Photo-Optical Instrumentation Engineers (SPIE) Conference Series, vol. 9143, Aug. 2014, p. 914340.

Vita

Alexandra Z. Greenbaum received her Bachelor of Science degrees in Physics and Mechanical Engineering from Rensselaer Polytechnic Institute in Spring 2011, and enrolled in the Physics and Astronomy Ph.D. program at Johns Hopkins University in Fall of 2011. She was inducted into the Tau Beta Pi, Sigma Pi Sigma, and Pi Tau Sigma honor societies in 2010, and received a National Science Foundation Graduate Research Fellowship in 2013. Her research focuses on in-pupil interferometric imaging of planet forming regions, contributing both to instrumentation and observational progress for detecting moderate contrast structure at close inner working angles.

Starting in October 2016, Alexandra will start a postdoctoral fellow position in planet formation science at the University of Michigan in Ann Arbor, MI, contributing to JWST NIRISS science programs and ground-based instrumentation.